

# **IN SITU ELECTRICAL MEASUREMENTS IN TRANSMISSION ELECTRON MICROSCOPY**

## **Proefschrift**

ter verkrijging van de graad van doctor  
aan de Technische Universiteit Delft,  
op gezag van de Rector Magnificus prof. ir. K. C. A. M. Luyben,  
voorzitter van het College voor Promoties,  
in het openbaar te verdedigen  
op woensdag 16 januari 2013 om 12:30 uur

door

**Maria RUDNEVA**

Engineer-physicist, Moscow Engineering Physics Institute (State University),  
Moskou, Rusland  
geboren te Moskou, Sovjet-Unie.

Dit proefschrift is goedgekeurd door de promotor:

Prof. dr. H. W. Zandbergen

Samenstelling promotiecommissie:

Rector Magnificus	voorzitter
Prof. dr. H. W. Zandbergen	Technische Universiteit Delft, promotor
Prof. dr. ir. H. S. J. van der Zant	Technische Universiteit Delft
Prof. dr. P. M. Sarro	Technische Universiteit Delft
Prof. dr. J. W. M. Frenken	Universiteit Leiden
Prof. dr. E. Olsson	Chalmers University of Technology, Zweden
Prof. dr. J. Mayer	RWTH Aachen, Duitsland
Dr. A. F. de Jong	FEI Company
Prof. dr. ir. L. M. K. Vandersypen	Technische Universiteit Delft, reservelid

*Keywords:* Transmission electron microscopy, in situ measurements, helium ion microscopy.

*Printed by:* Ipskamp Drukkers B.V.

*Cover design:* Maria Rudneva

The work described in this thesis was financially supported by NIMIC consortium (Nano-Imaging under Industrial Conditions)

Cover Copyright © Oliopi - Fotolia.com

Copyright © 2013 by M. Rudneva

Casimir PhD series, Delft-Leiden 2012-39

ISBN 978-90-8593-147-8

An electronic version of this dissertation is available at

<http://repository.tudelft.nl/>.

To my family





# CONTENTS

<b>1</b>	<b>General Introduction</b>	<b>1</b>
1.1	Electrical measurements at the nanoscale . . . . .	1
1.2	Nanoscale modification of nanowires . . . . .	2
1.3	Fundamentals of electromigration . . . . .	3
1.4	References . . . . .	8
	<b>Thesis outline</b>	<b>13</b>
<b>2</b>	<b>Experimental techniques</b>	<b>17</b>
2.1	Transmission electron microscopy . . . . .	17
2.2	Helium-ion microscopy . . . . .	19
2.3	Atomic force microscopy . . . . .	21
2.4	Sample fabrication (overview) . . . . .	21
2.5	Measurement setup . . . . .	25
2.6	Potential problems . . . . .	27
2.7	References . . . . .	29
<b>3</b>	<b>Chapter 3</b>	<b>33</b>
3.1	Introduction . . . . .	34
3.2	Sample preparation . . . . .	34
3.3	Results and discussions . . . . .	36
3.4	Simulation . . . . .	41
3.5	Summary . . . . .	46
3.6	Conclusions . . . . .	47
3.7	Acknowledgements . . . . .	47
3.8	References . . . . .	47
<b>4</b>	<b>Chapter 4</b>	<b>51</b>
4.1	Introduction . . . . .	52
4.2	Materials and Methods . . . . .	53

---

4.3 Results . . . . .	53
4.4 Discussion . . . . .	63
4.5 Summary . . . . .	64
4.6 References . . . . .	64
<b>5 Chapter 5</b>	<b>67</b>
5.1 Introduction . . . . .	68
5.2 Materials and Methods . . . . .	69
5.3 Results . . . . .	70
5.4 Summary and conclusions . . . . .	80
5.5 References . . . . .	81
<b>6 Chapter 6</b>	<b>83</b>
6.1 Introduction . . . . .	84
6.2 Modification of Si lamellas . . . . .	85
6.2.1 Methods . . . . .	86
6.2.2 Results . . . . .	88
6.2.3 Discussion . . . . .	91
6.3 Nanoscale modification of SrTiO <sub>3</sub> . . . . .	91
6.3.1 Discussion . . . . .	93
6.4 Nanoscale modification of Pt bridges . . . . .	96
6.5 In situ electrical measurements on HIM modified samples . . . . .	98
6.6 Conclusions . . . . .	101
6.7 References . . . . .	101
<b>Summary</b>	<b>105</b>
<b>Curriculum Vitae</b>	<b>107</b>
<b>List of Publications</b>	<b>109</b>

# 1

## GENERAL INTRODUCTION

### 1.1 ELECTRICAL MEASUREMENTS AT THE NANOSCALE

**I**NTERCONNECTS failure due to high current densities and local heating is an important problem for the development and functioning of various nanoelectronic devices. At the scales significantly smaller than one micron, surface and interface effects become prevalent. Therefore the characterization and understanding of the failure mechanisms and electrical transport properties is crucial for the further development of nanoelectronics. Ten-nanometer-scale metallic wires are used increasingly often for such studies and applications. However, passing an electric current through such wires can lead to their thinning. Finally wires become more like atomic point contacts and no longer reveal mesoscopic properties.

Performing experiments at the nanoscale requires the development of new methods for sample fabrication as well as for precise observation and characterization of the processes, that take place in the samples [1]. Apart from the imaging of these processes advances in observation and characterization methods quite often result in the development of new techniques or the discovery of new effects. For example, it has been found that nanobridge breakage due to electromigration can be controlled. It is in fact possible to produce small nanogaps that can be used, for instance, to create single-molecule transport junctions [2, 3]. The possibility of performing *in situ* electrical measurements combined with microscopy imaging techniques directly benefits the areas of micro-, nano- and molecular electronics.

Only in the past ten years has it been possible to couple the electrical characterization of samples with *ex situ* microscopy. Recently, a few advanced techniques were developed to make simultaneous *in situ* measurements possible. Since then, such an approach was used to characterize one-dimensional structures such as nanotubes, nanorods, and nanoparticles [4-8]. Furthermore, the characterization of two-dimensional nanoscale structures has been attempted by means of a limited number of techniques. For example, a method of two-dimensional point probe electrical measurements in transmission electron microscopy (TEM) was proposed to identify electrical properties at specific positions [9]. In addition, resistance monitoring during sample modification by an electron beam has been reported. This was performed for single-crystalline silver nanowires, the electrical properties of which were measured *in situ* in TEM [10]. However, a method of characterizing the intrinsic properties in nanoscale devices combined with real-time imaging was still missing. The development of such method is one of the goals of this thesis.

## 1.2 NANOSCALE MODIFICATION OF NANOWIRES

An electric current and related heating of a nanowire may result in various effects such as electromigration- induced changes in the wire's microstructure due to grain growth or changes in the its geometry and even in subsequent breakage. On the other hand, both current stressing and heating can in principle be applied for controlled nanoscale modification of the samples. For example, the application of an electric current with high density leads to the formation of two electrodes with a separation of just a few nanometers. Such structures cannot be made with the widely used e-beam lithography technique because it is unable to provide a resolution below 5 nm [11]. Molecular electronics, for instance, requires the electrode separation to be as small as 1-2 nm. Such devices recently became available by performing *ex situ* electromigration on thin nanowires combined with a self-breaking technique; nevertheless the reproducibility of the method still remains an open question and the shape of the electrodes is unknown. Clearly, the capability to characterize and control such nanogaps with sub-nanometer precision is required.

Precise sculpting of the samples with a focused beam of charged particles is considered a nice tool for nanoscale modification. The use of electron beams yields good results for soft samples, such as biosamples [12] or thin samples, such as a few layers of graphene flake [13, 14]. Modification of thin films, nanowires or even bulk samples requires the use of heavier particles, such as ions. Today, the two most popular sources of focused ion beams are a gallium focused ion-beam microscope

(Ga-FIB) and a helium-ion microscope (HIM). It has been shown that Ga ions cannot be focused onto a sub-nanometer probe [15, 16]. Furthermore, they lead to unavoidable contamination of the sub-surface layer, making their application for nanoscale modification rather problematic. Helium ions, in comparison with Ga, are much lighter, inert, and can be collimated very well into a nanometer-sized probe [17]. The details of nanoscale modification with a helium-ion beam will be discussed in **Chapter 6**.

### 1.3 FUNDAMENTALS OF ELECTROMIGRATION

In this thesis significant attention is devoted to the *in situ* investigation of electromigration in thin polycrystalline metal films. What follows is a brief overview of this phenomenon and a discussion of the main factors that affects it.

Electromigration is the thermally assisted motion of ions under the influence of an electric field. It is considered to be one of the main reasons for electric circuit failure [18-21]. In order to understand the mechanisms by which material is transported due to the flow of electric current, many parameters should be taken into account: the material of the wire, its geometry, current density and distribution, the temperature of the sample during electromigration and the diffusion rate of material along the wire determined by its microstructure should be considered [22].

Instant heating of a metallic wire under electric current stressing is due to electron-phonon interaction and increases the mobility of the atoms in the metal.

The driving force applied to the atom is proportional to the electric field  $\mathbf{E}$  and characterized by the what is called the effective charge  $Z^*$ :

$$\mathbf{F} = Z^* e\mathbf{E}. \quad (1.1)$$

where  $e$  is the elementary charge. Two terms contribute to the driving force: the direct force due to the applied external field and the electron wind force due to the momentum exchange with the current carriers [23-25]. If the electron wind force dominates over the direct force, atoms propelled by the electron wind start to move in the direction of the electron flow (Figure 1.1(a)). The rate at which they propagate is determined by the local diffusion coefficient, as illustrated in Figure 1.1(b) and Table 1.1. Thus, the atomic flux depends not only on the driving force, but also on the mobility of the atoms, which is expressed by the Nernst-Einstein equation for the atomic drift velocity [25]:

$$\mathbf{v} = \frac{D}{kT}\mathbf{F}. \quad (1.2)$$

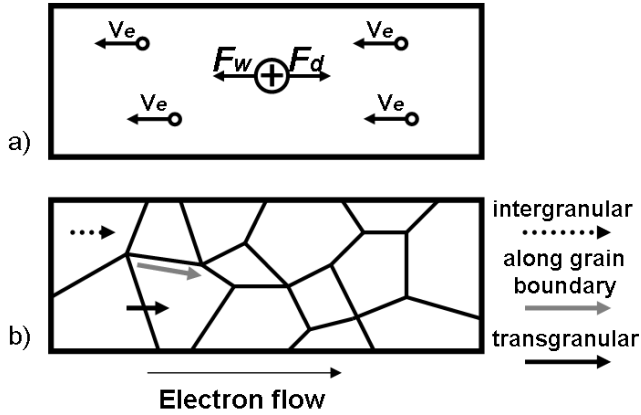


FIGURE 1.1: (a) Direct and electron wind forces are applied to an atom during electromigration. (b) Motion of ions due to the flow of electric current. The length of the respective arrows indicates the relative diffusion rate in each case [21].

where the diffusivity  $D = D_0 \exp(-Q/kT)$  contains the constant  $D_0$ , the activation energy  $Q$ , Boltzmann's constant  $k$ , and temperature  $T$ . Being an activated diffusion process, the electromigration rate increases with increasing temperature. In Table 1.1 we list typical values for diffusivity, thus quantifying the rate of electro-migration of two typical materials Cu and Al[26].

At  $100^\circ\text{C}$  the lattice diffusivity of Al and Cu is insignificant. The surface diffusivity is three orders of magnitude greater than the grain boundary diffusivity in the case of Cu and eight orders of magnitude greater for Al. At  $350^\circ\text{C}$  the difference between the grain boundary and surface diffusivity for Cu and Al is much smaller, so both terms should be considered at higher temperatures.

## MEAN TIME TO FAILURE AND ACCELERATED ELECTROMIGRATION EXPERIMENTS

One of the most important parameters characterizing electromigration is "mean time to failure" (MTFF). This value is governed, for a given applied current density, by Black's equation [28]:

$$t_{50} = C J^{-n} e^{-E_a/k_b T}. \quad (1.3)$$

where  $t_{50}$  is the MTFF,  $C$  is a constant factor dependent on the material properties (geometry, diffusion constant, etc.),  $J$  is the current density,  $T$  is the temperature,  $E_a$

Material	Melting point, $T_m$ (K)	Temperature ratio $373K/T_m(K)$	Diffusivities at 100°C (cm <sup>2</sup> /s)	Diffusivities at 350°C (cm <sup>2</sup> /s)
Cu	1356	0.275	Lattice $D_l = 7 \times 10^{-28}$ Grain boundary $D_{Gb} = 3 \times 10^{-15}$ Surface $D_s = 10^{-12}$	$D_l = 5 \times 10^{-17}$ $D_{Gb} = 1.2 \times 10^{-9}$ $D_s = 10^{-11}$
Al	933	0.4	Lattice $D_l = 1.5 \times 10^{-19}$ Grain boundary $D_{Gb} = 6 \times 10^{-11}$	$D_l = 10^{-11}$ $D_{Gb} = 5 \times 10^{-7}$

TABLE 1.1: Diffusivities of Al and Cu calculated for 100°C and 350°C

is the electromigration activation energy (for example, the typical value of  $E_a$  for Al is 0.5-0.7 eV [19]),  $k_b$  is Boltzmann's constant and  $n$  is an integer which in most cases is 2. As can be seen from this equation, the lifetime of wires is inversely proportional to the current density squared and has an even stronger exponential dependence on the temperature. However, during *in situ* TEM experiments accelerated electromigration is normally observed where the current density is deliberately increased to minimize the experiment time. This affects the mechanisms governing the failure such as stress and temperature [29] and thus Black's equation yields correct values of MTTF only in a limited range of temperatures and current densities [30].

### TEMPERATURE EFFECT: CURRENT-INDUCED HEATING IN A NANOWIRE

Temperature is an important factor defining the rate of failure due to electromigration. For thin wires, deposited or embedded in a substrate, temperature depends on the balance between the net energy input from the current flowing through the wire and the energy loss rate to the surroundings.

Our samples can be described by a simple model of a wire connected to two semi-infinite heat sinks. Poisson's equation in the wire and the contacts has the form[21]:

$$\nabla^2 T - m^2 T + \frac{Q}{k} = 0, \quad (1.4)$$

where

$$m = \sqrt{\frac{k_{sub}}{ktd}}. \quad (1.5)$$

The term  $Q/k$  is the rate of generation of thermal energy,  $Q = J^2$ ,  $k$  and  $k_{sub}$  are the thermal conductivities of the wire and the substrate,  $t$  and  $d$  are the thicknesses of the wire and the substrate, respectively. From this equation one can conclude that:

- The temperature and thus the thermal stress have a peak at the center of the wire;
- The temperature depends on the wire thickness and lengths and not on the width for a given current density [21].

Therefore, if the wire has failed catastrophically at the center, we can conclude that it is very likely due to thermomechanical stress (see Chapter 3).

The temperature of the sample depends on the efficiency of heat dissipation through the substrate. For instance, in the case of a gold nanowire deposited onto a  $\text{SiO}_2$  membrane, the peak temperature is expected to be higher for thinner substrates [22]. Our experimental observations of various membrane thicknesses revealed no significant changes in the results.

### EFFECT OF ELECTROMIGRATION-INDUCED STRESS

Let us now examine the role played by electromigration-induced stress in wire failure. A few important points to be mentioned are [31]:

- Stress gradients can be considered a driving force for the motion of metal atoms;
- Sample failure will occur when critical stresses are reached (either compressive stress that forms extrusions or tensile stress that forms voids);
- Stresses affect the diffusion process: Tensile stress makes diffusion easier and compressive stress makes diffusion more difficult.

A series of experimental and theoretical work was carried out by Blech and co-workers on metal islands deposited onto a refractory metal underlay [32-34]. They demonstrated the effect of a stress gradient and how it provides a driving force for



diffusion that acts opposite to the electromigration force. Blech found a threshold relationship between electromigration drift, current density and conductor length:

$$Jl_{Blech} \leq A_{Blech} \quad (1.6)$$

where  $J$  is the current density and  $l_{Blech}$  is known as the "Blech length". Analogously, their product  $A_{Blech}$  is called the "Blech product". If the product is less than a certain critical value electromigration will not be observed. Thus, if a conductor is shorter than the Blech length for a given current density, electromigration can be eliminated as a failure mechanism. The Blech product  $A_{Blech}$  for Al-based metallization is of the order of 2000 to 3000. For the current densities of about  $10^6 \text{ Acm}^{-2}$  the calculated Blech length is 20 to 30  $\mu\text{m}$ . For the samples described in Chapters 4 and 5 of this thesis electromigration was observed in much shorter samples (300 nm for Pt and 500 nm for Pd) at current densities of order of  $3 \times 10^7 \text{ Acm}^{-2}$ .

### CRITICAL STRESS AS A CRITERION FOR FAILURE

During electromigration one side of the sample will possess a positive flux divergence - a net influx of material - and thus an extrusion/hillock is formed. If a negative flux divergence is present and there is a net loss of material, voids are formed. In both cases, failure will only occur after a critical stress is reached. In the case of a metal wire the stress will be the greatest at the ends of the wire. Therefore the electromigration stress is greatest at the end whereas the thermal stress and temperature are greatest at the center.

### INFLUENCE OF WIRE GEOMETRY AND MICROSTRUCTURE ON ELECTROMIGRATION

Wires normally possess one of the three types of microstructure: single-crystal, bamboo-like and polycrystalline. As the wire width decreases passing from a polycrystalline to a bamboo-like structure, the wire should become less susceptible to failure.

It was shown theoretically [22] that for longer wires the following effects are observed: the stress due to electromigration and the peak temperature at the center of the wire increase linearly with the wire length. A combination of these two factors results in the fact that longer wires fail more readily than shorter ones.

On the other hand the temperature is independent of the wire width whereas the atom flux depends very strongly on the width of the wire. As soon as the wire width becomes smaller than the average grain size (bamboo structure), the atom flux

should decrease. As a result, narrower wires are more stable if the width approaches the grain size. Theoretical calculations and experimental results can be summarized as follows [22, 35-37]:

- The lifetime of the wire decreases with increasing wire length;
- Polycrystalline wires fail more readily than bamboo-like wires;
- The rate of failure of the wires increases dramatically once the wire width decreases below the mean grain diameter;
- Wires reach high temperatures due to current flow;
- The wire temperature depends on the thickness of the membrane on which the wire is deposited;
- As the temperature of a wire increases the failure point and thus the maximum of the total stress shifts from the cathode end towards the center of the wire.

Experimental evidence supporting these conclusions has been presented by many researchers for large scale ( $> 1 \mu\text{m}$ ) interconnects [27, 35, 38-40], whereas very little work has been done on nanowires. In this thesis, an electromigration study was carried out on thin polycrystalline Pt and Pd films and the validity of some of the above statements was checked for this type of structures.

## 1.4 REFERENCES

1. Esen, G. and M.S. Fuhrer, *Temperature control of electromigration to form gold nanogap junctions*. Applied Physics Letters, 2005. **87(26)**.
2. Gao, B., et al., *Three-terminal electric transport measurements on gold nanoparticles combined with ex situ TEM inspection*. Nanotechnology, 2009. **20(41)**.
3. Heersche, H.B., et al., *In situ imaging of electromigration-induced nanogap formation by transmission electron microscopy*. Applied Physics Letters, 2007. **91(7)**.
4. Minot, E.D., et al., *Tuning carbon nanotube band gaps with strain*. Physical Review Letters, 2003. **90(15)**.
5. Kim, T.Y., et al., *In situ measurements and transmission electron microscopy of carbon nanotube field-effect transistors*. Ultramicroscopy, 2008. **108(7)**: p. 613-618.
6. K. Svensson, H. Olin and E. Olsson, *Nanopipettes for metal transport*, Phys. Rev. Lett. **93 (2004)** 14590

7. Golberg, D., et al., *In situ electrical probing and bias-mediated manipulation of dielectric nanotubes in a high-resolution transmission electron microscope*. Applied Physics Letters, 2006. **88(12)**.
8. Howe, J.M., H. Mori, and Z.L. Wang, *In situ high-resolution transmission electron microscopy in the study of nanomaterials and properties*. MRS Bulletin, 2008. **33(2)**: p. 115-121.
9. Park, S., M.J. Kim, and O. Lourie, *Direct Two-Dimensional Electrical Measurement Using Point Probing for Doping Area Identification of Nanodevice in Tem*. Nano, 2010. **5(1)**: p. 61-66.
10. Liu, X.H., et al., *In situ electrical measurements of polytypic silver nanowires*. Nanotechnology, 2008. **19(8)**.
11. Broers, A.N., A.C.F. Hoole, and J.M. Ryan, *Electron beam lithography - Resolution limits*. Microelectronic Engineering, 1996. **32(1-4)**: p. 131-142.
12. Cairns, M.L., et al., *The potential of electron beam radiation for simultaneous surface modification and bioresorption control of PLLA*. Journal of Biomedical Materials Research Part A, 2012. **100A(9)**: p. 2223-2229.
13. Gardener, J.A. and J.A. Golovchenko, *Ice-assisted electron beam lithography of graphene*. Nanotechnology, 2012. **23(18)**.
14. Schneider, G.F., et al., *DNA Translocation through Graphene Nanopores*. Nano Letters, 2010. **10(8)**: p. 3163-3167.
15. Floresca, H.C., et al., *The Focused Ion Beam Fold-Out: Sample Preparation Method for Transmission Electron Microscopy*. Microscopy and Microanalysis, 2009. **15(6)**: p. 558-563.
16. Sciau, P., et al., *Applications of focused ion beam for preparation of specimens of ancient ceramic for electron microscopy and synchrotron X-ray studies*. Micron, 2009. **40(5-6)**: p. 597-604.
17. Postek, M.T., et al., *Review of current progress in nanometrology with the helium ion microscope*. Measurement Science & Technology, 2011. **22(2)**.
18. Sanchez, J.E., L.T. Mcknelly, and J.W. Morris, *Slit Morphology of Electromigration Induced Open Circuit Failures in Fine Line Conductors*. Journal of Applied Physics, 1992. **72(7)**: p. 3201-3203.
19. Joo, Y.C. and C.V. Thompson, *Electromigration-induced transgranular failure mechanisms in single-crystal aluminum interconnects*. Journal of Applied Physics, 1997. **81(9)**: p. 6062-6072.
20. Paik, J.M., et al., *Linewidth dependence of grain structure and stress in damascene Cu lines*. Journal of Applied Physics, 2006. **99(2)**.

21. Josell, D., D. Wheeler, and T.P. Moffat, *Gold superfill in submicrometer trenches: Experiment and prediction*. Journal of the Electrochemical Society, 2006. **153(1)**: p. C11-C18.
22. Durkan, C., *Current at nanoscale. An introduction to Nanoelectronics.*, ed. I.C. Press 2007.
23. Landauer, R. and J.W.F. Woo, *Driving Force in Electromigration*. Physical Review B, 1974. **10(4)**: p. 1266-1271.
24. Lodder, A., *The Driving Force in Electromigration*. Physica A, 1989. **158(3)**: p. 723-739.
25. Sham, L.J., *Microscopic Theory of Driving Force in Electromigration*. Physical Review B, 1975. **12(8)**: p. 3142-3149.
26. Ho, P.S. and Huntington, Hb, *Electromigration and Void Observation in Silver*. Journal of Physics and Chemistry of Solids, 1966. **27(8)**: p. 1319.
27. Tu, K.N., *Recent advances on electromigration in very-large-scale-integration of interconnects*. Journal of Applied Physics, 2003. **94(9)**: p. 5451-5473.
28. Black, J.R., *Electromigration - a Brief Survey and Some Recent Results*. Ieee Transactions on Electron Devices, 1969. **Ed16(4)**: p. 338.
29. Pramanick, S., et al., *Effect of mechanical stress on electromigration failure mode during accelerated electromigration tests*. Thin Films: Stresses and Mechanical Properties V, 1995. **356**: p. 507-512.
30. Foley, S., et al., *A comparison between normally and highly accelerated electromigration tests*. Microelectronics and Reliability, 1998. **38(6-8)**: p. 1021-1027.
31. Lloyd, J.R., *Electromigration in thin film conductors*. Semiconductor Science and Technology, 1997. **12(10)**: p. 1177-1185.
32. Blech, I.A., *Electromigration in Thin Aluminum Films on Titanium Nitride*. Journal of Applied Physics, 1976. **47(4)**: p. 1203-1208.
33. Blech, I.A. and C. Herring, *Stress Generation by Electromigration*. Applied Physics Letters, 1976. **29(3)**: p. 131-133.
34. Blech, I.A. and E. Kinsbron, *Electromigration in Thin Gold-Films on Molybdenum Surfaces*. Thin Solid Films, 1975. **25(2)**: p. 327-334.
35. Kwok, T. *Effect of metal line geometry on electromigration lifetime in Al-Cu submicron interconnects*. in International Reliability Physics Symposium. 1989.
36. Alford, T.L., et al., *Influence of Joule heating during electromigration evaluation of silver lines*. Thin Solid Films, 2009. **517(5)**: p. 1833-1836.
37. Liu, Y.K., C.L. Cox, and R.J. Diefendorf, *Finite element analysis of the effects of geometry and microstructure on electromigration in confined metal lines*. Journal

of Applied Physics, 1998. **83(7)**: p. 3600-3608.

38. Okabayashi, H., *Stress-Induced Void Formation in Metallization for Integrated-Circuits*. Materials Science & Engineering R-Reports, 1993. **11(5)**: p. 189-241.

39. Kirchheim, R., *Stress and Electromigration in Al-Lines of Integrated-Circuits*. Acta Metallurgica Et Materialia, 1992. **40(2)**: p. 309-323.

40. Kraft, O. and E. Arzt, *Electromigration mechanisms in conductor lines: Void shape changes and slit-like failure*. Acta Materialia, 1997. **45(4)**: p. 1599-1611.



# THESIS OUTLINE

Studies of nanostructures are commonly associated with an analysis of the end product - either synthesized or specifically modified objects on the nanoscale. Objectively, the physical phenomena that take place during processing or the evolution of the properties of nanostructures often escape the attention they deserve. That is because the real-time observations can be extremely challenging due to a number of factors such as proper sample preparation, the availability of fast scan cameras and difficulties to correlate the applied treatment with the observed changes.

This thesis presents how the *in situ* real-time TEM observations of electromigration and current-induced grain growth in thin films with TEM were made possible. The development of this method can potentially yield benefits for nanoscale electronics, measurements on nanowires and graphene nanoribbons, managing of molecular electronic devices and further progress of *in situ* TEM characterization.

Basic concepts of electromigration in thin metal films are described in **Chapter 1**, where the application of a helium microscope as a sample preparation tool for *in situ* electrical measurements is also discussed.

Technical aspects of transmission electron microscopy (TEM), helium-ion microscopy (HIM) and atomic force microscopy (AFM) as well as various experimental approaches used throughout the present work are considered in **Chapter 2**. By describing the measurement setup, I will also provide sample fabrication details and characteristics of a specially developed sample holder for the electrical measurements. I will also highlight some typical problems of *in situ* experiments in TEM such as contamination and charging of the sample.

Differences in the structure of the polycrystalline platinum (Pt) bridges imaged prior and after application of an electric current provoke the particular interest in an *in situ* TEM investigation of the processes that take place in the bridge during voltage stressing. In **Chapter 3** the results of an *in situ* TEM study of grain growth in a Pt nanobridge are presented. The grain growth is induced by a high electric current density. The change in morphology of the Pt bridge at the nanoscale is directly

correlated with the electrical characterization. TEM inspection shows that the drop in the differential resistance that is clearly observed on an I-V curve coincides with thermally induced grain growth. The temperature required to initialize the grain growth is estimated numerically and measured directly by combining the use of special MEMS heating devices with TEM observation. Both experimental and simulation data is presented.

In **Chapter 4** *in situ* observations of electromigration in  $200 \times 300 \text{ nm}^2$  Pt bridges and the capability to create two electrodes with a separation of a few nanometers are discussed in detail. The electromigration is performed in two modes: one mode with feedback control and a bias ramping mode without feedback control. In the first case, symmetric electrodes are obtained and the gap usually forms at the center of the nanobridge. Without feedback control asymmetric electrodes are formed and the gap can occur at any position along the wire. The feasibility of performing "reversed electromigration" in a Pt bridge by changing the current direction is shown. The three-dimensional gap geometries of the electrodes in the Pt nanowire are determined using high-angle annular dark-field scanning transmission electron microscopy.

The capability to analyze the mass flow generated by voltage stressing with the scanning TEM technique is shown in **Chapter 5**. That chapter explores the phenomenon of reversed electromigration in thin polycrystalline Pd bridges. The results are compared with those obtained with conventional TEM and with *ex situ* AFM imaging for the Pd bridges of different geometries. It is shown that for a thin polycrystalline Pd bridge, material is transferred from the cathode to the anode. By reversing the current direction it is possible to restore the shape of the electromigrated bridge and thus to control the resistance of such a device.

Among the many techniques used for TEM sample preparation, modification with a particle beam appears most promising from the perspective of sculpting structures at the nanoscale. Use of electron and gallium ion beams for such modifications has already been described quite well. Recently it became possible to use a helium beam of a helium ion microscope developed by Carl Zeiss AG for this purpose. **Chapter 6** is devoted to the applicability of the helium ion microscope as a tool for precise modification of Si, SrTiO<sub>3</sub> and Pt samples. We developed a heating stage that allows one to obtain defect-free cuts in Si lamellas and to thin down the selected areas of the sample. During such modification no noticeable changes were created in the surrounding area or in the crystalline structure of the sample. The quality of such cuts was inspected by TEM with high-resolution imaging, and



an analysis of the diffraction patterns was performed. Therefore the modification of the samples with a helium beam ion at elevated temperatures can be used in principle to repair failures in integrated circuits.

A set of Pt bridges with standard geometry was modified at room temperature into different shapes using focused He-ion beam. *In situ* electrical measurements of the modified bridges allow examining the influence of the focused He-ion beam treatment on the samples. It is shown that this provides an excellent way to make one kind of modification to correlate geometry of the samples with their electrical properties without needing to fabricate a new batch of samples.



# 2

## EXPERIMENTAL TECHNIQUES

### 2.1 TRANSMISSION ELECTRON MICROSCOPY

The history of electron microscopes dates back to the 1930's when Max Knoll and Ernst Ruska introduced their first machine. Although Ernst Ruska was awarded the Nobel Prize in Physics for this invention many years later - only in 1986 - the interest in electron microscopy was increasing quickly since its first days. In 1938, the first scanning transmission electron microscope was presented by M. von Ardenne and already in 1945 the resolution record has surpassed 1 nm.

The best resolution achieved with modern transmission electron microscopes left this historical mark of 1 nm far behind and has now almost reached its physical limit posed by the information content of the sample.

In the electron microscope a beam of accelerated electrons is focused on a sample and the generated signal is recorded by an electron-sensitive detector (for example an image plate or CCD camera) in such a way that the image is formed. Compared to other microscopy techniques transmission electron microscopy is an extremely powerful tool allowing scientists to investigate nanoscale sized samples and literally look at atoms. However its remarkable advantages are countered by the strict requirements for sample preparation and by the cost of such machines.

A TEM appears in different forms known as high-resolution transmission electron microscopy (HRTEM), scanning transmission electron microscopy (STEM) and analytical electron microscopy (AEM). The present work will focus mostly on the

first two forms, although some AEM studies are included for the analysis of sample composition and thicknesses.

### **BASICS OF TRANSMISSION ELECTRON MICROSCOPY**

A transmission electron microscope can be divided into three parts according to its optical functions: the illumination part, the objective lens system and the magnification part. A schematic diagram showing the main parts of the microscope is presented in Figure 2.1. The main part of the illumination system is an electron source. The FEI Titan microscope used throughout this work is equipped with a Schottky field emission gun. Compared to LaB<sub>6</sub> and W sources utilized in older microscopes, this type of electron emitter provides greater brightness and stability of the beam but at the same time requires better vacuum conditions. A few lenses are placed right after the electron source: a gun lens that forms a virtual source in front of the gun and two or three condenser lenses that control the size of the virtual source and the illumination on the specimen thus allowing us to obtain a parallel or a converged beam.

The imaging system of a TEM constitutes at least three lenses: the objective lens, the intermediate lens and the projector lens. The latter two lenses represent the magnification part. An objective lens forms the magnified image of the sample by focusing the electrons that are transmitted through the sample. The intermediate (or diffraction) lens magnifies the first diffraction pattern formed in the focal plane of the objective lens or the first intermediate image formed just in front of the lens. The purpose of the projector lens is to further magnify a diffraction pattern or an image of the sample.

Other important elements of the TEM are the beam deflection coils, detectors, monochromators and aberration correctors. For more information see [1].

### **SCANNING TRANSMISSION ELECTRON MICROSCOPY (STEM)**

In STEM mode, an electron beam is focused on a narrow spot and then scanned over the sample. To provide such a capability, a few dynamic deflection coils are placed in the TEM column, which allow it to raster the electron beam on the sample and to adjust the beam position and angle. The STEM image is created by collecting the high-angle scattered electrons using an annular dark-field detector (ADF) (Figure 2.1)

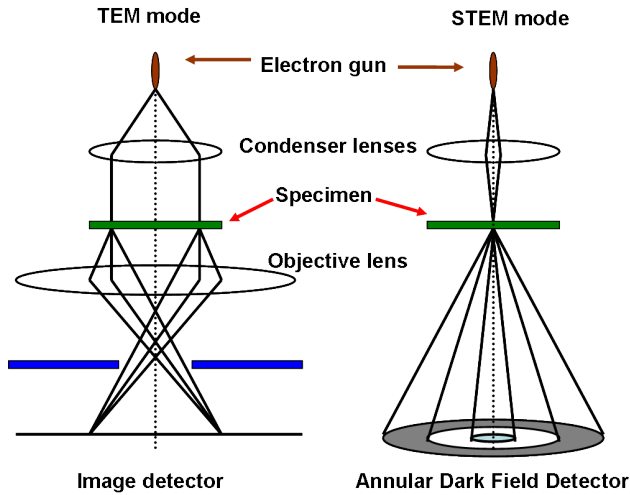


FIGURE 2.1: Schematic ray diagram of TEM and STEM operation modes.

## 2.2 HELIUM-ION MICROSCOPY

The helium-ion microscope (HIM) was introduced in 2006 as a new high-resolution imaging tool [2-4]. Many new application fields have been developed since then such as the precise imaging of bio-samples [5, 6], beam-sensitive samples and nano-samples [7], as well as nanofabrication with a He-beam [5, 6, 8-10]. The key feature of this microscope is the unique interaction of the primary helium-ion beam with the sample material at and just below its surface. This results in a relatively high number of low-energy secondary electrons from a well localized area around the point of incidence of the primary beam area, allowing a range of samples, including samples with high local specimen charging, to be imaged [11-13].

The scheme of the HIM column is shown in Figure 2.2. The inset to the figure shows a top view of the tungsten tip with its typical triangular shape.

In the HIM, a focused ion beam with a sub-nanometer sized probe is scanned over the sample surface [14]. Similar to the primary electron beam in SEM, the helium ions collide with surface and bulk atoms of the sample and create secondary electrons (SE). By recording the intensity of the SE signal while scanning the ion probe, an image of the sample surface with sub-nanometer resolution is obtained

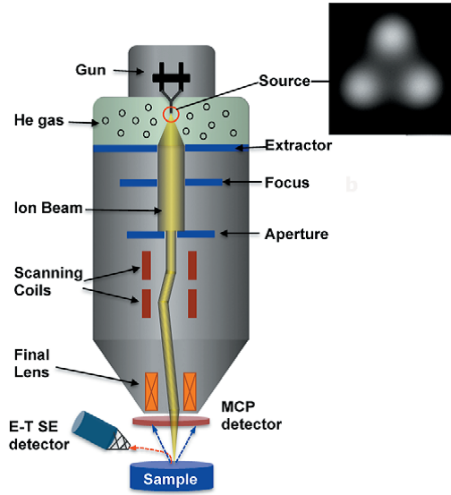


FIGURE 2.2: Schematic of the Orion-type helium microscope column. The ion source, aperture and detector configuration can be clearly seen. Inset: image of atomic trimer on tungsten showing He-ion emission from three atoms; one atom is selected to produce the beam for imaging [7]

in HIM [15, 16]. Comparing HIM and SEM we can list the following features of the HIM:

- The shorter wavelength of the heavier helium ions ( $\sim 1\%$  or less of that for electrons of the same energy) enables one to focus to approximately the same spot size at a typically 5 times smaller numerical aperture.
- Hence, the depth-of-focus can be five to ten times greater in HIM than in SEM.
- The velocity of a 30 keV helium ion is comparable to that of a 4 eV electron. The interaction volume within the sample is smaller for helium ions than for electrons.
- In HIM the interaction with the sample is more localized around the incident point of the scanning probe, but still spreading in bulk sample.

Therefore the HIM is well-suited for both high-resolution imaging as well as high resolution nanofabrication [17-20].

The HIM at the TNO Van Leeuwenhoek Laboratory (TNO-VLL)[4] is equipped with a pattern-generating system, which makes the exploration of nanofabrication capabilities of the HIM relatively easy. For maximum flexibility during nanofabrication, beam scan during deposition, etching and lithography can be controlled with the Elphy Plus (Raith GmbH) lithography pattern generator.

The HIM provides beam currents between 0.1 and 10 pA. Thus one can choose between noninvasive imaging at very low current values, including imaging of beam sensitive samples, or fast sample milling at high beam currents. The HIM at TNO-VLL is installed on a floating concrete floor that suppresses the transmission of low-frequency vibrations from the environment to the microscope. Additionally, TNO has developed an acoustic enclosure that suppresses room acoustic noise by at least 12 dB[21].

## 2.3 ATOMIC FORCE MICROSCOPY

An atomic force microscope (AFM) was used in this work to determine the three-dimensional topography of the samples (see Chapter 5). In the AFM the sharp cantilever is placed just above the area of interest—close enough to the surface to interact with the associated force field. The motion of the cantilever is controlled by piezo-electric motors. The deflection of the tip is measured by a laser spot that is focused on the back of the cantilever and reflected into a photo-detector. The electronic output of the sensor is related to the distance between the probe and the sample. Depending on the material and objective of the study, contact, non-contact or tapping modes can be used for sample characterization.

## 2.4 SAMPLE FABRICATION (OVERVIEW)

Figure 2.3 provides an overview of the fabrication processes in chronological order. Two fabrication processes were used to prepare samples for the experiments described in this thesis. Process flow (a) is used for the fabrication of silicon chips with free standing transparent SiN windows and for the simultaneous creation of the markers on a chip. Process flow (b) is used for the fabrication of the platinum nanobridges and gold electrical contacts on chip. Both processes have some similarities and the fabrication steps are listed below:

1. **Substrate preparation:** We start with a double-sided polished silicon substrate. Low-stress, 100-nm thick silicon nitride layers are grown on both sides of the substrate using low-pressure chemical vapor deposition (LPCVD). Next, the wafer

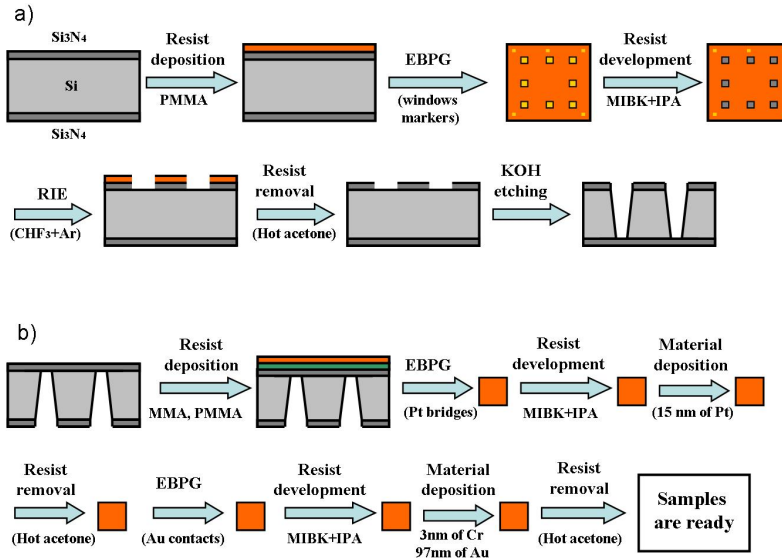


FIGURE 2.3: Overview of the fabrication process. (a) Fabrication of free standing windows and markers; (b) fabrication of the Pt bridges and gold contacts.

is covered with the AZ5214 resist to protect the membrane before being diced into square ( $14 \times 14 \text{ mm}^2$ ) by mechanical sawing.

2. **Cleaning:** Each piece is cleaned in fuming nitric acid for 10 minutes and rinsed with water to remove acid residues.

3. **Resist deposition:** We use three different recipes for each fabrication step: transparent windows, platinum bridges and gold contacts. In the first case the structure is coarse and does not require consideration of proximity effects and high accuracy so only one resist (polymethyl methacrylate or PMMA) is used. This is the most commonly used positive resist, which normally comes in powder form that is dissolved in a solvent (anisole in our case) to obtain the desired concentration (see Table 2.1). To fabricate platinum bridges and gold contacts, both copolymer Methyl MethAcrylate (MMA) and PMMA resists are deposited on the sample. Using mixed layers improves the sensitivity and thermal stability of the resist. The selected resist is first spin-coated onto the sample for 55 seconds at a preset speed (see Table 2.1). The sample is then baked on a hotplate at  $175^\circ\text{C}$  for 10-20 minutes. To fabricate platinum bridges and gold contacts we start by spin-coating the samples with an



Fabrication step	Resist	Rotation speed	Spinning time	Thickness of resist	Baking temperature	Baking time
Windows and markers	PMMA 950k, 7% in anisole	5000 rpm	55 sec	500 nm	175°C	60 min
Pt bridges	PMMA/MMA (17.7%), 8% in Ethyl-L-Lactate	3000 rpm	55 sec	300 nm	175°C	15 min
Pt bridges	PMMA 950k, 3% in anisole	3000 rpm	55 sec	130 nm	175°C	15 min
Au contacts	PMMA/MMA (17.5%), 8% in Ethyl-L-Lactate	1000 rpm	55 sec	500 nm	175°C	10 min
Au contacts	PMMA 950k, 2% in anisole	1000 rpm	55 sec	80 nm	175°C	20 min

TABLE 2.1: Overview of the parameters for resist spinning

MMA resist and then repeating the entire process for the PMMA layer. Details of each resist deposition step can be found in Table 2.1.

4. **Electron beam exposure:** The sample is exposed to a scanning electron beam (EB) generated by a 5000+ Leica pattern generator. Both resists, used in this fabrication are positive, so exposure to the e-beam changes the chemical structure of the resist such that it becomes more soluble in the developer.

5. **Resist development:** The sample is immersed for 70 seconds into a developer (1:3 MIBK), which resolves the exposed regions of the resist layer. To stop the development process, the sample is immersed in isopropanol for 50 seconds.

6. **Reactive ion etching (RIE):** The exposed SiN layer was removed by an anisotropic low-pressure reactive ion etching in a LHZ 400 system using the following recipe:  $\text{CHF}_3/\text{O}_2$ , gas flow 50/2.5 sccm, chamber pressure 8  $\mu\text{bar}$  and forward power 50 W. This step is used only to fabricate transparent windows and markers.

7. **Resist removal:** The remaining resist is removed by washing in hot acetone at 54°C for 20 minutes. After being cleaning with acetone, the sample is rinsed in isopropanol to remove any residue.

8. **KOH etching:** The remaining SiN was used as the mask for the following KOH wet etching, which produced the anisotropic V-shaped etching profile. This step is used only to fabricate transparent windows and markers.

9. **Material deposition:** A Temescal FC-2000 evaporator is used for Pt and Au/Cr deposition. A thin Cr layer is used for improving the adhesion of gold to the SiN membrane. The deposition rate for all metals is 1Å/s. The thicknesses of the deposited Pt, Cr and Au layers are 15, 3 and 97 nm, respectively.

10. **Substrate thinning (optional):** To improve the electron transparency of the SiN membrane for some experiments, it was dry etched from the underside in the LHZ 400 system using the following process: CHF<sub>3</sub>/Ar plasma, gas flow 25.0/16.8 sccm, chamber pressure 6.7 μbar and forward power 50 W. The final thickness of the etched membrane is approximately 20-30 nm. This step is used if one wants to improve resolution of TEM imaging, but it renders the membrane fragile so sample has to be handled very carefully.

11. **Cleaving:** The sample was manually cut with a diamond tool into pieces which fit into the sample holder of the TEM.

## ELECTRON BEAM LITHOGRAPHY

Lithography is a process of transferring patterns from a medium to a substrate [22]. Among different particle beams that could be used for lithography, electron beams are the most attractive ones due to their extremely high diffraction-limited resolution. Therefore electron-beam lithography (EBL) has become a widely used technique for the fabrication of nanoscale structures and for transferring patterns with nanometer sized features. One of the possible applications for EBL, for example, is to generate masks for optical projection printing which in turn are used in the semiconductor industry for pattern replication onto silicon wafers. In this work EBL was used to produce fine structures called nanobridges on the transparent SiN membrane by means of the direct writing method. In this case, a sample with a few deposited layers of resist is exposed to a scanning e-beam, generated by a 5000+ Leica EB pattern generator. A typical EB design is shown in Figure 2.4. The pattern normally comprises the nanobridges (shown in red) and electrical contacts (shown in yellow). Additional markers allow the fine and coarse structures to be matched as they are written in separate steps with different e-beam spot sizes. Both nanobridges and contacts are written using an e-beam with a 100-kV acceleration voltage and doses ranging between 900 and 1100 μC/cm<sup>2</sup>. The layout file of the sample patterns was created with LayoutBEAMER software [23].

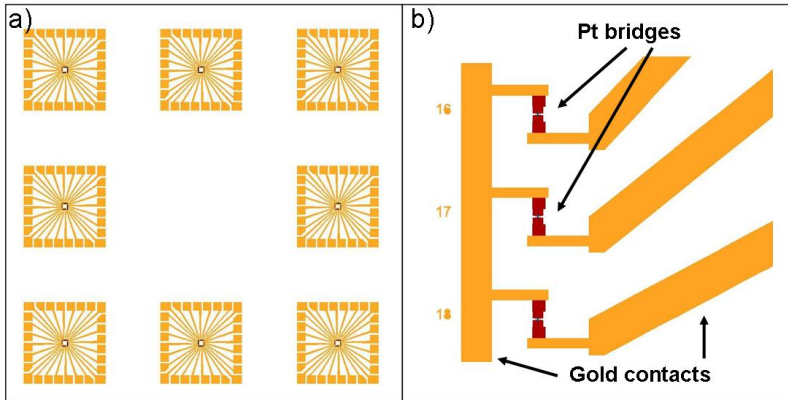


FIGURE 2.4: Structure layout for the electron beam exposure. (a) Overview of pattern showing both bridges and electrical contacts to be written; (b) Scheme of part of the structure representing Pt bridges and Au contacts.

## 2.5 MEASUREMENT SETUP

### HOLDER FOR *in situ* MEASUREMENTS

A special holder has been developed that allows sample modification caused by voltage/current stressing in the TEM to be observed and thus *in situ* electrical measurements to be performed. As can be seen in Figure 2.5, the holder may play various roles depending on the specific requirements for the experiment:

- **Single-tilt holder:** Allows the samples to be rotated only around the axis of the rod. Suitable for a simple TEM check of chip-like samples.
- **Cooling holder:** Allows the sample temperature to be set to a given value in the range between 100 and 273 K. The stage is cooled by lowering copper wires connected to the holder into a thermo flask filled with liquid nitrogen, an ice-water mixture or any other non-toxic and non-flammable liquids at temperatures below room temperature. Use of the cooling substantially reduces the amount of carbon contaminants deposited on the sample during experiments.
- **Heating:** A combination of the holder with the control box, a power supply for heating experiments and special MEMS-based heating chips can be used for

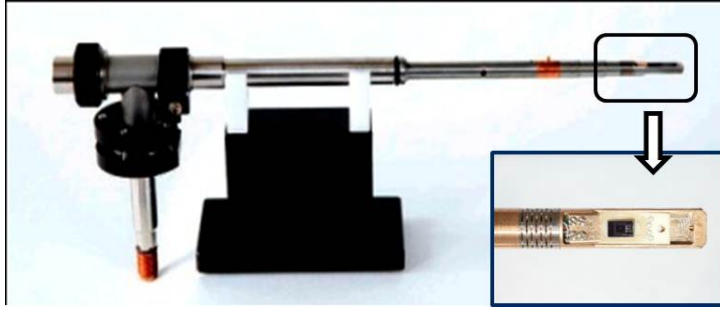


FIGURE 2.5: Holder for *in situ* electrical measurements. Inset: The tip of the holder with loaded chip-like sample connected to  $\text{Al}_2\text{O}_3$  carrier.

*in situ* electrical measurements at elevated temperatures. For some samples, cooling yielded undesirable effects such as the increase of the resistance in semiconducting nanowires or the formation of ice on the surface of graphene. In such cases, heating can be used.

- **Electrical measurements holder:** Eight separate electrical lines pass from the tip through the holder to an electrical connector. The lines are air tight and allow the electrical measurements to be performed inside the microscope. Chip-like samples glued to  $\text{Al}_2\text{O}_3$  chip carriers and placed at the tip of the holder are connected with the measurement setup via a copper shielded cable.

### SETUP FOR ELECTRICAL MEASUREMENTS

The in-house-built measurement electronics setup (IVVI rack designed by Raymond Schouten, TU Delft [24]) can host several modules such as voltage sources, current sources, current-voltage converters, and voltage amplifiers. All modules are enclosed by a shielded rack (bottom grey box in Figure 2.6). The entire system is designed to send and receive pulsed and DC signals to and from an experimental sample. The system is engineered to reduce external influences such as noise and interference signals, from sources or acquisition devices. The holder is connected via the cable to a matrix box. All signal inputs of the matrix box are equipped with grounding switches to prevent voltage spikes and low-pass filtered with 100 pF capacitors. All circuits connected to the measurement setup are battery-operated and isolated.

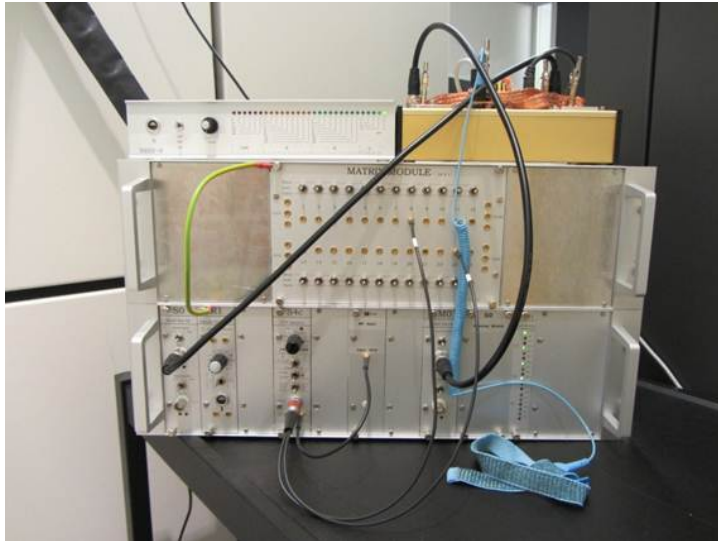


FIGURE 2.6: Measurement setup used throughout this work.

To control the measurements, the IVVI rack is connected to the ADwin module [25] consisting of a dedicated real-time processor, fast analog and digital inputs and outputs and a communicational link to a PC. The measurement setup has been automated using the LabVIEW programming environment (National Instruments).

## 2.6 POTENTIAL PROBLEMS

### CARBON CONTAMINATION

The problem of cleanliness of the specimen surfaces and TEM chambers is very critical as examination and fabrication techniques approach the atomic level [26]. Hydrocarbon (HC) contamination in the microscope chamber usually comes from the diffusion pump (not used in Titan), the grease used for vacuum seals, air - one second of breathing over sample holder can produce a monolayer of hydrocarbons - or from residues left on the sample after fabrication. During e-beam illumination carbonaceous materials can be deposited on a sample at room temperature in the form of circular contamination rings. Such shape of the deposited contaminants is due to a permanent supply of the hydrocarbons from the outside of the illuminating area. Therefore diffusion and cracks of HC occurs at the edges of the illuminated

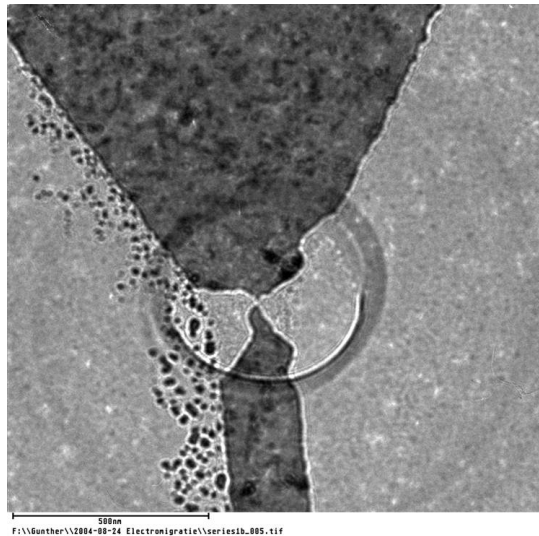


FIGURE 2.7: Micrograph of a severely contaminated TEM sample. Black rings on the image are due to carbon deposited during e-beam illumination.

area. Contamination causes a loss of resolution in TEM imaging and spectroscopy and in the case of *in situ* electrical measurements creates additional pathways for the current flow, which affect the measurement results.

In order to prevent carbon contamination one may use plasma-cleaning technology. Cooling of the sample is another way to prevent carbon deposition on the surface. In this case the diffusion of hydrocarbons on the sample is strongly suppressed and contamination build up occurs at a much lower rate than at room temperature thus not influencing the electrical measurements.

### CHARGING THE SAMPLE

Sample charging is one of the biggest problems for *in situ* TEM electrical measurements. In the worst case it can completely destroy the entire sample. One of the possible causes is the potential difference of 2 V between the CompuStage of the microscope and the ground. The 2 V connection is a safety component of the TEM used to detect a pole hit by the holder. On the other hand, the holder has to be connected via a cable to the grounded measurement setup. If a sample is occasionally brought into contact with the holder, this 2 V potential difference

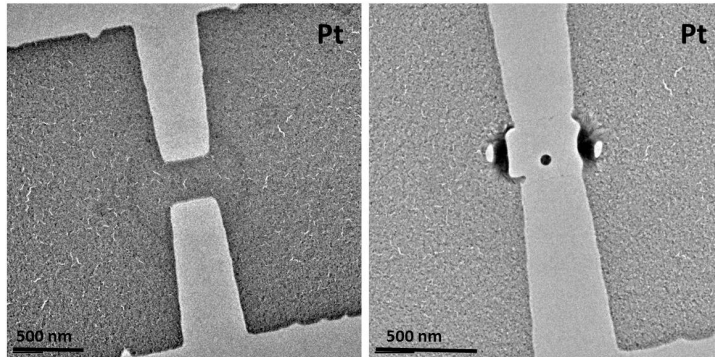


FIGURE 2.8: Failure of the sample due to accumulation of electrical charge. (a) As fabricated Pt bridge deposited on SiN membrane; (b) the sample bridge destroyed by an uncontrolled discharge.

immediately leads to high currents passing through the sample. The result of such an influence can be seen in Figure 2.8(b).

Electrostatic charge accumulated on the chip carrier, might also be a serious problem and has to be reduced. To protect the sample from breaking due to charging effects, direct electrical contact between a grounded chip and the holder (at 2 V) has to be prevented. For this purpose an insulating tape can be placed between the holder and the contact wires coming from the chip sample. Another possible solution is to develop a safety system that allows authorized users to switch off the 2 V bias of the CompuStage. In this case the sample holder is grounded and the sample is completely protected from uncontrolled charges, but the holder cannot be tilted. We used the latter solution in all our experiments.

## 2.7 REFERENCES

1. Williams, D.B., Carter, C. B, *Transmission Electron Microscopy. A Textbook for Material Science*, ed. S. Science2009.
2. Notte, J., et al., *An introduction to the helium ion microscope*. *Frontiers of Characterization and Metrology for Nanoelectronics: 2007*. **931**: p. 489-496.
3. Morgan, J., Notte, J., Hill, R., Ward, B., *An Introduction to the Helium Ion Microscope*. *Microscopy today*, 2006. **14**(4).
4. Bell, D.C., *Contrast mechanisms and image formation in Helium Ion microscopy*. *Microscopy and Microanalysis*, 2009. **15**: p. 147-153.

5. Scipioni, L., et al., *The Helium Ion Microscope: Advances in Technology and Applications*. American Laboratory, 2009. **41(12)**: p. 26-28.
6. Scipioni, L., et al., *Material Analysis With a Helium Ion Microscope*. 2009 Ieee International Reliability Physics Symposium, **Vols 1 and 2**, 2009: p. 317-321.
7. Bell, D.C., Stern, L. A., Farkas, L., Notte, J. A, *Application of the Helium Ion Microscope for the Imaging and Analysis of Nanomaterials*. Microscopy today, 2008. **14**.
8. Alkemade, P.F.A., et al., *Imaging and Nanofabrication With the Helium Ion Microscope of the Van Leeuwenhoek Laboratory in Delft*. Scanning, 2012. **34(2)**: p. 90-100.
9. Maas, D., et al., *Nanofabrication with a Helium Ion Microscope*. Metrology, Inspection, and Process Control for Microlithography, 2010. 7638.
10. Postek, M.T., A.E. Vladár, and J. Kramar, *The helium ion microscope: A new tool for nanomanufacturing* - art. no. 664806. Instrumentation, Metrology, and Standards for Nanomanufacturing, 2007. **6648**: p. 64806-64806.
11. Joy, D.C. and B.J. Griffin, *Is Microanalysis Possible in the Helium Ion Microscope?* Microscopy and Microanalysis, 2011. **17(4)**: p. 643-649.
12. Petrov, Y. and O. Vyvenko, *Secondary electron emission spectra and energy selective imaging in helium ion microscope*. Scanning Microscopies 2011: Advanced Microscopy Technologies for Defense, Homeland Security, Forensic, Life, Environmental, and Industrial Sciences, 2011. **8036**.
13. Ramachandra, R., B. Griffin, and D. Joy, *A model of secondary electron imaging in the helium ion scanning microscope*. Ultramicroscopy, 2009. **109(6)**: p. 748-757.
14. Morgan, J., et al., *An Introduction to the Helium Ion Microscope*. Microscopy Today, 2006. **14(4)**: p. 24-30.
15. Vladár, A.E., M.T. Postek, and B. Ming, *On the Sub-Nanometer Resolution of Scanning Electron and Helium Ion Microscopes*. Microscopy Today, 2009. **17**: p. 6.
16. Scipioni, L., et al., *Understanding imaging modes in the helium ion microscope*. J. Vac. Sci. Technol. B, 2009. **27**.
17. Postek, M.T., A.E. Vladár, and B. Ming, *Recent progress in understanding the imaging and metrology using the helium ion microscope*, in Proc. SPIE, M.T. Postek, et al., Editors. 2009, SPIE: Monterey, CA, USA. p. 737808-10.
18. Postek, M.T., et al., *Review of current progress in nanometrology with the helium ion microscope*. Meas. Sci. Technol., 2011. **22(2)**.
19. Alkemade, P.F.A., et al., *Model for nanopillar growth by focused helium*



*ion-beam-induced deposition*. Journal of Vacuum Science & Technology B: Microelectronics and Nanometer Structures, 2010. **28(6)**: p. C6F22-C6F25.

20. Maas, D.J., et al., *Nanofabrication with a helium ion microscope*. SPIE Metrology, Inspection, and Process Control for Microlithography XXIV 2010. **7638**: p. 763814.

21. van Beek, P.J.G., et al., *Acoustic immunity improvement for the Helium Ion Microscope* - Private communication.

22. Tseng, A.A., et al., *Electron beam lithography in nanoscale fabrication: recent development*. Ieee Transactions on Electronics Packaging Manufacturing, 2003. **26(2)**: p. 141-149.

23. LayoutBeamer.

24. Martin, C.A., et al., *A versatile low-temperature setup for the electrical characterization of single-molecule junctions*. Review of Scientific Instruments, 2011. **82(5)**.

25. ADwin. Available from: <http://www.adwin.de>.

26. Levesque, T., Leckenby, J., *Application of Plasma Cleaning Technology in Microscopy*: XEI Scientific.



# 3

## CHAPTER 3

### ***In situ* transmission electron microscopy imaging of grain growth in a platinum nanobridge induced by electric current annealing**

*An in situ transmission electron microscopy (TEM) study of grain growth in a Pt nanobridge induced by a high electric current density is reported. The change in morphology at the nanoscale is recorded in real time together with the electrical characterization of the Pt nanobridge. We find a drop in the resistance as the voltage across the bridge is increased; TEM inspection shows that this coincides with thermally induced grain growth, indicating that a reduction of grain boundary scattering is the cause of the resistance decrease.*

---

The work presented in this Chapter has been published as Gao, B., Rudneva, M., McGarrity, K., Xu, Q., Prins, E., Thijssen, J. M., Zandbergen, H. W. and van der Zant, H. S.J *In situ transmission electron microscopy imaging of grain growth in a platinum nanobridge induced by electric current annealing*. *Nanotechnology*, 2011 **22**(20).

### 3.1 INTRODUCTION

It is well known that the grain size of a material is an important parameter influencing its mechanical and electrical properties. Consequently, grain growth and its prevention have been studied extensively, in particular for metals. Often this was done phenomenologically and although widely studied [1-5] still much progress can be made. The need for fine tuning of material properties and continuing miniaturization of components demand a more thorough understanding of the physical and chemical processes involved in grain growth.

In the grain growth of thin metallic layers (e.g. 5–50 nm thick), the quasi-two-dimensional character can play an important role, since the two interfaces, one with the substrate and the other one with another material, air or vacuum, will influence the grain growth and will favor certain crystallographic orientations. Recently, a few *in situ* observations of grain growth have been reported. By combining the thermal annealing with real-time x-ray diffraction (XRD)[6], transmission electron microscopy (TEM)[7, 8] or scanning tunneling microscopy (STM) measurements[9], the evolution of grain size can be followed even with atomic resolution.

A resistance drop has been observed during our study of nanogaps formation in Pt nanobridges using the electromigration technique. *Ex situ* TEM measurements before and after the resistance drop show an increase in the grain size. This grain growth can be, in principle, the result of the local Joule heating caused by the electric current. Here, this process is called electric current annealing (ECA). ECA has been used to tune the grain growth and control the drifting of domain walls [10-13]. It is also a powerful tool used in fabrication of structures such as nanogaps and nanofilaments [14-16] beyond the limit of traditional techniques such as, for example, electron beam lithography. In order to correlate the grain growth with the measured resistance change an *in situ* TEM study have been performed where we measured the electrical properties of Pt nanobridges while imaging it. Numerical simulations to model our experimental findings were performed. Both the experimental and the numerical studies are reported in this chapter.

### 3.2 SAMPLE PREPARATION

Pt nanobridges were made on a pre-fabricated silicon nitride membrane substrate using electron beam lithography (EBL) followed by metal evaporation. One hundred nanometers thick N deficient low stress silicon nitride layers were grown on both sides of the silicon substrate using low-pressure chemical vapor deposition (LPCVD). The free-standing SiN membrane was made by a two-step etching

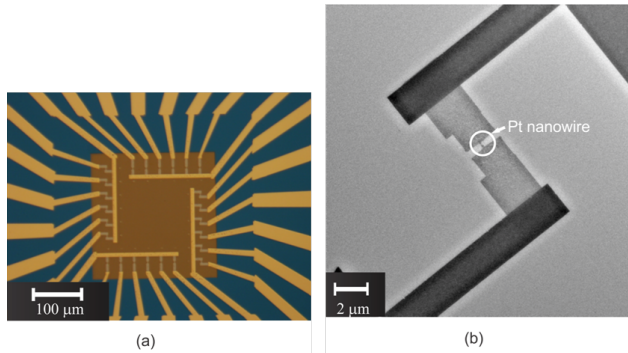


FIGURE 3.1: (a) Top view of the specimen (optical image). The central square is the silicon nitride membrane substrate that was originally 100 nm thick. Pt nanobridges and gold contact leads/pads were patterned onto the substrate using conventional EBL. (b) TEM image of a Pt nanobridge. The Pt nanobridge indicated by the white circle in the image has a size of  $300 \times 200 \times 14$  nm.

process: first, a PMMA mask was patterned on the top surface of the substrate by EBL, then the exposed SiN layer was removed by an anisotropic low-pressure reactive ion etching in a LHZ 400 system using the recipe:  $\text{CHF}_3/\text{O}_2$ , gas flow 50/2.5 sccm, chamber pressure 8 μbar and forward power 50 W; second, the remaining SiN was used as the mask for the following KOH wet etching, which produced the anisotropic V-shaped etching profile. The Pt nanobridges were then patterned on the membrane substrate. In some cases it is necessary to improve the electron transparency of the SiN membrane. For that membrane was dry etched from the bottom side in the LHZ 400 system using the following process:  $\text{CHF}_3/\text{Ar}$  plasma, gas flow 25.0/16.8 sccm, chamber pressure 6.7 μbar and forward power 50 W. As a result, samples with thickness of the SiN membrane varying from 20 nm to 100 nm (original thickness) were used in experiments described below. The geometry of the sample is shown in Figure 3.1. The dimensions of the Pt nanobridge are  $300 \times 200 \times 14$  nm. More details of sample fabrication are given in the **Chapter 2** and in [17]. After dry etching, sample was glued to an  $\text{Al}_2\text{O}_3$  chip carrier and then mounted onto a TEM holder with electric connections. The electrical measurements were performed with a high-speed analog/digital–digital/analog converter (ADwin-Gold I) and homemade voltage divider/current amplifier. The setup is similar to the previous electromigration experiments on gold nanowires described in [18].

### 3.3 RESULTS AND DISCUSSIONS

First, we performed ECA on more than 20 different Pt bridges. TEM images were taken before and after the annealing. The annealing was achieved through a bias ramping process, where the current density (in the order of  $10^{11}$  Am<sup>-2</sup>), ramping rate (1–1000 mV s<sup>-1</sup>) and the use of feed-back control all contributed to the process. In all the devices we observed two common phenomena. The first one was the increase in the grain size. Figure 3.2(a) shows a Pt nanobridge before the annealing; it was composed of many small Pt grains with an average radius of about 4 nm. After the ECA, large grains with an average radius greater than 10 nm were present in the bridge, as shown in Figure 3.2(b). Note that for larger currents/voltages the bridge eventually breaks due to electromigration. ECA was carried out at sample holder temperatures of 300 K (room temperature) and at ~100 K (cooling with liquid nitrogen). It was noticed that environmental temperature does not have a sizable impact on the grain growth process. However performing experiments at lower temperature allows to prevent formation of carbon contaminations rings in the illumination area, which might influence the electrical measurements (see discussion in **Chapter 2**).

The second phenomenon was a kink in the I–V curve, which indicates the onset of the grain growth. Figure 3.2(c) shows a typical example where a kink is present in the I–V curve. After an initial downward bending (i.e. a resistance increase) associated with Joule heating, the I–V curve shows an unexpected upward bending around 0.3 V. The differential resistance curve in Figure 3.2(d) shows clearly appearance of characteristic peak at voltage values of 220–250 mV and subsequent drop of the resistance induced by grain growth in a sample (see discussion below). At 350 mV the local minimum is reached and then resistance starts to rise again due to suppression of grain growth and increase of influence of Joule heating. The voltage at which this minimum occurs differs from sample to sample; we observed the values ranging from 0.15 to 0.6 V. Since the differential resistance is affected by temperature increase due to Joule heating, we measured the low-bias resistance of the Pt nanobridge before and after ECA. The low-bias resistance is obtained from the linear fitting of the I–V curve in which the bias is ramped from 0 to 100 mV. The inset of Figure 3.2(d) shows the ratio of the low-bias resistance ( $R_{min}$ ) that was reached after annealing to the resistance of initial bridge ( $R_{ini}$ ). Annealing was carried out through a few rounds of ECA. In each loop the maximum value of bias ramping voltage was slightly increased and consequently low-bias resistance was measured at the end. Both resistances  $R_{ini}$  and  $R_{min}$  were measured at the same

environment temperature. In the inset we plot this ratio for the 20 samples studied. On average a drop in resistance of about 30% is observed.

In order to have a direct correlation between the evolution of the grain size and the resistance variation, *in situ* TEM imaging with a FEI Titan was performed. The sample was annealed in an environment at liquid nitrogen temperature. Annealing was realized by ramping the bias voltage from zero to 400 mV and then back to zero. The bias ramping rate was 8.3 mV/s. The I–V plot of the annealing process is shown in Figure 3.3(a). The solid lines in the figure represent the upward and the downward sweeps respectively. A resistance drop similar to the one in Figure 3.2(c) is present.

The ECA process was monitored *in situ* by focusing on a local area in the nanobridge of about 5000 nm<sup>2</sup>. The grain growth was accurately followed, a movie was recorded and a few selected snapshots from the movie are presented in Figures 3.4(a)–(g). Figure 3.4(h) shows an overview of the whole Pt nanobridge after annealing. The observed significant changes in microstructure of the bridge occurred very quickly, however the geometry of the bridge after annealing remained very similar to its initial state. Therefore, it can be concluded that the electromigration effect did not play an important role in this experiment.

The number of grains as a function of time was also analyzed. Since the bias voltage ramping rate and the maximum applied voltage were known, time dependency could be replaced with voltage dependency, as shown in Figure 3.3(b). The initial number of grains was 101. At low bias, it remained constant. The small fluctuations were due to the noise in the movie and the changes in the visibility of the grains due to focus changes resulting from current changes. At about 170 mV the number of grains started to drop quickly. As the voltage reaches about 290 mV, the drop slowed down. Finally it converged to a value of about 20 as the voltage reached the maximum. The number of grains did not change during the downward ramping. Figures 3.3(a) and (b) show the close relation between the grain growth and the resistance variation in the Pt nanobridge. We have seen from Figure 3.3(b) that the number of grains does not decrease until the voltage reaches 170 mV. This suggests that an energy barrier must be overcome before the grain growth can start. This agrees with the resistance change shown in the inset of Figure 3.3(a), where a resistance peak also appears around 170 mV. It means that up to this voltage, Joule heating still dominates the resistance change. Above 170 mV, grain growth takes place so that the resistance change depends on Joule heating as well as on the grain growth. Joule heating leads to resistance increase, and the grain growth tends to

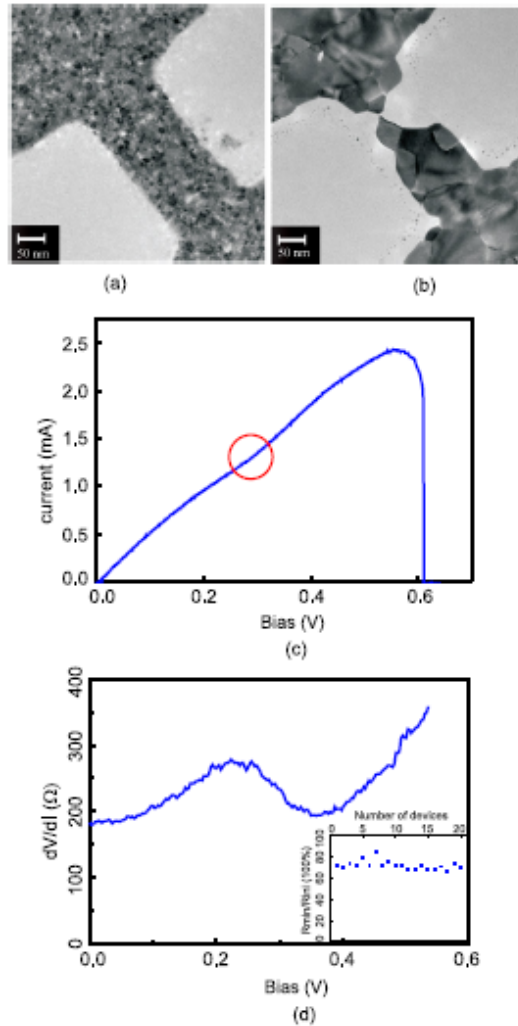


FIGURE 3.2: (a) TEM image of a single Pt nanobridge prior to applying a current. (b) The same Pt nanobridge exposed to high density electric current. Large grains were formed. (c) The I - V plot that describes an ECA process. The red circle denotes the resistance drop of the Pt nanobridge. The final drop of the current corresponds to the breaking of the bridge due to electromigration. (d) The differential resistance of the Pt nanobridge calculated from the I - V curve shown in (c). The initial increase of the resistance is due to Joule heating, followed by a resistance drop because of grain growth. The inset shows the ratio of the Pt nanobridge minimum resistance after annealing to its initial resistance.



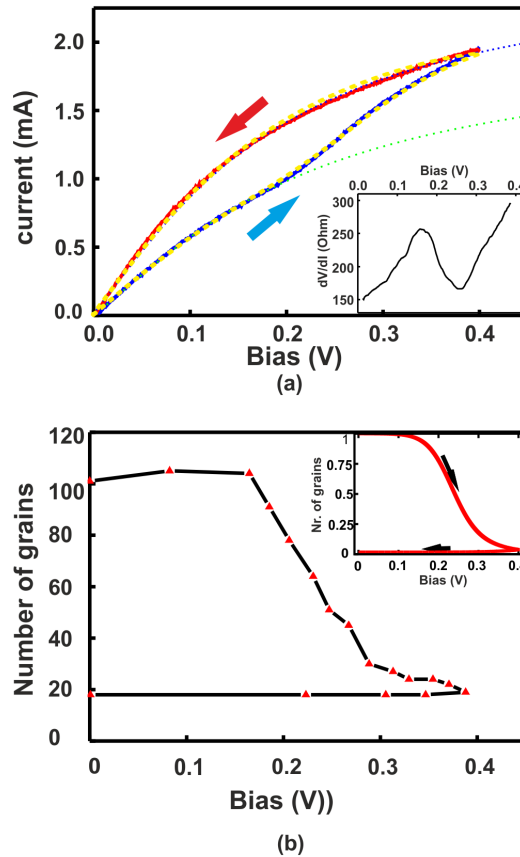


FIGURE 3.3: (a) The I - V curves (solid lines) corresponding to an ECA loop with *in situ* TEM imaging. The upward and the downward arrows denote the directions of the bias ramping. The hysteresis indicates permanent changes taking place inside the bridge, and reflects the grain growth shown in the following Figures 3.4(a)-(g). Dotted and dashed lines are the fits of the experimental data. The dotted lines show the fits by keeping the number of grains constant. The dashed line shows the fit that takes into account the evolution of the number of grains. The inset shows the resistance ( $dV/dI$ ) plot of the upward ramping I - V curve. (b) The evolution of the number of grains as a function of the applied voltage. The number of grains is counted manually from the corresponding annealing movies. The inset shows the theoretical modeling of the annealing based on equation (1), in which the number of grains has arbitrary units.

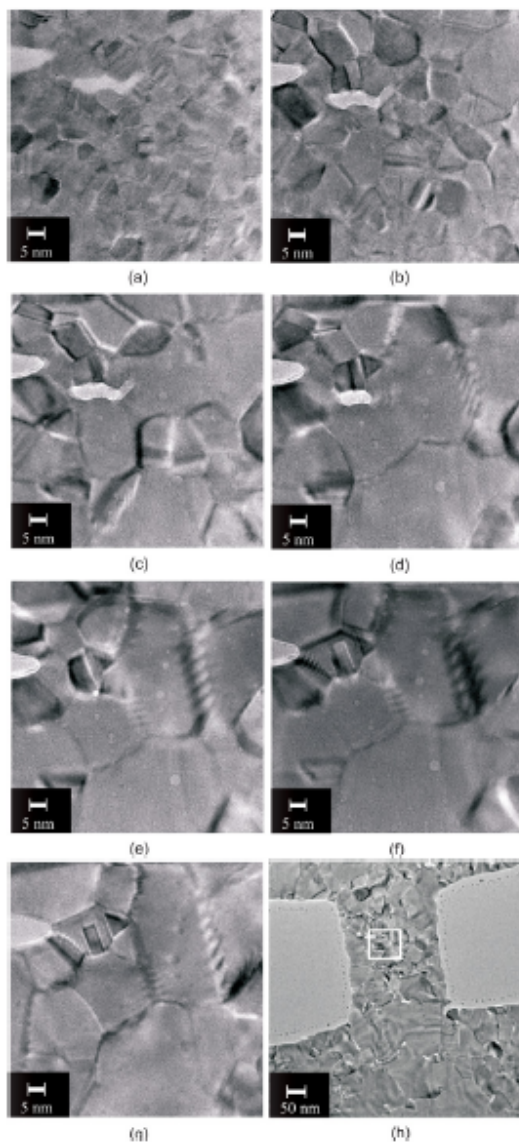


FIGURE 3.4: (a)-(g) Images of grain growth process during ECA of sample 1, captured at 0 s, 30 s, 35 s, 45 s, 50 s, 55 s, and 97 s, respectively. (h) Overview of the whole Pt nanobridge after ECA. The images shown above were taken from the local part of the bridge indicated by the white square.

decrease the resistance due to less grain boundary scattering. With further increase in voltage, the grain growth eventually slows down and Joule heating dominates the resistance change again. As shown in the inset of Figure 3.3(a), the resistance rises again around 270 mV, which agrees qualitatively with the slowing down of grain growth at 290 mV. The grain grows slow down and its final halting indicates that further growth is energetically unfavorable. The downward ramping of the I-V curve demonstrates the expected slight bending due to the termination of annealing as the wire cooled and linear behavior at small voltages. Possible explanations for the grain growth stagnation are the film thickness effect [19], pinning by thermal grooves [20] and presence of smooth boundaries in the sample, demonstrating the slow mobility [5]. However, the exact stopping mechanism is not yet clear. From the above analysis, we can see that there is qualitatively a one-to-one correlation between the number of grains and the resistance of the bridge. It suggests that one can use the resistance measurements to probe the situation of grain growth in the case where direct microscopic inspection is not accessible. However, since Joule heating also influences the bridge resistance, the simple analysis shown above is not able to generate a quantitative description of the correlation between grain growth and resistance change. Below, we develop a mathematical model to describe our experimental findings quantitatively.

### 3.4 SIMULATION

The mechanisms responsible for the observed behavior of the I-V characteristics are (i) temperature dependent grain growth, (ii) resistance increase with temperature and (iii) Joule heating. In this section it is shown that if these mechanisms can be incorporated into a simple model, the experiment can be reproduced quite well using only a few fitting parameters. In the simulation the platinum nanobridge was represented as a realistic polycrystalline structure with an underlying Ohmic resistor network [21]. The parameters used in simulation are taken from known material values. Esen demonstrated that Joule heating leads to reversible changes in resistance of a gold nanowire. In turn, electromigration causes an irreversible change in resistance [18, 22]. Our experiments show that an irreversible change in resistance was observed in platinum even before electromigration. The model is aimed to analyze the annealing due to Joule heating and its effect on the resistance. Time evolution of the grain size is simulated using the normal grain growth model for the linear domain size  $r$  [23]:

$$\frac{dr}{dx} = m_0 e^{\frac{-E_a}{k_b T}} \frac{1}{r} \quad (3.1)$$

(1) where  $m_0$  is the average grain boundary mobility and the activation factor  $e^{-E_a/k_b T}$  takes the temperature dependence of the mobility of the atoms in the contact into account.  $Q$  is a measure for the energy barrier that atoms near a grain boundary have to overcome before they can move to a different location. Joule heating is calculated from the bias voltage and resistance, where the latter varies due to temperature effects and due to the decreasing number of grains in the sample. The current along the bridge encounters  $\sim \sqrt{N}$  such boundaries (in two dimensions) where  $N$  is the number of grains, which leads to a total resistance of  $R = R_0(T) + B\sqrt{N}$ . The Joule heating is compensated by heat loss to the environment, the rate of which is  $\gamma(T - T_0)$ , where  $T$  is the sample temperature and  $T_0$  is the environment temperature (77 K). The balance between the heat loss and the Joule heating directly gives the temperature for each bias voltage and grain number.

The fit parameters used in the simulation are (i) the parameter  $B$  specifying the difference between the resistivity in bulk and across a grain boundary, (ii) the heat loss rate  $\gamma$  and (iii) the activation energy  $Q$ . For the temperature coefficient of the resistance, a value of  $0.002 \text{ K}^{-1}$  was used, which is about half the macroscopic bulk value from the literature [24]. This choice was based on several experimental observations on nanoscale wires, where this parameter is often found to be half the macroscopic bulk value [25, 26]. Natelson even finds a much lower value than the macroscopic bulk value in measurements on a Pt nanobridge [27].

If the number of grains is kept constant, the equations become particularly simple. In Figure 3.3(a) the resulting analytic expression is fitted to the experimental results for the initial ramp-up of the voltage and the full down-ramp to zero. The fitting parameters for the upward ramp (green dots in Figure 3.3(a)) are:  $\gamma = 1.1 * 10^{-6} \text{ JK}^{-1} \text{ s}^{-1}$  and  $b = 153.1 \text{ } \Omega$ ; for the downward ramp (blue dots):  $\gamma = 1.1 * 10^{-6} \text{ JK}^{-1} \text{ s}^{-1}$  and  $b = 98.12 \text{ } \Omega$ . These parameters give very close fits (Figure 3.3(a)), indicating that the number of grains is relatively constant during these stages. The zero-temperature resistance  $b = R_0(T_0) + B/r$ , which goes into the fit as a single parameter, drops about 35% before and after the domain growth, as is expected in view of the observed 30% drop in resistance (including the contacts) before and after annealing. To fit the full upward and the downward ramp, the annealing effect is included in equation (1) using the temperature calculated from the heat balance. The parameter  $\gamma = 1.1 * 10^{-6} \text{ JK}^{-1} \text{ s}^{-1}$  is applied that was also used in the previous fit plus a few new ones:  $Q = 1450 \text{ kB K}$ ,  $R_0(T_0) = 72 \text{ } \Omega$ ;  $B = 90$  (unit set by the dimension of  $r$ ). Then curves are obtained that are in good agreement between the simulations and the experimental results over the entire curve, see Figure

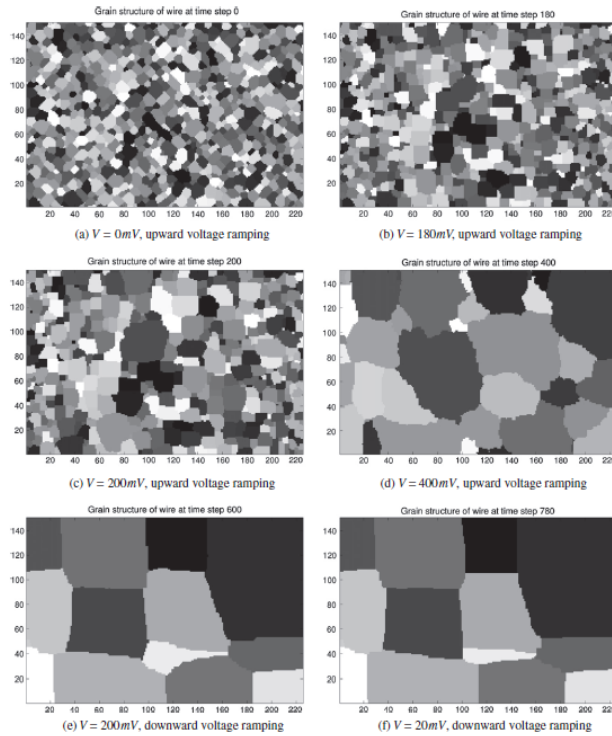


FIGURE 3.5: Snapshots of the simulated grain growth in the bridge at various time steps. Current is flowing from left to right in all images (courtesy of K. McGarrity [21]).

3.3(a). The maximum temperature reached in the simulation is 900 K. Simulation shows [21] that annealing starts when local temperatures reach between 400 K and 500 K, quantitatively matching experimental observations. Natelson [27] found that during electromigration, temperatures around 1000 K are obtained. At such temperatures the bridge in our experiment does not yet exhibit electromigration. The simulated effect of annealing on the bridge can be seen in Figure 3.5. To initialize grain growth in the wire, the temperature needs to be high enough to overcome the energy barrier. The grain size development as seen in the simulated images is in good agreement with the one observed in the experiment (Figure 3.4). The calculation of the average temperature at each site in the lattice as a function of bias voltage is presented at Figure 3.6 [21]. The temperature distribution throughout the

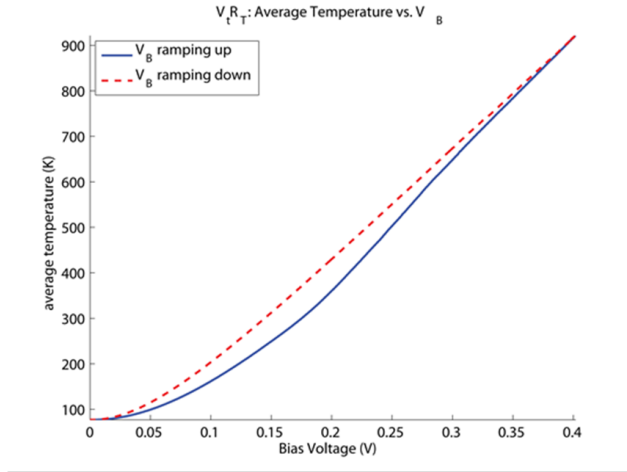


FIGURE 3.6: Average temperature versus bias voltage [21].

lattice is parabolic with the highest temperature reached in the middle of the bridge. McGarrity simulated the impact of annealing on the resistance without the interference of Joule heating [21]. For that the initial resistance of the bridge was calculated and then the grain structure was measured at various time steps during the annealing process at the bias voltage of 1 mV and temperature of 77 K. This method can be used for a direct comparison of the resistance only due to the annealing. Obtained simulated results correspond quantitatively with the experimentally observed drop in resistance of 30%.

Presented model demonstrates that Joule heating is significant enough to drive grain annealing and that annealing is responsible for the irreversible drop in resistance observed in the experiment.

### IN SITU STUDY OF GRAIN GROWTH IN THIN POLYCRYSTALLINE PT FILM INDUCED BY EXTERNAL HEATING

In bulk platinum annealing begins around 800 K [28]. However for nanoscale structures this value is expected to be substantially lower (about 500 K) [29]. For the experiments, described above, Joule heating due to the current passing in the bridge is considered to be the main driving force for annealing. This is due to the fact that the experiments were performed in the ultra-high vacuum chamber of the

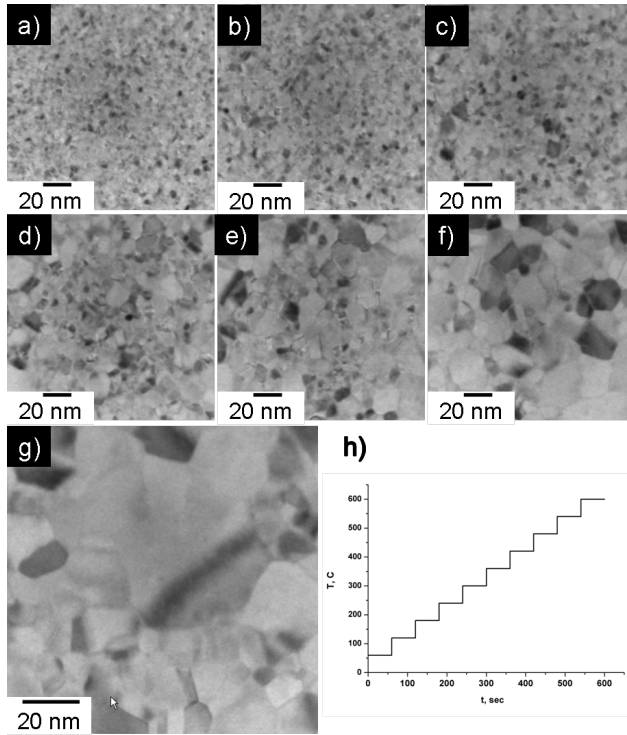


FIGURE 3.7: Set of images captured from the annealing movie at temperatures (a) 60°C; (b) 240°C; (c) 300°C; (d) 360°C; (e) 420°C; (f) 480°C; (g) 540°C; (h) temperature profile for the annealing process.

TEM and samples were cooled down with liquid nitrogen (to  $\sim 100$  K). To analyze whether the increase of the temperature required for annealing can be gained by Joule heating only, we carried out heating experiment on thin platinum film deposited onto a MEMS based heater. Up till now it was not possible to measure the temperature of the bridge directly in the TEM during the current induced annealing process. The temperature in that case has only been predicted from blackbody radiation measurements [27]. The use of calibrated heater combined with *in situ* TEM observation of the grain growth allows to capture quantitatively the relation between the input bias voltage and the temperature of the wire. In order to define the temperature, required for initiation of grain growth, 15nm thick Pt film was deposited using sputtering method onto a MEMS based heater chip. The structure

and thickness of the sample are similar to ones in the experiments and simulations described above. A heating element is embedded into thick SiN membrane and has four electrical outputs allowing to set and to control temperature of the heater. The membrane has areas of thinning-out with thicknesses of  $\sim 20$  nm, enabling TEM observation of ongoing processes. After Pt deposition MEMS heater was loaded into the TEM chamber using a special heating holder.

Initially, the temperature of the heater was set to  $60^\circ\text{C}$  and then increased in steps of  $60^\circ\text{C}$  every 1 minute. The grain growth process was followed *in situ* and recorded from fluorescent screen using Camtasia software [30]. At  $240^\circ\text{C}$  first trace of grain growth is observed (Figure 3.7), which is in good agreement with temperature values mentioned in literature and simulations [21, 29], though negligible number of grains was affected, compare to the total amount of grains. At  $300^\circ\text{C}$  significant grain growth is observed in the sample, suggesting that this temperature is already high enough to overcome the energy barrier for majority of grain orientations. Further increase of the temperature leads to subsequent increase of the grains sizes. Starting with average grain size of 5nm, thermal annealing leads to formation of 20–100 nm wide grains, which far exceeds the thickness of the film. Certainly, if one wants to utilize the described method for one-to-one correlation between applied voltage and the temperature of the sample, one should be aware of the effect of sample and membrane thicknesses and samples geometry on the obtained results. In our case difference is thicknesses of the underlying membrane for current induced annealing and thermal annealing can be neglected.

### 3.5 SUMMARY

The bias voltage, applied to the polycrystalline platinum bridges causes a current flow which generates Joule heating. Heating of the bridge leads to increase of resistance of the sample with the temperature. At voltage values of about 200 mV for the specified geometry of the bridge ( $200 \times 300 \times 15$  nm) the temperature of the system is high enough to activate the annealing process which in turn results in change of samples structure (grain growth). With dropping of the number of grains and increasing of their average size, the overall resistance starts to decrease significantly, despite the rising of the temperature. I–V curve of the process reflects the drop in resistance having a slight kink around 200–250 mV (see Figures 3.2(c), 3.3(a)). *In situ* TEM observation shows (Figures 3.4, 3.3(b)) that about total number of grains is reduced substantially in this voltage range and at higher voltage values the loss of grain boundaries through annealing is not able to compensate for Joule



heating and so the overall resistance begins to increase again. The results of the simulation match quantitatively with the experiment.

### 3.6 CONCLUSIONS

We have performed *in situ* TEM imaging with electric measurements of Pt nano-bridges. A one-to-one correlation was obtained between the change in resistance and the observed grain growth. A simple model based on Joule heating and grain boundary scattering as the dominant source for the resistance was used to reproduce the measured current-voltage curves. Given the simplicity of the model, the agreement with the experiment is reasonable and confirms that annealing is responsible for the observed change in resistance. Our results suggest that it is possible to use the resistance measurement to probe the grain growth in nanobridges.

### 3.7 ACKNOWLEDGEMENTS

I would like to thank Kimberly McGarrity and Prof. J. Thijsen for the simulations of the behavior of polycrystalline platinum samples, performed in this work.

### 3.8 REFERENCES

1. Offerman, S.E., et al., *Grain nucleation and growth during phase transformations*. Science, 2002. **298(5595)**: p. 1003-1005.
2. Schmidt, S., et al., *Watching the growth of bulk grains during recrystallization of deformed metals*. Science, 2004. **305(5681)**: p. 229-232.
3. MacPherson, R.D. and D.J. Srolovitz, *The von Neumann relation generalized to coarsening of three-dimensional microstructures*. Nature, 2007. **446(7139)**: p. 1053-1055.
4. Van Petegem, S., et al., *On the Microstructure of Nanoporous Gold: An X-ray Diffraction Study*. Nano Letters, 2009. **9(3)**: p. 1158-1163.
5. Holm, E.A. and S.M. Foiles, *How Grain Growth Stops: A Mechanism for Grain-Growth Stagnation in Pure Materials*. Science, 2010. **328(5982)**: p. 1138-1141.
6. Seibt, M., et al., *Nanoscale observation of a grain boundary related growth mode in thin film reactions*. Physical Review Letters, 1998. **80(4)**: p. 774-777.
7. Simoes, S., et al., *In situ TEM study of grain growth in nanocrystalline copper thin films*. Nanotechnology, 2010. **21(14)**.
8. Sharon, J.A., et al., *Stress-driven grain growth in nanocrystalline Pt thin films*. Scripta Materialia, 2011. **64(1)**: p. 25-28.

9. Agustsson, J.S., et al., *Growth, coalescence, and electrical resistivity of thin Pt films grown by dc magnetron sputtering on SiO<sub>2</sub>*. Applied Surface Science, 2008. **254(22)**: p. 7356-7360.
10. Conrad, H., *Effects of electric current on solid state phase transformations in metals*. Materials Science and Engineering a-Structural Materials Properties Microstructure and Processing, 2000. **287(2)**: p. 227-237.
11. Yu, C.H., et al., *Ultrafast directional nickel-silicide-induced crystallization of amorphous silicon under high-density current stressing*. Applied Physics Letters, 2003. **82(12)**: p. 1857-1859.
12. Rogozin, A., et al., *Annealing of indium tin oxide films by electric current: Properties and structure evolution*. Applied Physics Letters, 2006. **89(6)**.
13. Gu, Q., et al., *Current-driven phase oscillation and domain-wall propagation in WxV1-xO<sub>2</sub> nanobeams*. Nano Letters, 2007. **7(2)**: p. 363-366.
14. Strachan, D.R., et al., *Clean electromigrated nanogaps imaged by transmission electron microscopy*. Nano Letters, 2006. **6(3)**: p. 441-444.
15. Taychatanapat, T., et al., *Imaging electromigration during the formation of break junctions*. Nano Letters, 2007. **7(3)**: p. 652-656.
16. Lee, M.J., et al., *Electrical Manipulation of Nanofilaments in Transition-Metal Oxides for Resistance-Based Memory*. Nano Letters, 2009. **9(4)**: p. 1476-1481.
17. Gao, B., et al., *Three-terminal electric transport measurements on gold nanoparticles combined with ex situ TEM inspection*. Nanotechnology, 2009. **20(41)**.
18. Heersche, H.B., et al., *In situ imaging of electromigration-induced nanogap formation by transmission electron microscopy*. Applied Physics Letters, 2007. **91(7)**.
19. Burke, J.E. and D. Turnbull, *Recrystallization and Grain Growth*. Progress in Metal Physics, 1952. **3**: p. 220-292.
20. Mullins, W.W., *The Effect of Thermal Grooving on Grain Boundary Motion*. Acta Metallurgica, 1958. **6(6)**: p. 414-427.
21. McGarrity, K.S., B. Gao, and J.M. Thijssen, *Simulation of Joule annealing in nanoscale Pt wires*. Computational Materials Science, 2011. **50(10)**: p. 3043-3049.
22. Esen, G. and M.S. Fuhrer, *Temperature control of electromigration to form gold nanogap junctions*. Applied Physics Letters, 2005. **87(26)**.
23. Thompson, C.V., *Structure evolution during processing of polycrystalline films*. Annual Review of Materials Science, 2000. **30**: p. 159-190.
24. Glazkov, S.Y., *Point-Defect Formation and Temperature-Coefficient of Electrical-Resistivity of Platinum and Platinum-(10 Wt-Percent) Rhodium Alloy in the Range 1100-1900-K*. International Journal of Thermophysics, 1985. **6(4)**: p. 421-426.

- 
25. Lacy, F., *Developing a theoretical relationship between electrical resistivity, temperature, and film thickness for conductors*. Nanoscale Research Letters, 2011. **6**: p. 1-14.
26. Zhang, X., et al., *Thermal and electrical properties of a suspended nanoscale thin film*. International Journal of Thermophysics, 2007. **28(1)**: p. 33-43.
27. Ward, D.R., N.J. Halas, and D. Natelson, *Localized heating in nanoscale Pt constrictions measured using blackbody radiation emission*. Applied Physics Letters, 2008. **93(21)**. 28. Platinum Metals Reveiw, 2010.
29. Tschope, A., R. Birringer, and H. Gleiter, *Calorimetric Measurements of the Thermal Relaxation in Nanocrystalline Platinum*. Journal of Applied Physics, 1992. **71(11)**: p. 5391-5394.
30. Camtasia studio. Available from: <http://www.techsmith.com/index.html>.



# 4

## CHAPTER 4

### **In situ transmission electron microscopy imaging of electromigration in Pt nanowires**

*The phenomenon of electromigration with and without feedback control in Pt nanowires (14 nm thick, 200 nm wide and 300 nm long) was analyzed using in situ transmission electron microscopy. Symmetric electrodes are obtained in the feedback control mode while the gap usually forms at the center of the Pt nanowire. Without the feedback control asymmetric electrodes are formed and the gap can occur at any position along the wire. The three-dimensional gap geometries of the electrodes in the Pt nanowire were reconstructed using high-angle annular dark-field scanning transmission electron microscopy. The thickness of the nanowire is reduced from 14 nm to only a few atoms at the edge with a gap which is 5-10 nm thick.*

---

The work presented in this Chapter has been accepted for publication as Rudneva, M., Gao, B., Prins, E., Xu Q., van der Zant, H. S. J. and Zandbergen, H. W. *In situ TEM imaging of electromigration in Pt nanowires* *Microscopy and Microanalysis*, 2012.

## 4.1 INTRODUCTION

Electromigration is a mass transport phenomenon induced by the impulse of charge carriers to lattice ions. Electromigration occurs when an electrical current with a density exceeding the threshold value is applied to thin films or nanowires, and is considered to be a main failure mechanism in integrated circuits. Whereas electromigration can be detrimental for contact lines in ICs, it can be used to create nanogaps and to determine the electronic properties of particles or molecules trapped in these nanogaps. For example, a gap which is approximately 1 nm wide has been fabricated using this technique to contact colloidal cadmium selenide nanocrystals [1].

Good control over the shape and size of the gap is essential when fabricating nanogaps to determine the electronic properties of trapped species. If one uses the conventional electromigration technique of uniform voltage increase, the formation of the nanogaps cannot be controlled [1, 2]: one then typically gets a cascade of unpredictable changes in the nanowire. Feedback-controlled electromigration has been developed to get a better control of gap formation, whereby the current is reduced or switched off as soon as a sudden change in resistance is measured [3-5]. Finally, self-breaking schemes have been developed to avoid the formation of spurious metal grains [6, 7] and high temperatures during the trapping of the molecules [4, 8, 9].

Scanning electron microscopy (SEM) and transmission electron microscopy (TEM) imaging have been used to probe the gap formation with a high spatial resolution [2, 10, 11]. A temperature rise during electromigration has also been reported [12-14]. Previous publications on the imaging of nanogaps have focused on electromigration of gold nanowires because gold is often used in molecular electronics [1, 10]. Recently platinum (Pt) has been considered as an alternative material because it produces more stable nanoelectrodes than gold [8, 15]. Direct observation of electromigration in Pt nanowires has not been reported. In this Chapter we present an *in situ* TEM study of electromigration in Pt nanowires. The gap geometries realized with and without feedback control are compared. Furthermore, the stability of the *in situ* measurement setup allows a more detailed investigation of the gap with various TEM techniques and the imaging of the self-breaking process of a Pt nanojunction with atomic resolution. Reversibility of atomic flow direction is discussed in details. The scanning transmission electron microscopy (STEM) imaging was applied to probe the height profile of the nanogap, thereby providing a three-dimensional description of the geometry of the electrodes formed by

electromigration.

## 4.2 MATERIALS AND METHODS

Platinum nanowires were patterned on 100-nm-thick silicon nitride membrane substrates using e-beam lithography [16]. The Pt wire was 300 nm long and had a cross section (width×thickness) of  $200\times 14\text{ nm}^2$ . The total resistance of each device, including the resistance of the leads and the contact pads, was between 150 and 300 Ohm. Before loading into the TEM, the membrane substrate was thinned from the back to a thickness of about 20 nm using reactive ion etching in order to reduce image deterioration by the amorphous  $\text{Si}_3\text{N}_4$  membrane. Imaging was performed with the Titan FEI microscope at 300 kV. The experiments were carried out at temperatures close to 100 K in order to reduce carbon contamination. A custom in-house built sample holder has 8 feedthroughs for performing electrical measurements (see details in **Chapter 2**). The construction of the holder allows connection of chip-like samples to the measurement setup. We performed *in situ* TEM observations of electromigration using two different techniques: a mode with a uniform increase of the voltage (UVI) and a feedback control (FBC) mode. In the UVI mode, the bias voltage applied to the Pt nanowire increases slowly and linearly with time at a rate of about 8.3 mV/s up to the defined  $V_{\text{max}}$  value or until the wire is broken. In the first case the voltage is then lowered down to 0 with the same speed after the  $V_{\text{max}}$  value is reached and then the voltage increase loop is repeated again. In the second case no  $V_{\text{max}}$  value is set in the program and voltage is rising till physical breakdown of the wire occurs. A typical breakdown value for the presented samples is a few hundred millivolts. In FBC mode the wire conductance is constantly monitored while the voltage is sweeping up. If there is a sudden decrease in conductance, the feedback control mechanism reduces the voltage to zero. The process starts again after a new reference conductance is defined. The program stops when a pre-defined conductance value is reached. We investigated a total of 12 samples with UVI and 16 samples with the FBC mode. All electrical measurements were combined with a simultaneous observation of the changes in the wire using a fast scan camera.

## 4.3 RESULTS

Figures 1 and 2 show typical video footage of the gap formation in UVI and FBC modes, respectively. In both cases, the initial Pt wire consists of small grains with an average diameter of 4 - 5 nm. Also in both cases grain growth is observed prior to

changes that can be related to electromigration (see Chapter 3). Obviously the grain growth is due to the temperature rise in the Pt wire and its neighborhood as was previously described [17]. After this initially similar behavior, the changes related to the electromigration process occur differently in UVI and FBC modes. The effect of electromigration in the UVI mode can be seen in Figures 1(d)-1(h). At first, a bottleneck is formed in the upper part of the wire, on the anode side. In Figures 1(e)-1(g), the bottleneck shifts along the wire from the upper right part to the lower left part, which is the cathode side. Finally, a gap is formed near the cathode side of the wire. The electrodes on both sides of the gap are asymmetric. In most cases the anode side has a point-like shape and the cathode side is flat, but other shapes (e.g. two flat electrodes) were also observed, thus indicating that the shape also depends on the local grains and their orientation. Whereas the bottleneck begins roughly in the middle of the nanowire, the location of the final gap was found to be random along the wire between the middle part and the cathode side and was sometimes even observed in the wider region that connects the nanowire with the lead. But in all cases, the bottleneck tends to move towards the cathode side. A similar gap formation was observed for UVI electromigration of gold nanowires [10]. In the case of gold, the anode side is flat and the cathode side is pointed. The difference can be related to the wind force direction. In gold, the charge carriers are electrons and therefore the electron wind force is dominant; similar behavior is observed in platinum, resulting in atomic flow from cathode to anode side and in formation of the nanogap near the cathode side. [18] The effect of electromigration in the FBC mode can be seen in Figures 2(c)-2(f). The narrowing of the nanowire starts almost in the middle of the nanowire and stays there until the wire is broken. As a result a gap with two symmetric electrodes is found. Note that it is possible to correlate changes in the shape of the wire with the applied current (see Figure 4.2(a)). As can be seen in Figure 4.2, each loop on the I-V characteristic corresponds to the particular shape on the bridge. The process of gap formation in the FBC mode is similar to one in alternating current, the main difference being the better control over the gap formation process in the case of FBC (see discussion section).

During the direct observation of the electromigration process one can question whether the direction of atomic motion is governed by current direction or it is chaotic and induced simply by only Joule heating of the sample due to current annealing.

In order to answer this question, we performed a so-called "reversed" electromigration on the Pt nanowires. The process is the following: after the standard voltage



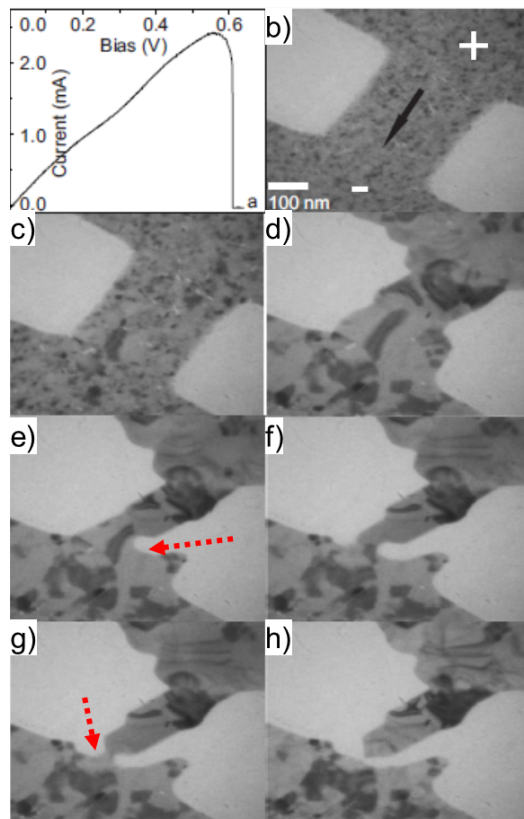


FIGURE 4.1: (a) A current- voltage curve of an electromigration process without feedback control (UVI). The drop of the current signifies the breaking of the wire. (b)-(h) *In situ* TEM imaging of electromigration. (b) The Pt nanowire as fabricated; (c) grain growth taking place in the wire. The rest of the images show that the bottleneck of the wire (marked with red dashed arrows) shifts from the upper right to the lower left, where the final gap is formed. The gap electrodes are asymmetrical. The anode side is sharp and pointy; the cathode side is wide and flat. The arrow in (b) denotes the direction of the current. The scale bar applies to all the figures.

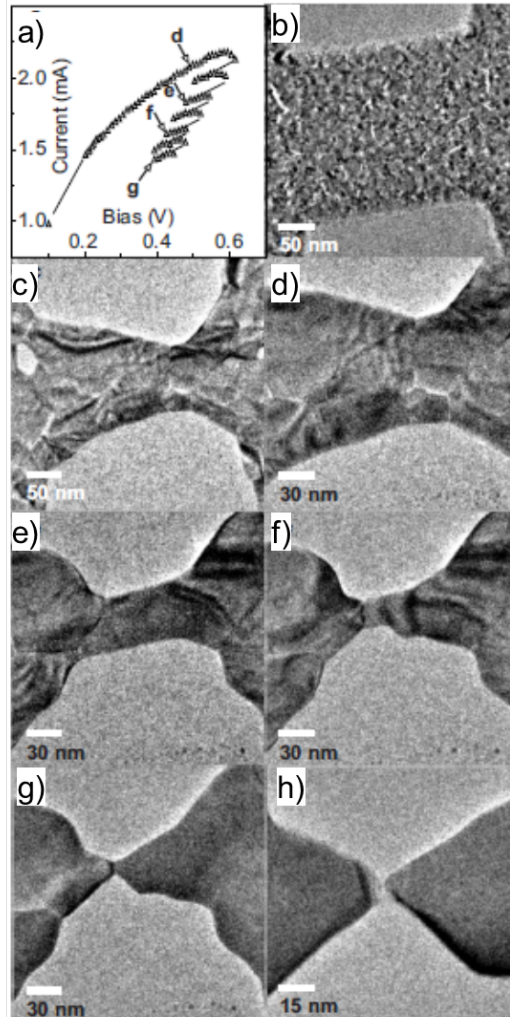


FIGURE 4.2: (a) A current- voltage curve of an electromigration process with feedback control (FBC). Triangles indicate the measured I-V data points; the black lines signify the occurrence of the feedback loop. The I-V curve corresponds to electromigration from image (d) to (g). More precisely, the four locations indicated by the arrow and letter correspond to the respective images below. (b)-(h) *In situ* TEM imaging of electromigration. (b) The original Pt nanowire. The rest of the images show that FBC leads to symmetric electrodes on both sides of the final gap; and the gap in FBC usually appears near the centre of the wire. Reversed electromigration in polycrystalline Pt bridges.

loop in the UVI mode where the bias voltage is increased from 0 to the  $V_{max}$  value and then lowered back to 0, the polarity of the sample and thus the current direction is changed. We repeated such voltage loops many times, slowly increasing the peak voltage value for each subsequent loop. The effect of this "reversed electromigration" on voids formation in Pt bridges was followed *in situ* using TEM and selected frames from the movie presented in Figure 4.3. Starting with the polycrystalline structure with an average grain size of 5 nm, current annealing, described in **Chapter 3**, leads to formation of bigger grains at voltage values of 200–550 mV. The result of such annealing is shown in Figure 4.3(b). Figure 4.3(b)- (c) correspond to the voltage loop with  $V_{max}$  value of 550 mV and no constriction/void formation or further grain development are observed. In Figure 4.3(d) the polarity of the sample was changed and the bias voltage was increased to  $V_{max} = 580$  mV. We observe the formation of small void on the right (cathode) side of the bridge due to electromigration. As the voltage reaches its set peak value electromigration stops. At the downward I-V slope no changes in the sample are observed since current density and temperature of the sample are reduced. Note that the increase of the absolute value of  $V_{max}$  results in formation of even bigger grains. In the Figure 4.3(e)-3(h) the  $V_{max}$  value set to 620 mV. The frames shown in Figure 4.3 reflect the development and propagation of the constriction near the cathode side. When the current direction is changes (Figures 4.3(i) - 4.3(o)) ( $V_{max}$  is still 620 mV) the constriction formed in the previous voltage loop, does not continue to expand to the left side of the bridge. One would expect that breakage will occur in the narrowest area where bottleneck was initially formed during the direct voltage loop. However images show the alteration in the direction of constriction propagation indicating that the direction of atomic flow also reverses. A final constriction is shifted to the cathode side, leading at the end to the gap formation at the right side of the bridge. Schematic view of constriction formation for direct and reversed current is shown in Figure 4.4.

The crystal orientations in the Pt nanowires were studied before and after electromigration. The wire initially has small grains with random orientation. We observed that after the recrystallization and electromigration processes the nanowires contain fewer grains than the primary nanowire. The orientation of the grains after electromigration is analyzed by acquiring diffraction patterns from different parts of the sample. Diffraction patterns are taken from the two different areas labeled A and B in Figure 4.5. As can be seen, the 002, 022, 111 and 113 reflections are present in the non-recrystallized area (Figure 4.5(b)). During recrystallization, all reflec-

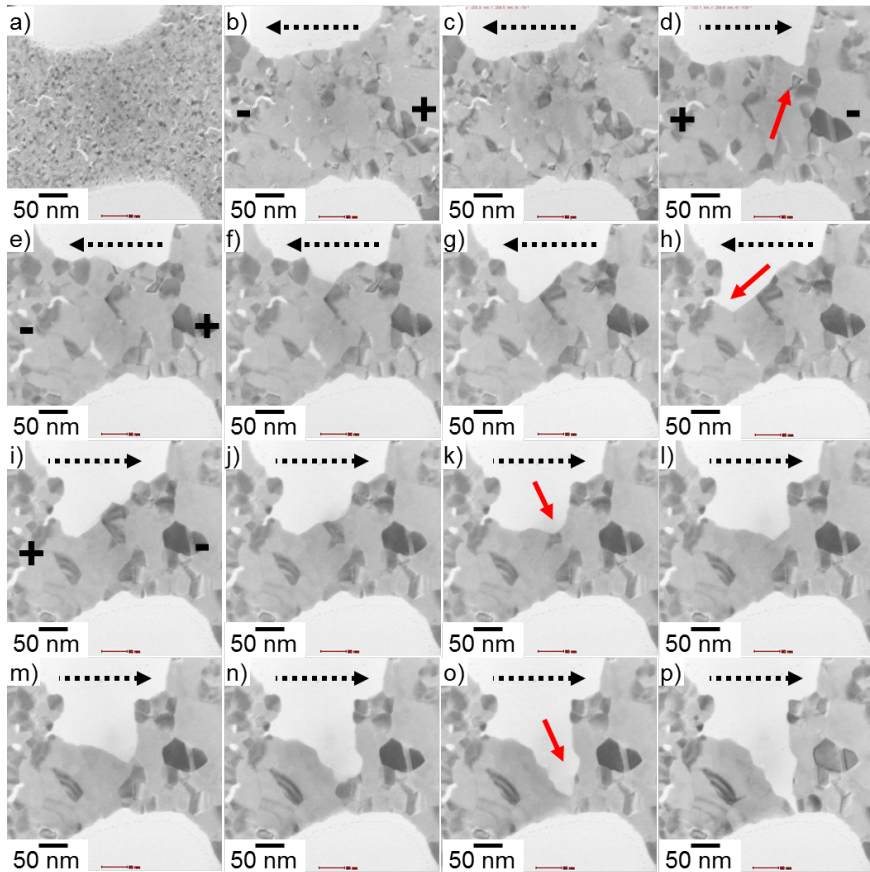


FIGURE 4.3: Reversed electromigration in Pt bridge. (a) The Pt nanowire as fabricated. (b) - (p) *In situ* TEM imaging of the electromigration process for different values of  $V_{max}$  and direction of current flow. Big grains, visible in the picture appeared during subsequent voltage loops. (b) - (c)  $V_{max}$  is 550 mV, no changes in the bridge is observed; (d) Small void, indicated by an arrow, is formed near the cathode side at  $V_{max} = 580$  mV; (e) - (h) Frames corresponding to voltage loop from 0 to  $V_{max} = 620$  mV. The constriction is propagating to the cathode side; (i) - (o) Polarity of the sample was changed and direction of constriction propagation was reversed. Gap is form close to the new cathode side, as shown in Figure 4.3 (p). The dashed arrows in all images denote the direction of the current.

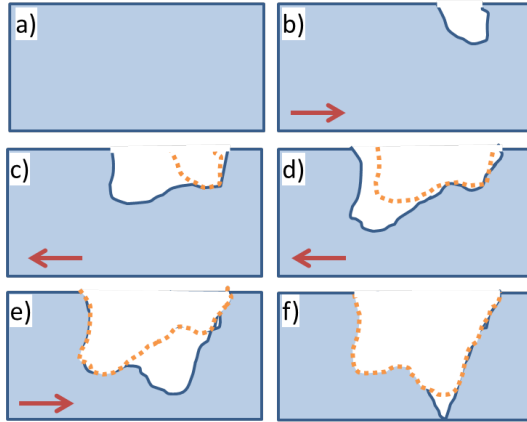


FIGURE 4.4: Formation of the constriction in platinum bridge for different current directions (indicated by red arrow). (a) Original bridge; (b)-(e) Shapes of the bridge at different steps of the experiment. Dashed yellow line reflects the shape of the void formed during previous voltage loop.

tions except those corresponding to the  $[111]$  orientation disappear (Figure 4.5(c)). This shows that most of the grains in area B are oriented close to  $[111]$ .

The self-breaking technique is widely used to prevent the formation of the metal particles in a gap during electromigration [4, 8]. It has been demonstrated that when using the conventional electromigration technique, regardless of the mode (FBC or UVI), there is always a chance that metal particles will be left in the gap. These particles can emit spurious signals. The self-breaking technique, which uses the spontaneous breaking of a metal junction (thinner than 10 nm) due to the stress created in the junction during electromigration, can largely solve the problem. In the case of gold nanowires, it is hard to image the self-breaking process because gold atoms are too mobile under the illumination by the electron beam and thus a gold junction is likely to be changed by the electron beam. Owing to the higher stability of the Pt junction compared with that of gold, it is possible to image the self-breaking of the Pt junction with TEM. Figure 4.6 reveals the evolution of a Pt nanojunction from a few atoms of contact (Figures 6(a) and 6(b)) to a single-atom contact (Figure 4.6(c)), and finally to an open gap (Figure 4.6(d)). The image rate is 20 frames/second, from which we can estimate that the self-breaking takes place on a time scale of hundreds of milliseconds.

Previous papers on Au have provided a description of the two-dimensional

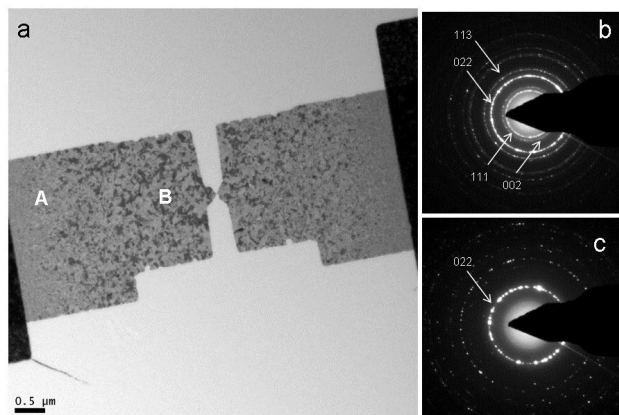


FIGURE 4.5: Distribution of recrystallization in a Pt nanowire. (a) Broken nanowire in the centre and leads to this bridge are both 14 nm thick. The black areas on both sides are thicker gold contact lines. The dark contrast seen is due to recrystallized Pt. (b) and (c) Diffraction patterns taken at A and B, respectively. Area A has the same diffraction pattern as the virgin sample showed for the complete Pt area. Area B shows the presence of the only diffraction rings that occur for [111]-oriented grains

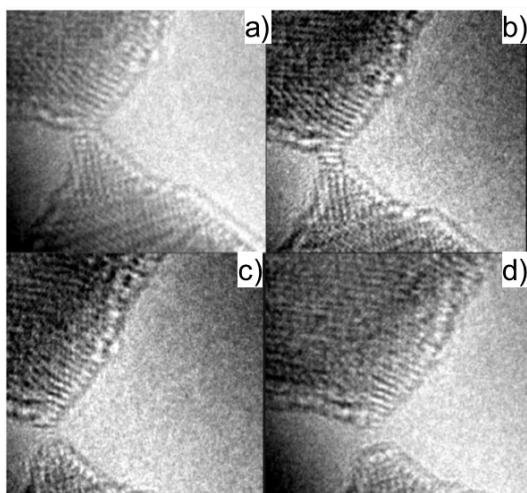


FIGURE 4.6: (a)–(d) Self-breaking of a Pt junction. Images (b), (c) and (d) were taken 150 mS, 200 mS, and 750 mS after image (a).

geometry of the gap [10, 11], but information on the third dimension is still missing. Scanning TEM operated in the high-angle annular dark-field (HAADF) imaging mode can provide such information. The HAADF signal is proportional to the mass thickness of the sample. In our case, the silicon nitride membrane is so thin that it emits only a weak background signal. After subtracting this background signal, the HAADF signal is then proportional to the thickness of the Pt electrodes. Several dark-field STEM images of nanogaps in the FBC mode were recorded. Figure 4.7 shows a typical example of this and the corresponding height profile across the 4-nm-wide gap. The height profile was acquired by taking a 10-pixel wide line profile across the nanogap at the position of the white line. Considering that the film is 14 nm thick, the thickness of the Pt electrode normally drops from 14 nm to 0 nm over a length of 5 to 10 nm. Figures 4.7(b) and 4.7(c) show a 3D representation of this nanogap, which suggests that the narrowest part of the gap is situated directly on the silicon nitride membrane. Figure 4.7(c) is an enlargement of the gap part of Figure 4.7(b). It shows the steep edges of the electrodes near the gap. The electrodes very near the nanogap are only a few atoms thick. The other nanogaps imaged by dark-field STEM showed very similar profiles.

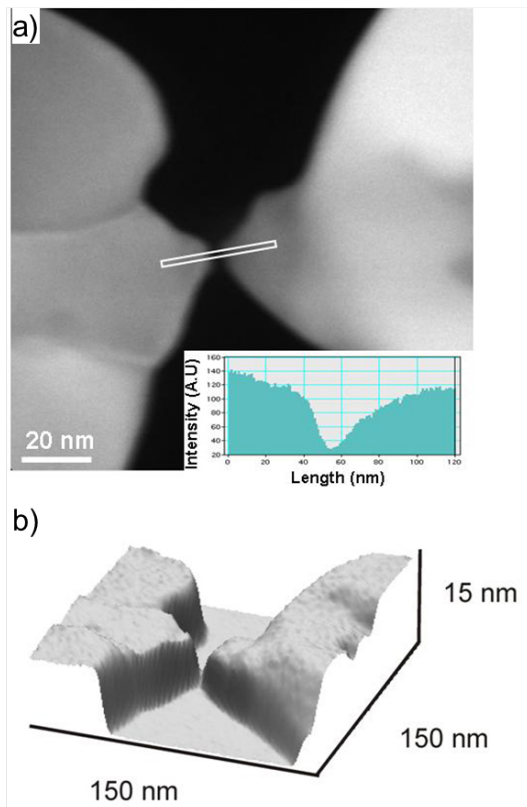


FIGURE 4.7: (a) Scanning TEM image of a nanogap formed using FBC electromigration. The white rectangle defines the area in which the intensity has been integrated. The inset shows the height profile of the broken nanowire across the gap. The thickness of the electrode evolves from nearly zero to 14 nm, which is assumed to be the same as the original thickness of the Pt nanowire. (b) 3D nanogap profile reconstructed from the STEM image in (a).



## 4.4 DISCUSSION

The *in situ* TEM electromigration experiments show clear differences between the two current control procedures. In particular the final results are very different. The gap is asymmetrical in the UVI mode and symmetrical in the FBC mode. The location of the gap is reliably in the middle of the Pt nanowire in the FBC mode, whereas it is at a random position with tendency to shift towards the cathode side for UVI. The position of the gap in the middle of the nanowire in the FBC mode is quite understandable. The narrowing of the nanowire by electromigration will start close to the place where it is the hottest, which will be the middle of the nanowire. Once a constriction has formed, the resistance will increase and the current is decreased to zero according to the programmed FBC procedure. As the current is increased in the following cycle, albeit to the lower peak value, the constriction would once again be preferentially heated, since its resistance is the highest. Thus the further narrowing is very likely to occur at the constriction. After several cycles a gap is formed.

The UVI procedure is identical to the FBC procedure up to the moment when the constriction is formed. Thus it is logical and indeed observed that the location of the constriction is the same as in the FBC mode - approximately in the middle of the nanowire. Contrary to what happens in the FBC mode, when this constriction is formed, the current is further increased in the UVI procedure and thus the local temperature will increase. We observed that once the constriction has formed, it moves towards the cathode side in most cases, but the speeds and paths vary greatly. This indicates that the local temperatures, as well as the grain sizes, orientations, boundaries and thus stress in the nanowire, all play an important role, making the further evolution of the gap formation process specimen-dependent. It is known that grain boundary diffusion depends very much on the type of grain boundary [19]. Higher specimen temperatures during electromigration process in the UVI mode as compared to the FBC mode result in a different evolution of the gap because the ratio between diffusion along the surfaces and the grain boundaries is different. It has been reported that at high temperatures both grain boundary diffusivity coefficient and the surface diffusivity coefficient should be taken into account [20]. Thus in the case of UVI the gap formation can vary significantly from wire to wire due to the differences in grain boundaries and the difference in temperature gradient. Obviously, further research is needed to produce a detailed model of the constriction displacement and the gap formation in relation to the grains and grain boundaries in the nanowires.

Analysis of several HAADF STEM images of samples electromigrated in the FBC mode shows roughly the same height profile as one indicated in Figure 4.7(a). We used FBC only because it reproducibly provides two pointy symmetrical contacts instead of asymmetrical ones forming in the UVI mode. The advantage of having two pointy contacts is that such situation yields less shielding of the back gate and can thus be used for electrical measurements on single molecules. The knowledge of the 3D shape of the electrodes allows a detailed description of the electron tunneling processes across the gap. In this respect it would be useful to perform *in situ* TEM imaging while simultaneously measuring the tunnel conductance. These measurements could then be used to test the validity of the different tunnel models and to obtain an accurate value of the barrier height in these junctions.

## 4.5 SUMMARY

In conclusion, we have performed an *in situ* TEM inspection of electromigration in Pt wires. Our study reveals the different gap formations for feedback-controlled versus noncontrolled electromigration. We have recorded for the first time a video showing the self-breaking process in Pt nanowires and demonstrated that HAADF STEM allows the determination of the 3D profile made by the electrodes via electromigration. Exact knowledge of the geometry of a tunneling junction makes it possible to validate various tunneling models.

## 4.6 REFERENCES

1. Park, H., et al., *Fabrication of metallic electrodes with nanometer separation by electromigration*. Applied Physics Letters, 1999. **75(2)**: p. 301-303.
2. Strachan, D.R., et al., *Clean electromigrated nanogaps imaged by transmission electron microscopy*. Nano Letters, 2006. **6(3)**: p. 441-444.
3. Strachan, D.R., et al., *Controlled fabrication of nanogaps in ambient environment for molecular electronics*. Applied Physics Letters, 2005. **86(4)**.
4. O'Neill, K., E.A. Osorio, and H.S.J. van der Zant, *Self-breaking in planar few-atom Au constrictions for nanometer-spaced electrodes*. Applied Physics Letters, 2007. **90(13)**.
5. Wu, Z.M., et al., *Feedback controlled electromigration in four-terminal nano-junctions*. Applied Physics Letters, 2007. **91(5)**.
6. Houck, A.A., et al., *Kondo effect in electromigrated gold break junctions*. Nano Letters, 2005. **5(9)**: p. 1685-1688.

7. van der Zant, H.S.J., et al., *Molecular three-terminal devices: fabrication and measurements*. Faraday Discussions, 2006. **131**: p. 347-356.
8. Prins, F., et al., *Room-temperature stability of Pt nanogaps formed by self-breaking*. Applied Physics Letters, 2009. **94**(12).
9. Petit, P., et al., *Conductance fluctuations in metallic nanogaps made by electromigration*. Journal of Applied Physics, 2011. **109**(1).
10. Heersche, H.B., et al., *In situ imaging of electromigration-induced nanogap formation by transmission electron microscopy*. Applied Physics Letters, 2007. **91**(7).
11. Strachan, D.R., et al., *Real-time TEM imaging of the formation of crystalline nanoscale gaps*. Physical Review Letters, 2008. **100**(5).
12. Ward, D.R., N.J. Halas, and D. Natelson, *Localized heating in nanoscale Pt constrictions measured using blackbody radiation emission*. Applied Physics Letters, 2008. **93**(21).
13. Taychatanapat, T., et al., *Imaging electromigration during the formation of break junctions*. Nano Letters, 2007. **7**(3): p. 652-656.
14. Esen, G. and M.S. Fuhrer, *Temperature control of electromigration to form gold nanogap junctions*. Applied Physics Letters, 2005. **87**(26).
15. Grose, J.E., et al., *Tunnelling spectra of individual magnetic endofullerene molecules*. Nature Materials, 2008. **7**(11): p. 884-889.
16. Gao, B., et al., *Three-terminal electric transport measurements on gold nanoparticles combined with ex situ TEM inspection*. Nanotechnology, 2009. **20**(41).
17. Gao, B., et al., *In situ transmission electron microscopy imaging of grain growth in a platinum nanobridge induced by electric current annealing*. Nanotechnology, 2011. **22**(20).
18. Ho, P.S. and T. Kwok, *Electromigration in Metals*. Reports on Progress in Physics, 1989. **52**(3): p. 301-348.
19. Smoluchowski, R., *Theory of Grain Boundary Diffusion*. Physical Review, 1952. **87**(3): p. 482-487.
20. Tu, K.N., *Recent advances on electromigration in very-large-scale-integration of interconnects*. Journal of Applied Physics, 2003. **94**(9): p. 5451-5473.



# 5

## CHAPTER 5

### **In situ TEM and STEM studies of reversed electromigration in thin palladium bridges**

*The process of reversed electromigration in Pd nanobridges (15 nm thick, 200 - 500 nm wide and 500 - 1000 nm long) was in situ investigated in two modes – transmission electron microscopy and scanning transmission electron microscopy modes. It was shown that material transfer can be visualized better in the second mode. For the used current densities ( $3- 5 \cdot 10^7 \text{ A/cm}^2$ ) the material transfer in thin Pd nanobridges occurs from the cathode towards anode side therefore Pd has the negative effective charge. Also, the dominant role of the diffusion along grain boundaries was shown.*

## 5.1 INTRODUCTION

Electromigration is a process in which the metallic contact line is thinned down by gradual displacement of atoms during current passage, finally leading to its destruction. The collapse will happen in a place where the thermomechanical stress (the combination of thermal and mechanical stresses) is maximal. The thermal stress occurs due to the Joule heating of the sample during current passage. The mechanical stress arises due to a change in the mass distribution which occurs because of electromigration induced mass transport. The electromigration process requires that atoms overcome the potential crystal lattice barrier which can be described as the electromigration activation energy.

The electromigration force is assumed to be a sum of two terms: the electrostatic (direct) force and the electron-wind force. The wind force corresponds to the momentum transfer from the current carriers (electrons or holes) to atoms in a scattering process. This can be grain-boundary scattering, surface scattering or phonon scattering [1]. The grain-boundary scattering process dominates when the wire width is larger than the average grain size, otherwise the surface scattering prevails. The phonon scattering leads to an increased sample temperature (Joule heating).

Whereas electromigration leads to failure in micro and nanoelectronics, it can also be applied constructively. One of the well-known applications is the creation of nanogaps which can be used to determine the electronic properties of small particles or molecules [2]. Park *et al.* reported a highly reproducible method to fabricate metallic electrodes with nanometer separation by passing a large electrical current through a gold nanowire. Later Prins *et al.* [3] showed that Pt allows to create more stable nanogaps than the Au ones. This is due to the much higher surface mobility of Au resulting in a fast rounding of the electrode tip.

Electromigration can in principle be applied for memory devices. If one can control the current passage through the polycrystalline bridge such that its shape and microstructure is changed in a controlled manner, the electrical properties of a bridge are changed accordingly. This concept is a main principle of memristor technology. The memristor research is mainly focused on the oxide materials because they have a resistance hysteresis [5]. If electromigration can be controlled in the nanobridges also the metals can be applied as memristors. In this work we demonstrate the possibility of a reversed electromigration in Pd bridges and thus reversible resistance changes.

In [4] authors show that Pd micro-strips are stable when the current density

is as much as 80- 90% of the failure current density (8- 10 MA/cm<sup>2</sup>). Since electromigration in Pd is not yet widely studied, the investigation of electromigration phenomena in transmission electron microscope(TEM) by use of the accelerated tests can give more information about this promising material.

In this work we report *in situ* TEM and scanning TEM (STEM) results of electromigration in Pd nanobridges with different geometries. The *in situ* TEM study of electromigration processes in thin polycrystalline Pd bridges allows detailed imaging of the changes due to electromigration. We focussed in particular on the direction of Pd migration in relation to the electrical current direction.

## 5.2 MATERIALS AND METHODS

The electromigration process in palladium (Pd) nanobridges was investigated by *in situ* transmission electron microscopy (TEM) using a FEI Titan microscope operating at 300 keV. The sample holder described in Chapter 2 was used for the experiments. As it was shown in the previous chapters, the combination of the TEM, the holder and the setup for electrical measurements (the "IVVI rack") allows recording of real time movies of the morphology transformations at the nanoscale, as well as I- V curves during passage of electrical current.

Polycrystalline Pd nanobridges with thickness of 15 nm were produced by sputtering of Pd on 100 nm thick free standing silicon nitride membrane. Details of the sample fabrication can be found in Chapter 2 and in [6]. Each bridge is connected to 100 nm thick gold contact.

A scanning electron microscopy (SEM) image of the chip is shown in Figures 5.1(a), (b)). The chip (size 2×2 mm<sup>2</sup>) has 28 gold contacts (the white lines in Figure 5.1(a) which connect the Pd bridges with the electromigration holder. The bridges had different lengths (500–1000 nm) and widths (200–500 nm). Figure 5.1(c) shows a schematic image of bridges with various geometries of contact pads (which are also made of palladium). The total resistance of the structures (including the resistance of bridges, contact pads and leads) before applying an electric current was between 100 and 200 Ohm.

The chip with the Pd nanobridges is fixed onto an Al<sub>2</sub>O<sub>3</sub> chip carrier using conductive tape, and then Au contact pads of several bridges are connected to the chip carrier using the standard wire bonding technique. The experimental chip is placed into a TEM holder for *in situ* electrical measurements, the tip of which is shown in Figure 5.1(d)). For performing the electromigration experiments the holder is connected with electrical control system. The experiments are usually

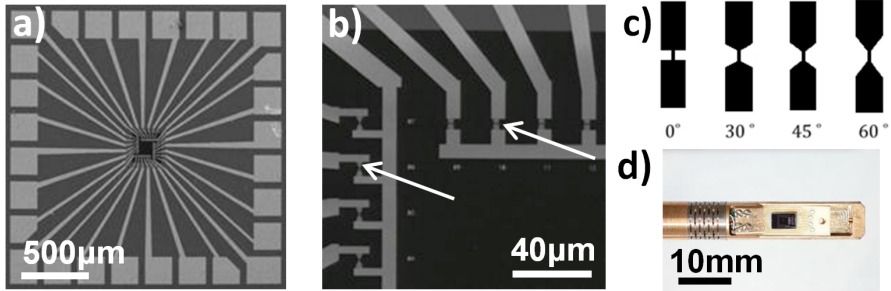


FIGURE 5.1: (a) SEM image of the chip (size  $2 \times 2 \text{ mm}^2$ ) with gold contacts and palladium bridges located in the black area in the middle (free standing membrane); (b) magnified view of one of the membrane corners, so that bridges (indicated with white arrows) and contacts are clearly visible; (c) schematic view of investigated Pd bridges with different geometries of contact pads; (d) the tip of the holder for electrical measurements with the experimental chip inside.

done in a bias ramping mode, which means an uniform increase of the voltage from 0 V to a maximum value 350- 600 mV (this was defined in each separate experiment), decrease back to 0 V, and than increase in the negative range (-350 - (-600) mV) followed by a decrease to 0 V (this call "loop" in the rest of the paper). If the bridge was not broken after one loop, maximum voltage value is increased and next loop is applied till the breakage of the bridge. Throughout the cycles the rate of the voltage ramp is set to 15 mV/s. The holder is cooled with liquid nitrogen, thus all experiments are performed at  $\sim 100 \text{ K}$  at the holder tip to prevent the deposition of carbon contamination on the sample due to electron beam.

We use Camtasia Studio software [7] to record the movies corresponding to the *in situ* measurements directly from the computer screen. The frame rate for the movie is 10- 15 fps.

We employ two different modes for the *in situ* electromigration experiments - TEM mode and STEM mode. Details and results of both experiments are discussed below.

## 5.3 RESULTS

### IN SITU TEM STUDY OF REVERSED ELECTROMIGRATION IN POLYCRYSTALLINE Pd BRIDGES

A few snapshots from a real time TEM movie recorded during the passage of an electrical current through a palladium bridge are shown in Figure 5.2. As-fabricated



Pd bridge has a polycrystalline structure with an average grain size of 5 nm. In Figure 5.2(a) bigger grains are visible in the bridge; those grains were formed during the preceding current annealing (similar to the one discussed in Chapter 3) when the voltage was increased to 400 mV. Images presented in Figure 5.2 correspond to three loops of voltage-current stressing with the maximum voltage values of 450 mV (b)-(c), 470 mV (d)-(e) and 500 mV (f)-(h). At the last loop the nanobridge broke near the cathode side as voltage reached 500 mV. The current density corresponding to the beginning of electromigration is estimated to be  $3 \times 10^7$  A/cm<sup>2</sup>. One of the typical I-V curve of the loop is shown in Figure 5.2(i). Arrows in the images correspond to the direction of electron flow (from cathode side (-) to the anode side (+)). In Figure 5.2 we demonstrate the reversed electromigration in the 200 nm wide and 1000 nm long bridge, but similar behaviour was observed for bridges with different geometries on which electromigration experiments were carried out.

During electromigration voids are formed near the cathode side (leading to the resistance increase); those voids are refilled when we reverse the polarity resulting in decrease of the resistance. This voids formation and refilling process cannot be repeated endlessly because the sample areas where material is removed are gradually getting thinner. Thus, at some critical voltage value the process results in a failure of the wire at the cathode side (Figure 5.2(h)).

TEM imaging gives a good overview of the process of grain growth. However, if one wants to analyse the mass transport along the bridge due to electromigration process) or any other dynamical processes in details, standard TEM imaging is insufficient. In standard TEM imaging a diffraction contrast cannot be distinguished from mass - thickness contrast: change in a grey level in TEM image can be explained not only by a thickness change, but also by the changes in the grain orientation. As a result, the direction of mass transport during electromigration cannot be determined easily.

### **IN SITU STEM STUDY OF REVERSED ELECTROMIGRATION IN POLYCRYSTALLINE Pd BRIDGES**

To analyze the direction of material flow, a few STEM movies were recorded. Figure 5.3 shows a series of images from the STEM movie, taken during voltage stressing of the Pd bridge. Similar to Figure 5.2, images correspond to three loops of voltage increase: (a) - the initial view of the bridge, (b)-(c) - the first loop, (d)-(f) - the second loop, (g)-(h) - the first part of the third loop till the bridge break) in the bias ramping regime. The maximum voltages were set to 500 mV (b)-(c), 520 mV (d)-(f)

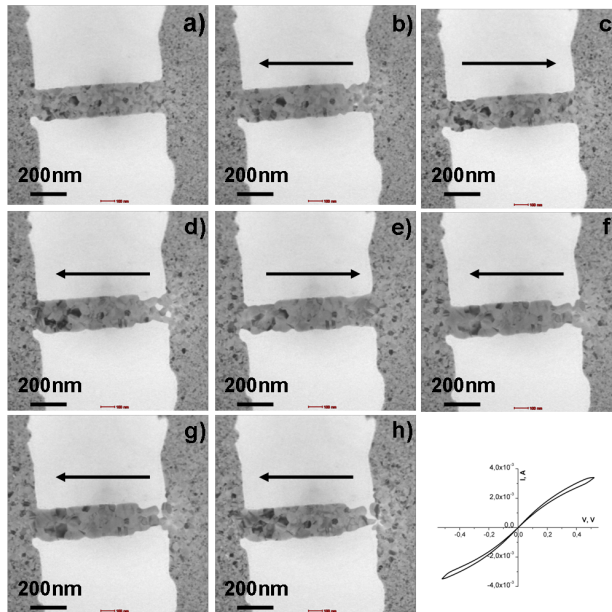


FIGURE 5.2: Snapshots from the TEM movie showing the process of reversed electromigration. (a) a TEM image of the initial configuration of the bridge; (b) a TEM image of the Pd bridge after some preliminary grain growth. During electromigration voids are formed on the cathode side (c), (e), (g)-(h) and then they refilled (d), (f) due to the changing of current direction. Black arrows indicate the direction of electrons; (i) typical I-V curve for one loop in the bias ramping mode.

and 540 mV (g)-(h) correspondingly. A small camera length was selected to acquire STEM images allowing to minimize diffraction contrast and to enhance the mass - thickness contrast. The frame rate of the STEM movie is selected to be 3 frames/sec to get acceptable image quality for the selected camera length. As can be seen from Figure 5.3(a)-(b), increasing of the voltage to 500 mV leads to the formation of voids (black areas) at the cathode side, and to a sample thickening and hillocks formation (brighter areas) at the anode side. Changing of the current direction results in refilling of the voids and even in growing of hillocks on the ex-cathode side (which is the anode side now).

To sum up, repeating of the voltage loops leads to reverse material transport from cathode towards anode side. We did experiments on bridges with different geometries, and always the process of reversed electromigration was observed. The

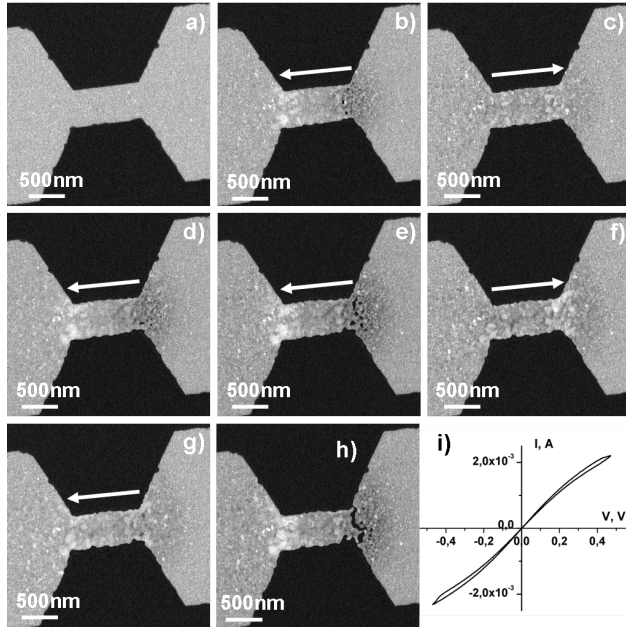


FIGURE 5.3: Snapshots from the STEM movie showing the direction of material transfer. (a) The initial state of the bridge. During electromigration voids are formed on cathode side, and material accumulation is occurred on the anode size (b), (d)-(e), (g)-(h), and then holes are refilled (c), (f) due to the change of polarity. White arrows indicate the direction of the flow of electrons; (i) typical I-V curve for one loop in the bias mode.

length of the shown bridge is 1000 nm, the width is 500 nm.

To analyze the material transfer in time, data processing was done using ImageJ software [8]. In Figure 5.4(a) the contrast change along the bridge axis (which corresponds to the changes in thickness) in time is shown. The figure is matched to a compressed representation of the whole movie (the total duration of movie is 100 seconds) recorded for one voltage loop (with maximum voltage of 520 mV) for the sample presented in Figure 5.3. Every horizontal line in Figure 5.4(a) corresponds to the signal from a real STEM snapshot after applying of the Gaussian blur with a radius of 20 pixels to each frame of the movie. Lines are collected along the dashed line shown in Figure 5.4(b). The Gaussian blur is implemented to reduce the effect of diffraction contrast such as the contrast really represents the thickness of the integrated material transfer along the bridge axis. The vertical black lines in Figure

5.4(a) indicate the positions where the intensity profiles were taken (shown in Figure 5.4(e)). Lines C and E correspond to the sides of the Pd bridge (to make it clear, the distance between them is 1000 nm which is equal to the bridge length). Upper part in Figure 5.4(a) corresponds to the initial state of the bridge prior to electromigration and shows uniformity of the bridge thickness (in Figure 5.4(b) one of the first STEM snapshots from this area is presented). The middle part in Figure 5.4(a) is referred to the electromigrated state of the bridge with mass transferred from cathode (right side) to the anode (left side) (in Figure 5.4(c)) corresponding image is shown). In Figure 5.4(e) lines C and E have a big plateaus in the middle parts which shows the maximum and the minimum intensity level and, as a result, the regions of the material storage and depletion correspondingly. The bottom area in the Figure 5.4(a) corresponds to the reversed direction of current flow. Here transport of the material toward right (anode) side is observed with complete refilling of the voids and even a small hillock formation (see Figure 5.4(d)).

If the direct force acts in the same direction as the electron wind force, the migration of Pd matches with the electrons flow - from cathode to anode side- and thus the effective charge of Pd atoms is negative. In the case when the direct force acts opposite to the electron wind force, two situation should be considered: the direct force is less than the electron wind force - Pd atoms move in the direction of electrons flow and effective charge is negative or the direct force is a dominant component, than Pd atoms move against the electrons flow and effective charge is positive.

From the results discussed above it is clear that Pd is transferred from negative to the positive side (in the same direction as electron flow), from which we conclude that Pd has a negative effective charge. The process of holes and hillocks formation and refilling starts quite fast (in a couple of seconds), which can be judged from a sharp transition areas between upper and middle parts and between middle and bottom parts in Figure 5.4(a), also from the sharp edges of plateaus for lines C and E in Figure 5.4(e). These fast transitions point to the existence of a threshold value for beginning of electromigration. When this threshold value (the current density of about  $3.5 \times 10^7 \text{ A/cm}^2$ ) is overcome the electromigration starts to be a rapidly evolving process. Yang *et al.* [4] report that Pd micro-stripes are stable when the current density is as much as 80–90% of the failure current density ( $0.8\text{--}1 \times 10^{-7} \text{ A/cm}^2$ ), which is in a good agreement with our results.

Lines A and G in Figure 5.4(a) and Figure 5.4(e) indicate places which are not affected by electromigration, because the temperature is lower over there (as we

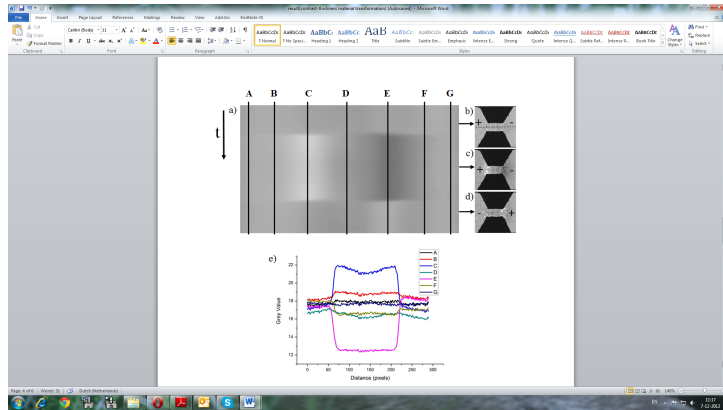


FIGURE 5.4: (a) thickness changing along the bridge axis versus time, vertical black lines are indicate where the intensity profiles (e) were taken; (b)-(d) Snapshots from the STEM movie taken during electromigration in time indicated with arrows; (e) grey value change along the lines indicated in (a).

consider the contact pads to be the heat sinks). Lines B and F represent places in a contact pads where the material transport is quite small. The mass transfer is occurred within a Pd bridge and a close proximity to it (between B–F lines in Figure 5.4(a), the radius of involved area on contact pads is around 500 nm. It should be pointed out, that the thickness in the middle part of the nanobridge during electromigration remains almost the same (area near the line D in Figure 5.4(a). This means that the middle part of the bridge behaves almost like a perfect channel for atoms without material storage or depletion. In Figure 5.4(e) small diminishing of grey value can be seen for the line D which corresponds to a thinning of the sample during electromigration. In Figure 5.4(e) the grey value distribution between lines A - G is smaller at the beginning (between 0 - 20 s) than at the end of electromigration process (between 80 - 100 s), because at the end of the voltage loop morphology of the bridge was significantly changed (material was stored near the cathode side, the middle part of the bridge became thinner, the bigger grains were grown) which can be clearly seen in Figure 5.4(d).

### COMPARISON OF THICKNESS MEASUREMENTS MADE BY STEM AND AFM

In order to confirm the direct correlation between the image intensity on the STEM image and real thickness of the bridge we have analyzed the electromigrated

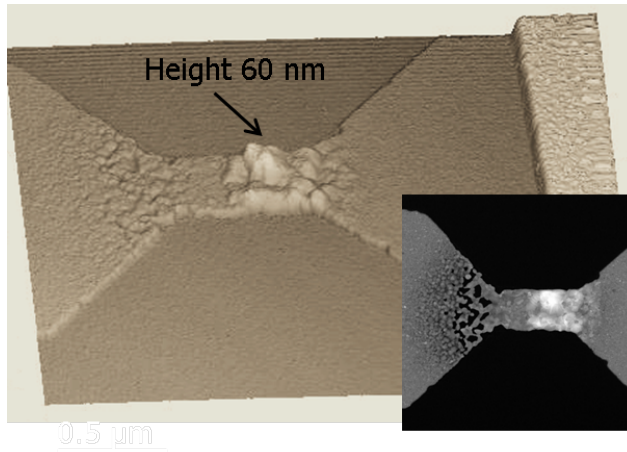


FIGURE 5.5: 3D AFM picture of the bridge showing the profile of material distribution after electromigration process in Pd bridge. Voids are formed at the cathode side (on the left) while hillocks are observed on the anode (right) side of the bridge.

bridge with an AFM. Both AFM and STEM images were obtained after a few voltage loops. As can be seen in Figure 5.5, the brightest area on STEM image corresponds well to the area with largest thickness, whereas area with voids corresponds to the region with the lowest intensity on the STEM image.

### INFLUENCE OF THE CAMERA LENGTH ON THE EXPERIMENTAL RESULTS

Figure 5.6 represents STEM images obtained for two camera lengths: 29 mm (Figure 5.6(a)) and 363 mm (Figure 5.6(b)) for tilt angle of  $0^\circ$ . In bright field TEM imaging (Figure 5.2) two types of contrast are competing: mass-thickness contrast and diffraction contrast. As was already mentioned, diffraction contrast in a TEM imaging arises due to difference in orientation of the grains in polycrystalline material and complicates the analysis of the real thickness of such sample. However even STEM image obtained at camera length of 363 mm (Figure 5.6(b)) does not only reflect the thickness variation on the sample but also the strong contrast from the grains in zone (appeared white). In that case the more the crystal is aligned along low index zone axis (for example 111 for Pd), the brighter it will appear in the STEM image. Images acquired with the shorter camera length (Figure 5.6(a)) demonstrate much more uniform contrast on the contact pads. Thus the wide white area visible on the left side of the bridge can be interpreted as thicker area. Comparison of

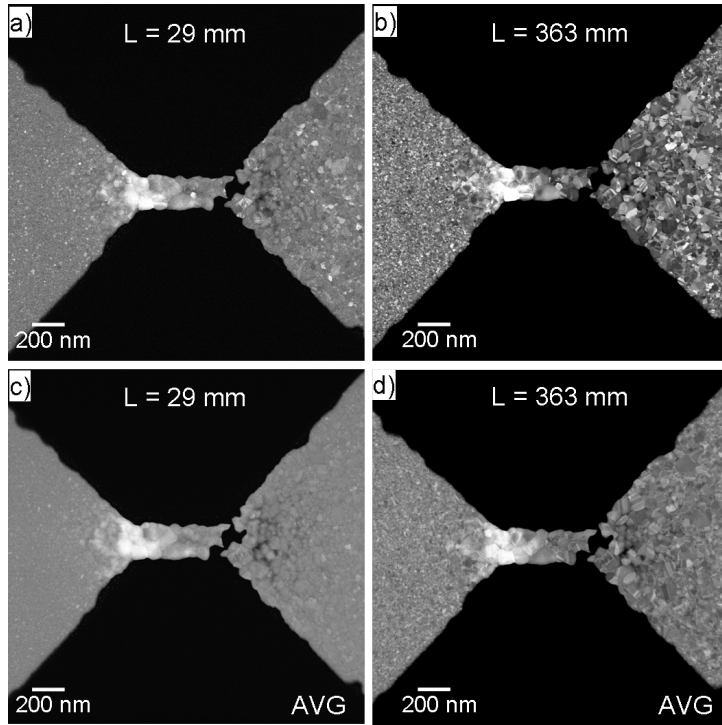


FIGURE 5.6: (a)–(b) STEM images obtained for camera lengths of 29 mm and 363 mm correspondingly. Tilt angle is 0. (c)–(d) Averaged STEM images over the tilt series from  $-5^\circ$  to  $5^\circ$  with step of  $1^\circ$  for the same camera lengths.

Figures 6(a) and 6(b) reveals that careful selection of the camera length is vital and in the case of the bigger camera length all grains in a polycrystalline samples are clearly observed complicating the analysis of the height profiles.

To further minimize the effect of the diffraction contrast in STEM imaging we obtained tilt series for the same camera lengths. Since our holder is a single tilt holder only  $\alpha$  tilt from  $-5^\circ$  to  $5^\circ$  with step of  $1^\circ$  was used. We combined and averaged the obtained images for each of the camera lengths using the ImageJ software. The results of this averaging are presented in Figures 5.6 (c)–(d). For the short camera length (29 mm) the average contrast became uniform and particular grains are difficult to identify. At these conditions the intensity of the obtained signal can be interpreted as measure of the samples height. For the long camera

Microscope camera length, mm	HAADF shadow radius, mrad
38	153.0
60	99.2
160	37.9
378	16.0
478	12.4

TABLE 5.1: Camera length calibration for FEI Titan microscope operated at 300kV. Calibration was done for objective lens value of 89.5061% by Robert Pennington [9].

length the quality of averaged image is similar to one of the single image obtained at  $L = 29$  mm thus not yet perfect.

We noticed, however, that the use of the smallest camera length significantly degrades the quality of the images hence less number of electrons fall on the HAADF detector. Thus smaller camera lengths require longer exposure time to record each frame. For example for the *in situ* TEM movies we use a frame rate of about 10-15 frames/sec, whereas for qualitative STEM frame rate of at least 3 frame/sec is required.

In Table 5.1 typical calibrated values for radius of HAADF detector are presented. As can be seen for the smallest camera length inner radius of the detector has the biggest value and number of diffraction rings influencing on contrast of the STEM image is significantly decreased. For bigger camera length ( $\sim 370$  mm in our case) inner radius of the HAADF detector is just 20 mrad thus many grains becomes clearly visible in the STEM image obtained at this conditions. The part of the diffraction pattern covered by the inner ring of the detector is marked in Figure 5.7 with green disk for the camera length of 370 mm and with orange disk for the camera length of 160 mm.

Electrical current passing through the metal bridge can lead to thermal and mechanical stresses [10]. The bridge will break at the position of the highest total stress - the sum of thermal and mechanical stresses. By using of alternating current (AC) we can largely exclude the electromigration effect (and as a result the asymmetric mechanical stress), thus only the thermal stress remains sufficient. We applied AC with different frequencies (2 - 100 Hz) to several bridges; the typical view of the bridge after the breakage is presented in Figure 5.8(a). In all cases bridges were broken in the middle, so the thermal stress has a maximum in this area. Due to the



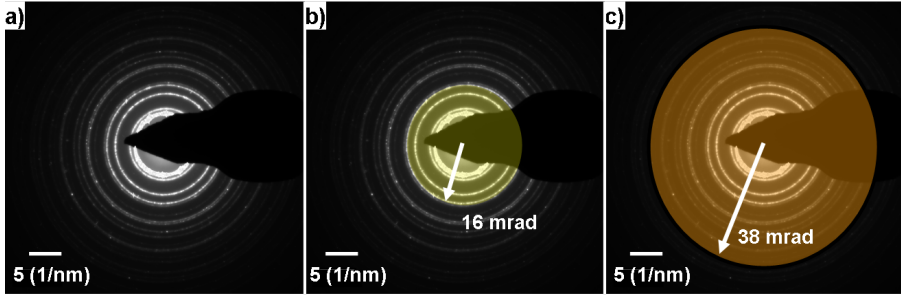


FIGURE 5.7: (a) Diffraction pattern obtained for the sample in Figure 5.6; (b) The green disk indicates the inner angle of the ADF detector of 16 mrad, corresponding to camera length of 378 mm; (c) The disk indicates the inner angle of the ADF detector of 38 mrad, corresponding to camera length of 160 mm.

Joule heating the temperature profile along the bridge has a maximum at the center of the bridge and the temperature decreases towards the contact pads (which we consider as a heat sinks).

In the case of the DC experiments the mechanical stress is zero in the middle part of the bridge and it increases towards the contact pads. This occurs due to the build up of the compressive stress near the anode side (piling up of material). At the same time the tensile stress is built up at the cathode side due to removal of material from that part. At the center of the bridge no significant changes are observed (in Figures 5.3, 5.4 the middle part of the bridges has almost the same grey level), thus we conclude that the value of thermal stress is not enough to increase the mobility of atoms in this area. On the other hand, the stress near the contact pads is large enough to induce deformation, finally leading to breakage of a Pd bridge near the cathode side.

In Figure 5.8(b) a STEM image of one of the contact pads during electromigration is presented. The grain boundaries are clearly visible and they appear darker than grains themselves. Analysis of the movie shows that the grain boundaries act as the channels for material transport and that the grain boundary diffusion is the dominant component in the electromigration process. In the bridge area (Figure 5.8(b) left part) the edges of the grains are not visible, so we conclude that not only the grain boundary diffusion but also the surface diffusion is involved. From literature [11] it is known that at 100°C the dominant mechanisms for atoms migration (in Cu, Al) are both surface and grain boundary diffusion, whereas lattice diffusion is negligibly small. This statement is in agreement with our results.

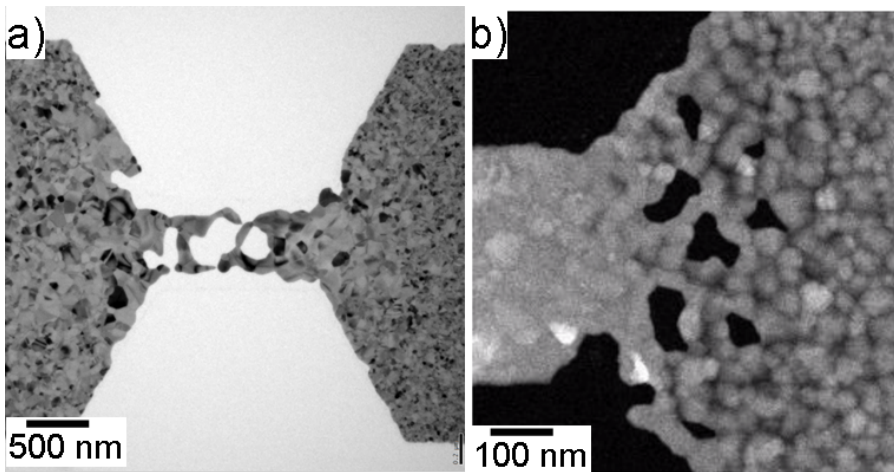


FIGURE 5.8: (a) TEM image of the broken bridge after application of alternating current; (b) STEM image of the contact pad near the cathode side.

Previously described Pd bridges were deposited on 100 nm thick  $\text{Si}_3\text{N}_4$  membrane. To realise the influence of heat dissipation on electromigration process, the membrane of several chips was thinned down to 40- 50 nm using reactive ion etching ( $\text{CHF}_3 + \text{Ar}$ ). In our experiments we did not find any significant differences in the flow of electromigration process for the samples with different thickness of silicon nitride membrane (in a region 40- 100 nm).

## 5.4 SUMMARY AND CONCLUSIONS

*In situ* TEM study of the electromigration process in thin polycrystalline Pd bridges reveals the obvious formation of the voids at the cathode side. However absence of the information about the thickness distribution in the whole bridge after electromigration process as well as presence of the diffraction contrast from the grains complicates judgment to the direction of material flow. The direction is defined by the sign of the effective charge in the material (see Chapter 1) and no data was reported in literature for the Pd films. Investigation of the sample by use of STEM technique shows that the migration of the atoms occurs via the bridge from cathode to anode side. Thus it was experimentally proven that Pd has negative effective charge. On the other hand, *in situ* STEM experiments allow to

visualize the process of reversed electromigration: during a current passage holes are formed near the cathode side, and then they are refilled after changing of the bias polarity. We demonstrated that in the case of Pd bridges the grain boundary diffusion dominates over lattice and surface diffusion.

The effect of camera length selection on image quality was analyzed in details. We compared images obtained for short (29 mm) and long (~370 mm) camera lengths. Shorter camera length is better if one wants to check the thickness variation over the sample. However longer camera length allows to obtain better image quality for the shorter scanning time and is advantageous for recording of *in situ* STEM movies. Also the correlation between the intensity in the STEM image and real thickness distribution was carried out by comparison with results obtained in atomic force microscope.

## 5.5 REFERENCES

1. Ho, P.S. and T. Kwok, *Electromigration in Metals*. Reports on Progress in Physics, 1989. **52(3)**: p. 301-348.
2. Park, H., et al., *Fabrication of metallic electrodes with nanometer separation by electromigration*. Applied Physics Letters, 1999. **75(2)**: p. 301-303.
3. Prins, F., et al., *Room-temperature stability of Pt nanogaps formed by self-breaking*. Applied Physics Letters, 2009. **94(12)**.
4. Yang, Y., et al., *Current sustainability and electromigration of Pd, Sc and Y thin-films as potential interconnects*. Nano-Micro Letters, 2010. **2(3)**: p. 184-189.
5. Kwon, D.H., et al., *Atomic structure of conducting nanofilaments in TiO<sub>2</sub> resistive switching memory*. Nature Nanotechnology, 2010. **5(2)**: p. 148-153.
6. Gao, B., et al., *In situ transmission electron microscopy imaging of grain growth in a platinum nanobridge induced by electric current annealing*. Nanotechnology, 2011. **22(20)**.
7. Camtasia studio. Available from: <http://www.techsmith.com/index.html>.
8. ImageJ. Available from: <http://imagejdocu.tudor.lu/>.
9. Pennington, R. 2009; Available from: <http://www.microscopy.cen.dtu.dk/microscopes/titan/atemspecs.html>.
10. Durkan, C., *Current at nanoscale. An introduction to Nanoelectronics.*, ed. I.C. Press 2007.
11. Tu, K.N., *Recent advances on electromigration in very-large-scale-integration of interconnects*. Journal of Applied Physics, 2003. **94(9)**: p. 5451-5473.

12. Gao, P., et al., *In situ TEM studies of oxygen vacancy migration for electrically induced resistance change effect in cerium oxides*. *Micron*, 2010. **41(4)**: p. 301-305.

# 6

## CHAPTER 6

### **In situ modification of TEM samples with Helium Ion Microscope**

*Novel sample modification methods using a helium ion microscope (HIM) are presented in this chapter. In particular we report a new method of preparation of thin SrTiO<sub>3</sub> and Si samples without significant artefacts by in situ heating of the samples during helium beam illumination. The possibility to reshape thin metal lines on an electron transparent membrane is discussed. The obtained structures were tested using transmission electron microscope and their applicability for in situ electrical measurements was investigated.*

---

The work presented in this Chapter has been partly published as Rudneva, M., van Veldhoven, E., Malladi, S., Maas, D. and Zandbergen, H. W., *Application of the Helium Ion Microscope as a Sculpting Tool for Nanosamples*, MRS Proceedings, **Volume 1455**, 2012

## 6.1 INTRODUCTION

Direct momentum transfer from charged particles to atoms of the sample is one of the main physical mechanisms for ion beam damage and for expelling atoms from their lattice positions [1]. If one wants to remove material from the surface of a sample - for instance to create a hole - one can use a range of charged particles such as ions or electrons. Although ions are preferable due to their mass, implantation of the ions into the sample may cause significant lattice damage in the illuminated area as well as its surroundings and can result in surface degradation of the remaining structure [2]. To analyse the influence of the ion beam on the illuminated sample, three forms of damage should be considered: a) surface sputtering of atoms, b) displacement of atoms in the sample from their original lattice positions and c) implantation of the incident ions into the sample [1]. TRIM calculations show that in the case of relatively heavy ions such as gallium, 90% of energy is dissipated through the ion's interaction with nuclei. For 25-keV helium ions, 6.7% of this energy is dissipated through the ion's interaction with nuclei whereas 93.3% of the energy is transferred to electrons. Light ions, such as helium, have a lower energy loss rate, and therefore they penetrate much deeper into the specimen than heavy gallium ions. The average energy loss rate for 25-keV helium ions in silicon is 89 eV/nm [3]. Helium ions, losing energy primarily through electron interactions, cause much less lattice damage in the sub-surface layer than gallium ion beams and can be used for precise nanolithography modification of the samples or ion beam-induced surface chemistry [4], [5].

The Helium ion microscope (HIM) was introduced in 2006 as a new high-resolution imaging tool [6]. The unique helium ion source can be regarded as the nearly ideal point source, because it results in a subnanometer probe size and generates a large depth of view. Compared to other ions, helium ions have a particular sample interaction that generates a relatively high number of low-energy secondary electrons and a low yield of backscatter ions, which allows the remarkable imaging of a range of samples, including samples with high local specimen charging [4],[7, 8].

Being used for nanofabrication, the helium ion microscope is reported to yield 4-nm-wide lines with a pitch of 10 nm as lithography tool [9, 10]. Very narrow structures with almost no overspray can be made with the gas-induced deposition [11, 12]. For thin-film dicing and nano-pore drilling, sub-10-nanometer features are now achieved [13, 14].

It is known that penetration of the accelerated helium ions into bulk samples, for

example in silicon, leads to amorphization, the formation of nanobubbles and even microbubbles at high doses [1]. In this chapter the possibility to perform defect free cutting of Si and SrTiO<sub>3</sub> lamellas of various thicknesses at elevated temperatures is presented. Also results of precise modification of thin Pt bridges with a helium beam and of subsequent electrical measurements on them are reported.

## 6.2 MODIFICATION OF SI LAMELLAS

Silicon is one of the most commonly used materials in the semiconductor industry. Ongoing development and miniaturization of semiconducting devices requires new techniques for sample modification and reparation in case of any possible failure or damage (Figure 6.1). A few advanced techniques were developed to improve the quality of manufacturing of semiconductor devices and to have the tool for study and repair of possible damages in them. For example, the focused ion beam (FIB) preparation method gives higher sample quality in shorter preparation times than traditional techniques, such as ultramicrotomy and polishing. FIB microscopy using gallium ions has demonstrated good results for bulk samples so far. However, the lack of resolution, significant broadening of the beam near the surface and contamination of the sample with gallium ions make Ga-FIB nanomodification of the samples nearly impossible [15].

For example, if FIB method is used for modification of the silicone samples some undesirable defects are formed due to the fact that heavy gallium ions penetrate into the sample, creating surface damage in the samples. In that sense it is necessary to develop new cutting techniques that allow the sample to be modified on the scale of a few nanometers without causing significant damage or contamination.

Using a focused helium ion beam, available in HIM cutting with a spot size of about 1 nm can be performed allowing to get higher precision than FIB machines. However, studies of influence of helium bombardment and subsequent annealing of the silicon samples demonstrate the possibility of formation of extended defects [16]. It was shown that interaction between point defects and helium atoms may lead to generation of helium bubbles. Thermal annealing results in their subsequent evolution into voids due to increase of the helium out diffusion [17]. The main features of the implantation process of helium ions into the silicon substrate were studied extensively. The focus was mainly on obtaining stable and reproducible voids in silicon for defect engineering applications [18]. Nevertheless, cutting of the silicon samples with helium beam was not yet described in detail and a clear understanding of this process has not yet been obtained.

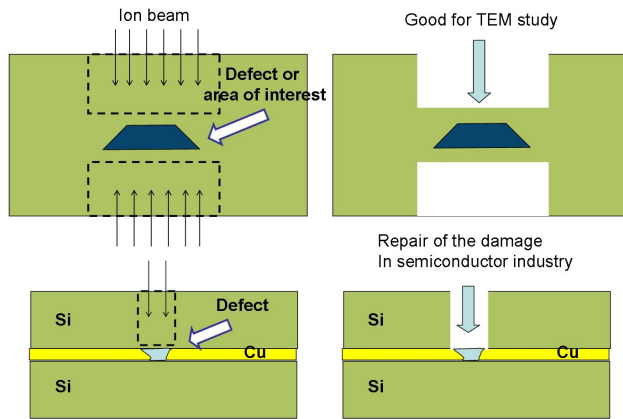


FIGURE 6.1: Examples of sample modification in the case of presence of defect in the sample. (a) Material is selectively removed around defect/area of interest with helium ion beam. In this way thin lamella appropriate for TEM study can be made; (b) Silicon is removed above the defect/fault in embedded Cu line. This method allows, in principle, to repair local damage in the conducting lines without affecting surrounding area.

If one wants to use the high accuracy of the HIM one has to completely prevent the deterioration of the silicon. In this part we demonstrate possibility of achieving defect free cut in silicon by performing modification of the sample at elevated temperature.

### 6.2.1 METHODS

A few silicon lamellas of  $6 \times 10 \mu\text{m}^2$  with different thicknesses ( $\sim 100\text{-}300 \text{ nm}$ ) were prepared by Ga-FIB milling. Recent developments in the field of FIB microscopes allows, in principle, to obtain very fine holes in the bulk sample. However the Ga-FIB milling process leads to destruction of the crystallinity of the surface layer of the sample (or even of the whole sample) as well as to contamination of the sample with gallium ions. This is clearly undesired and thus a last nanoscale modification/surface cleaning step should be performed by, for example, a helium ion microscope.

We use an ORION plus Zeiss helium ion microscope, operated at 25 kV and equipped with a Raith Elphy multibeam pattern generator. The beam currents between 2 pA and 3 pA were used for the cutting, the current intensity was controlled



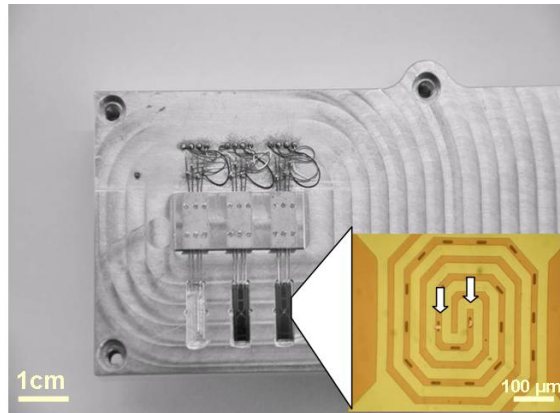


FIGURE 6.2: Optical image of the heating stage with two heaters. Inset: heater with two Si lamellas located above the holes in the SiN membrane.

with the helium gas supply. The pattern generator was used to control the beam path, number of scans and shape of the cut, which could be set to any arbitrary form. Images of the sample before, during and after cutting were recorded by an Everhart-Thornley (ET) detector. The helium dose is estimated by taking into account the beam current, size of the illumination area and number of scans and in order of  $10^{15}$  ions/cm<sup>2</sup>.

The FIB prepared silicon lamellas were placed over the holes in the membrane of the MEMS-based heaters (Figure 6.2(b)) using a micromanipulator.

We developed a special holder which allows *in situ* heating of the samples up to 800°C in the HIM (Figure 6.2(a)). Up to three MEMS based heaters can be loaded simultaneously into the HIM and connected with electronics of the holder via special needle-like clamps. Because the HIM does not have electrical inserts, we made a battery-based heating device with an electrical circuit. The temperature of each heater is set using a calibrated resistor. A special switch which is activated by the high current helium ion beam (~150 pA) is used to turn on and off each MEMS heater without removing the stage from the microscope. It is possible to judge by direct observation whether the heater is on (see Figure 6.3). Nanoscale analysis of the HIM-modified samples was done with a FEI Titan transmission electron microscope operated at 300 kV. Images were acquired with a Gatan CCD camera.



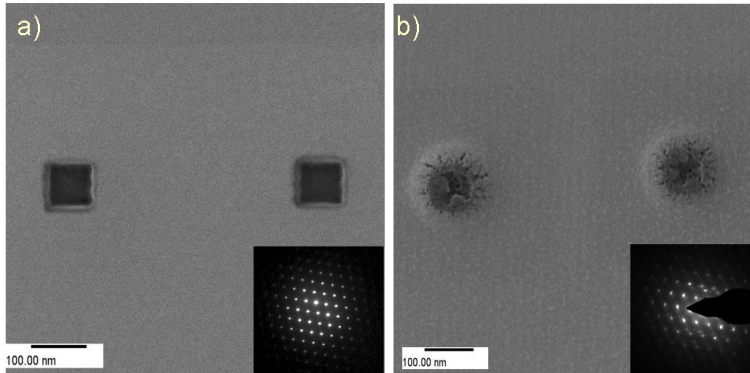


FIGURE 6.4: Result of cutting silicon lamellas with a thickness of (a) 100 nm and (b) 300 nm at room temperature. Boxes measuring  $100 \times 100 \text{ nm}^2$  were scanned with a helium beam at the same dose. Diffraction patterns in the insets indicate that the crystallinity of the area around the cut was substantially affected in the case of the 300-nm-thick sample.

bution in silicon (see discussion). Making the same modification at  $700^\circ\text{C}$  results in a clean cut without visible damage (Figure 6.5, top box) thus these temperature conditions can, in principle, be used for precise sample modification.

Local thinning down of selected area was performed at  $650^\circ\text{C}$  for the 300 nm thick silicon lamella. After modification by helium beam, the sample was studied in TEM, yielding a high resolution images as well as electron diffraction patterns. Initially, the 300 nm thick sample is not suitable for high resolution TEM inspection; however after helium beam milling it is possible to get very sharp images of the illuminated area (Figure 6.6(a), 6.6(b)). Diffraction patterns show that the sample was not amorphized during Helium milling and moreover crystallinity of this area remains unaffected.

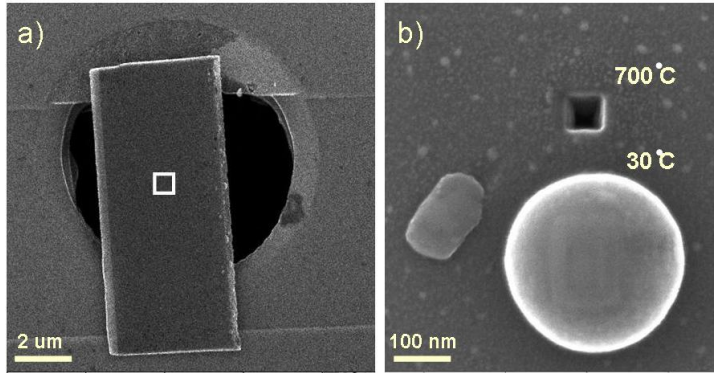


FIGURE 6.5: (a) Silicon lamella placed above the hole in MEMS heater; (b) Results of cutting of silicon lamella at room temperature and at 700°C. As can be seen, at room temperature a large white halo appeared around the illuminated area, whereas at 700 °C it was possible to create a through hole in the lamella.

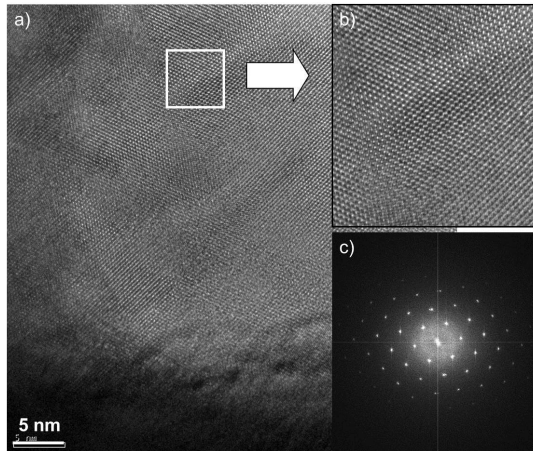


FIGURE 6.6: High resolution image of helium modified silicon sample obtained in transmission electron microscope. (a) Image of the thinning out created in silicon lamella; (b) Blow-up from the area marked with white frame in (a). Silicon atoms are clearly visible pointing that this area is very thin; (c) Fast Fourier Transform (FFT) image from the selected in (b) area.

### 6.2.3 DISCUSSION

Helium ion microscope works as a good cutting tool if it is possible to remove silicon atoms from the surface without any additional effects to the sample. In other words helium implantation leading to defect formation or sub-surface lattice changes should not occur. However, due to moderate interaction of high energy helium ions with matter they can penetrate relatively deep into the sample. Figure 6.7 represents TRIM simulation of the stopping range of helium ions at 25 keV in silicon at room temperature. Experimental data (Figure 6.4(a)) shows that for thin samples ( $\sim 100$  nm) no damage is observed after helium beam milling. At these thicknesses the ratio of the ions, stopping in the sample is relatively low and interaction volume in the beam with sample is small due to the high collimation of the beam. For the thicker lamellas most of the helium ions are stopped and retained inside the sample. Distribution of helium ions in thick silicon sample is shown in Figure 6.7(a). At room temperature the diffusion rate of helium to the surface is lower than the implantation rate. In other words, amount of the ions caught in the sample grows. This leads to accumulation of the ions in the sample, to a destruction of the silicon lattice and finally to amorphization. Moreover, due to the build-up of mechanical stress a large helium bubble emerges on the surface (Figure 6.5(b)). At elevated temperature the kinetic balance shifts towards loss of helium due to faster diffusion. It is important to note that the diffusion speed of helium is very material-dependant, so the optimal temperature for the HIM cutting depends on the substrate material. In a summary, we determined damage created in silicon by a focused helium ions at various temperatures in the range from room temperature to  $700^\circ\text{C}$ . A large amorphous area and, at higher doses, helium bubbles are created at room temperature. At  $700^\circ\text{C}$  silicon is almost clean of any amorphous areas or other defects. At intermediate temperatures dislocations are formed by the helium ion beam but the damage is far less than that at room temperature. This effect is explained by an outward diffusion of helium, which at  $700^\circ\text{C}$  is fast enough to prevent helium accumulation and defect formation. It is argued that the clean cutting at a temperature of  $700^\circ\text{C}$  allows making holes with defect-free crystalline edges in silicon. This is important for the semiconductor industry for failure analysis as well as failure repair.

## 6.3 NANOSCALE MODIFICATION OF $\text{SrTiO}_3$

Oxides with a perovskite structure have a large variety of properties and, because of similarities in unit cells, they are often being stacked or used as thin films on

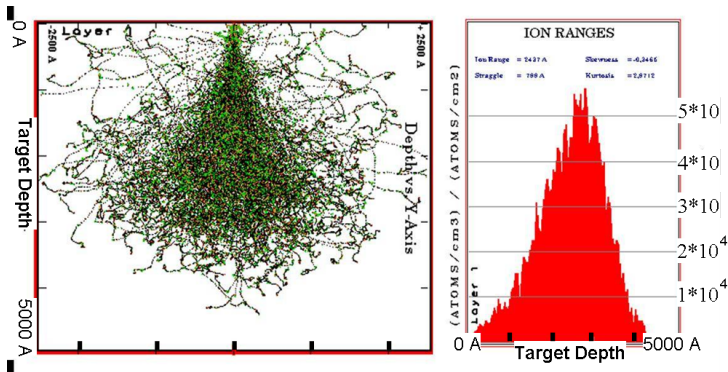


FIGURE 6.7: TRIM simulation of penetration depth for 30 keV helium ions in silicon. (a) Distribution of penetrated helium ions in the sample. (b) Calculated ion ranges for the silicon.

other oxide substrates with a perovskite structure [21]. One of the frequently used perovskite substrates is  $\text{SrTiO}_3$ . This is a dielectric with a simple cubic unit cell; however, a deviation in stoichiometry and in geometry may induce additional electrical properties such as conductivity [22] and ferroelectricity [23]. In the TEM characterization of thin films on  $\text{SrTiO}_3$  substrates, we are particularly interested in the film  $\text{SrTiO}_3$  interface to determine intermixing and interface roughness. Conventional TEM sample preparation techniques, such as cross section low-angle broad beam ion milling and focused gallium ion beam milling, can provide such information. However if one would like to thin down some local areas to obtain more detailed information, additional thinning is almost never successful.

With the HIM, it might be possible to remove material over the defect or to create a wedge-shaped sample. The well-defined wedge shape allows the very precise investigation of the changes in the image as a function of thickness. This provides details of atom positions with various scattering potentials such as O next to Sr and Ti. Although the HIM allows the selected removal with high precision, the quality of this cut still remains an open question.

A few  $\text{SrTiO}_3$  lamellas of various thicknesses were prepared by FIB milling. Further thinning down of the sample as well as creation of the holes and wedge-shaped cuts were accomplished by focused helium ion beam. Experiments were performed for different ion doses between  $1 \times 10^{14}$  ions/cm<sup>2</sup> and  $5 \times 10^{15}$  ions/cm<sup>2</sup>.

Cutting experiments on a 100-nm-thick sample show the formation of nanobubbles around the hole (Figure 6.8) at room temperature. Moreover significant



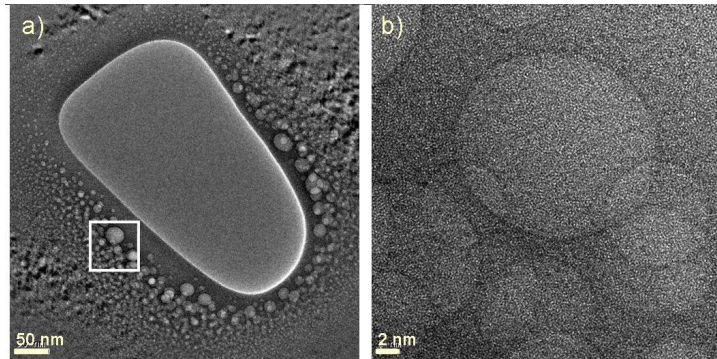


FIGURE 6.8: Result of cutting a SrTiO<sub>3</sub> lamella at room temperature. (a) Overview of the illuminated area. (b) Nanobubbles formed around the hole

degradation and even amorphization of the area close to the cut is observed by TEM inspection of the sample. For a thicker sample, bigger bubbles are present around the formed hole and the crystallinity is completely lost in the area (Figure 6.8(a)). The heating stage, described earlier, was used for carrying out the experiments at elevated temperatures. For this purpose we used a 150-nm-thick SrTiO<sub>3</sub> lamella on MEMS heater. The heater temperature was set to 650°C. As can be seen from Figure 6.9(a), the hole made at 650°C has a completely different appearance than the hole made at room temperature. It is obvious that at room temperature, the area around the cut is strongly affected (Figure 6.9), whereas at 650°C, it is possible to obtain a clean cut without any visible damage. The sample was checked in the TEM (Figure 6.9(b)). Inspection shows that the crystalline structure of SrTiO<sub>3</sub> remains unaffected and no bubbles/surface deformations were created compared to the result shown in Figure 6.8.

### 6.3.1 DISCUSSION

Ongoing developments in transmission electron microscopy require new possibilities for sample investigation and at the same time require new and more accurate sample preparation techniques. The HIM could be a great tool for the preparation of samples for TEM, if it has a sufficient throughput and creates no or very limited damage to the fabricated electron transparent specimens. The helium ion impact on all kinds of materials is not yet known. Thus its usefulness for the TEM sample preparation, in particular for composites, still has to be determined.

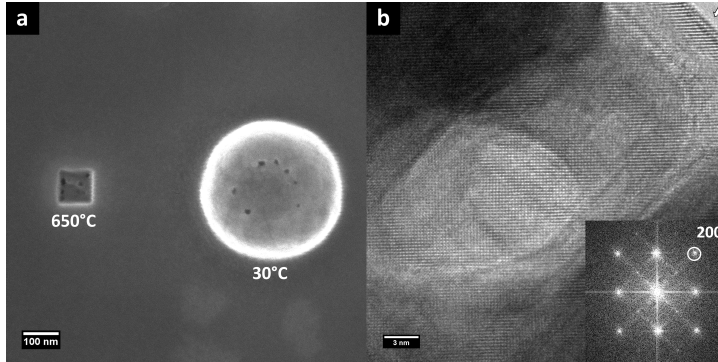


FIGURE 6.9: Result of modifying a  $\text{SrTiO}_3$  lamella at (a) room temperature and  $650^\circ\text{C}$ . At room temperature, numerous bubble-like defects were formed near the modified area. The left square reveals the  $100\times 100\text{ nm}^2$  cut made in the lamella at  $650^\circ\text{C}$ . As can be seen in Figure 6.9(a), no visible defects were created around the cut at these conditions; (b) TEM image of the hole made in a  $\text{SrTiO}_3$  sample. Lattice planes are clearly visible, confirming that the sample remains crystalline.

The experimental results presented in this chapter show that the HIM can be used as an artefact-free cutting tool. Although for some samples like layered  $\text{Cu}_x\text{Bi}_2\text{Se}_3$  or Pt nanowires modification can be done already at room temperature [24], most of the samples require heating to provide fast out diffusion of the implanted helium ions before they form irreversible defects. In addition to the out diffusion of helium, the deposition depth profile also plays an important role, providing that for thin enough samples even room temperature sculpting can be done. Our experiments show that for digging a hole in 100 nm thick Si at room temperature, the damage, created on the remaining area in close proximity to the hole, is so small that no effect of implanted helium is visible in the HIM image or the electron diffraction patterns whereas abundant defects are present in the 300 nm thick sample.

TRIM simulations of the stopping range of helium ions at 25 kV in silicon (Figure 6.10) represent that the distribution of the deposited helium ions has a Gaussian shape with maximum (mean projected range) at  $\sim 250\text{ nm}$ . For a sample thickness of  $\sim 100\text{ nm}$ , only a small fraction of the helium ions is stopped in the sample and furthermore the interaction volume is small due to the high collimation of the beam. Therefore the interaction of helium with silicon samples thinner than about 100 nm should not create serious damage even at room temperature, as indeed observed



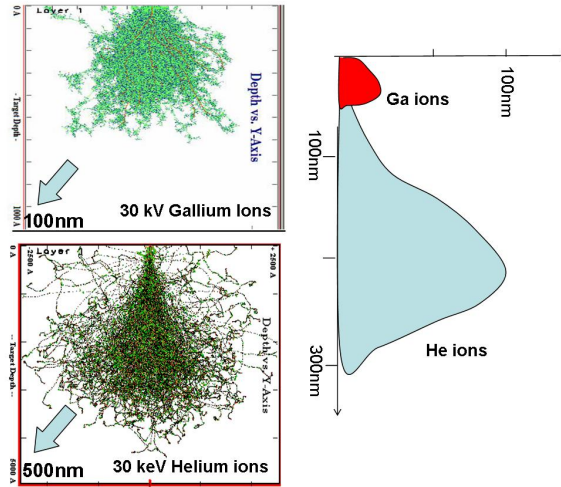


FIGURE 6.10: (a) Stopping range of 30 keV gallium and helium ions in silicon. (b) Comparison of the penetration depth areas for the gallium and helium ions.

experimentally and shown in Figure 6.4(a). However, if one wants to modify thicker silicon samples using a helium beam, significant damage to the sample is expected. In the case of SrTiO<sub>3</sub>, the penetration depth is less (the mean projected range is 130 nm for 25kV helium ions) and sample damage is expected to occur at room temperature even for thin samples.

The TRIM calculations are in good agreement with our experimental data and with previous studies [1, 8] showing that at high enough dose, silicon within ion propagation path becomes amorphous and small nanobubbles are formed in the amorphous region. Further implantation of helium ions leads to a deformation of the amorphous surface layer and the formation of a balloon-like structure [25].

The diffusion of helium in silicon is given by [26]:

$$D[m^2/s] = 7.6 \times 10^{-7} e^{-0.8[eV]/kT} \quad (6.1)$$

for  $300 \leq T[^\circ\text{C}] \leq 900$ . The diffusion is exponentially dependent of temperature (Figure 6.11). Thus once out diffusion is significant, even a minor increase of the temperature will strongly accelerate it. For both Si and SrTiO<sub>3</sub> the out-diffusion at around 650°C is large enough to prevent the formation of defects.

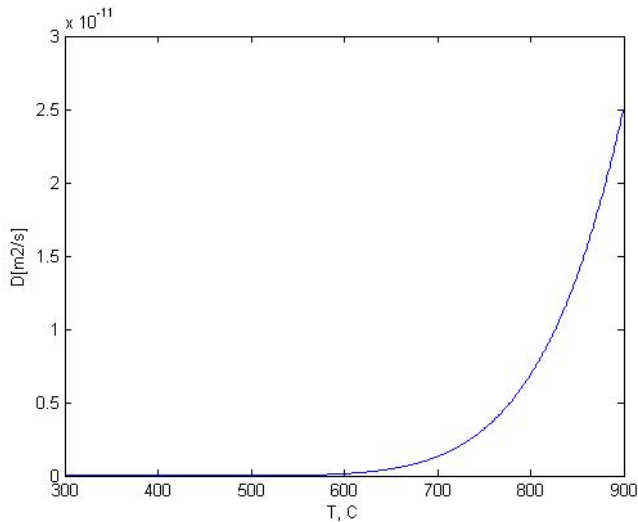


FIGURE 6.11: Diffusion of helium in silicon as a function of temperature.

## 6.4 NANOSCALE MODIFICATION OF PT BRIDGES

To fabricate metallic lines that are used for making contacts amongst nanowires, carbon nanotubes and metallic nanobridges, one commonly uses optical and e-beam lithography. However, this fabrication method is quite time-consuming and costly, and therefore these structures/devices are produced in batches. If one is interested in local modification/changing of batch-produced samples, it is necessary to perform the entire lithography process again. Thus it would be useful to have a tool for making quick local modifications to the sample. The main requirement of such a tool is that it incurs no significant damage to the surrounding areas. On a scale  $>40$  nm, a focused gallium ion beam can be used, but it is known that it leads to a significant modification of the surface layer and introduces gallium contamination to the sample. The helium ion microscope can be considered a better tool because it employs light helium ions instead of heavy gallium ions and because virtually no chemical interaction of the helium ions with atoms of the target will occur.

In order to check the applicability of the HIM for local modification of the TEM samples made by lithography, we selectively cut thin polycrystalline Pt bridges

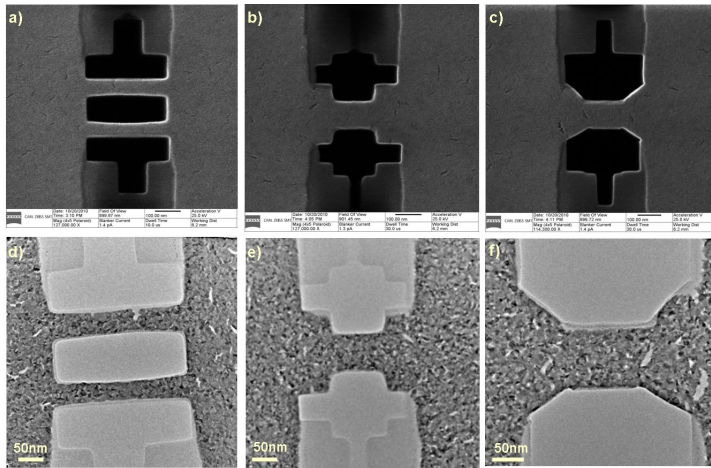


FIGURE 6.12: (a, b, c) HIM and (d, e, f) corresponding TEM images of Pt bridges modified by a helium ion microscope.

deposited onto membrane to create various shapes. Obviously the reason to make these shapes is to correlate changes in geometry for those samples with changes in their properties. For example, electrical measurements can be performed [27].

Polycrystalline platinum bridges and gold electrical contacts were produced on the  $\text{Si}_3\text{N}_4$  membrane in two steps, namely e-beam lithography and subsequent CVD deposition. The bridges have dimensions of  $200 \times 300 \times 15 \text{ nm}^3$  and the thickness of the membrane is 100 nm. Details of the sample fabrication process can be found in Chapter 2 and [28]. These structures have been used as test samples to demonstrate the capability of a helium ion microscope to yield the desired shape.

It is possible to modify the samples to the desired shape by manual control or by use of a special pattern-generating program. Pictures of the modified bridges obtained with an HIM and a TEM are shown in Figure 6.12. From a large variety of HIM-made shapes, we selected the most illustrative ones: (a) two thin, freestanding bridges with a width of  $\sim 50 \text{ nm}$  are separated by a 100-nm pitch; (b) a resized bridge measuring  $W=W_0/2$  and  $L=L_0/2$  compared to the original bridge and with edges perpendicular to the contacts; (c) a resized bridge measuring  $W=W_0/2$  and  $L=L_0/2$  compared to the original bridge and with edges that are at a  $45^\circ$  angle to the contacts. In all cases, the  $\text{Si}_3\text{N}_4$  membrane around the bridges was removed without affecting the bridges.

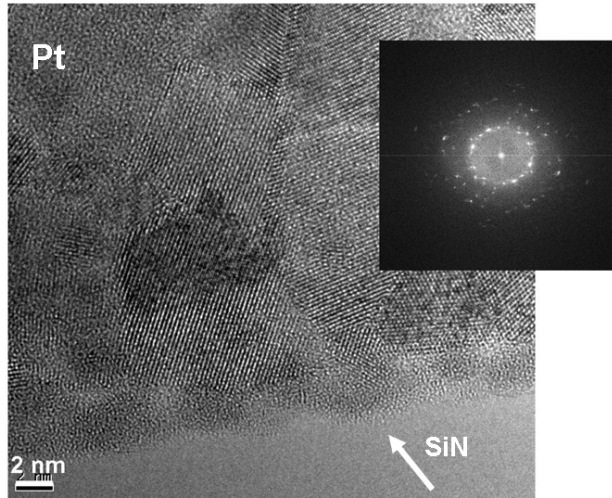


FIGURE 6.13: HREM picture of the edge of Pt bridge showing no effect of He-beam illumination of surrounding area. Rough line marked with white arrow is due to presence of underlying SiN membrane.

A transmission electron microscope FEI Titan was employed to study the samples and to analyse both the purity of the cuts and the damage caused by a helium beam. The high-resolution TEM inspection reveals that the Pt lattice is visible up to the cutting edge and that artefact-free cutting of Pt can be done with the HIM (Figure 6.13). Small polycrystalline grains and underlying SiN membrane are clearly seen at the TEM image.

## 6.5 IN SITU ELECTRICAL MEASUREMENTS ON HIM MODIFIED SAMPLES

Previously (Chapter 3 and 4) we reported *in situ* observation of the grain growth and electromigration processes in thin polycrystalline Pt bridges [28] under passing of electrical current. Here we present results of electrical measurements carried out on samples sculptured using HIM as described above. After reshaping, the samples were glued to an Al<sub>2</sub>O<sub>3</sub> chip carrier and then mounted onto a TEM holder with electrical connections. The electrical measurements were performed with a high-speed AD-DA controller (ADwin-Gold I) and homemade voltage divider/current amplifier. In present experiments we use passive control schema: voltage is gradually

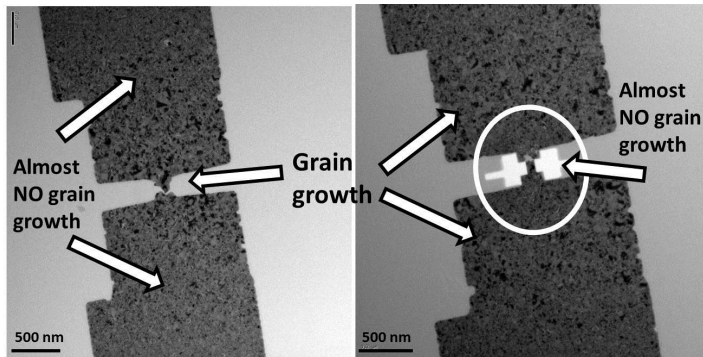


FIGURE 6.14: *In situ* electrical measurements on (a) original and (b) Helium beam modified Pt samples. (a) Grain growth observed in the bridge and surrounding areas. (b) Grain growth inhibited in the areas around helium beam cut, while normal grain growth observed in the outlying region.

increased with constant speed of 8mV/s from 0 to 500-600 mV and then lowered back to 0. Simultaneous observation of changes in the Pt bridges is carried out with FEI Titan TEM. It was shown for non-modified bridge [28] that at voltage values close to 0.2-0.3 V grain growth process starts. Further increase of the voltage leads to subsequent enlargement of the grains and destruction of the bridge due to electromigration, see Figure 6.14(a). Performing the electromigration experiments at the same conditions gives different results for modified bridges. It is expected that by applying current with high enough density through the bridge one simultaneously heat up the sample. For the used sample shapes, the temperature should be maximal close to the narrowest part and gradually decrease toward the gold contacts. In case of initial (non-modified) bridge this temperature distribution results in grain growth in the central area. With further increase of the voltage, the grain growth area expands to the wide platinum leads. That normally results in the grain size distribution as shown in Figure 6.14(a). For the bridge, modified with helium beam, one can notice unusual grain growth. The narrowest area in this case still remains in the center of the bridge but grain growth preferably occurs on periphery, namely in the non-illuminated areas. Figure 6.14(b) shows that in non-illuminated areas grain growth goes much slower compare to the experiments done on initial bridges.

For the sample, shown at Figure 6.15(a) we selectively removed SiN membrane from one side while rest of the bridge remains intact. TEM observations show

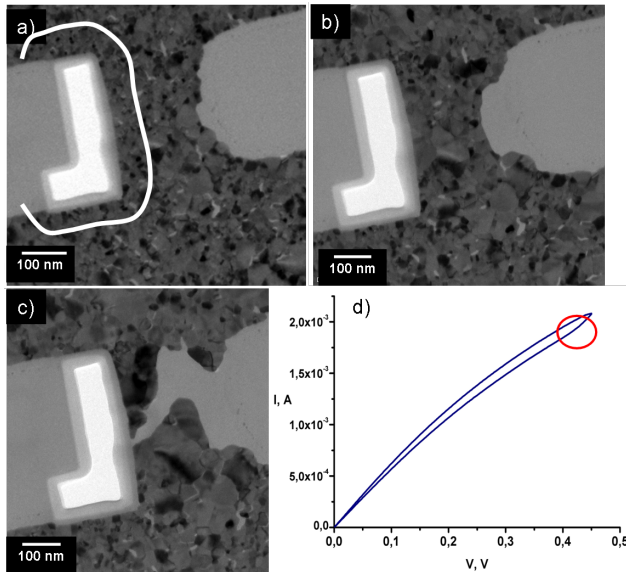


FIGURE 6.15: (a) Pt bridge with partly removed membrane after application of maximum bias of 500 mV. Grain growth is observed in the non-modified part of the bridge; (b) Pt bridge after application of 550 mV. Grain growth is observed on the whole bridge; (c) Bridge broken due to electromigration; (d) Typical I-V curve of the process.

that if we increase voltage through the sample linearly, at values, close to 0.3 V grain growth process starts in unaffected area of the bridge. For the illuminated part no grain growth occurs in areas up to  $\sim 70$  nm from the cutting edge. Further increase of the voltage leads to grains growth in all areas thus also in the ones close to illuminated. In the end stage, the formed big grains are similar in size distribution and orientation to the grains in untreated part of the sample. Figure 6.15(c) represents the bridge broken by electromigration process. Typical I-V curve obtained during the measurements is shown in the Figure 6.15(d). Small kink at 400 mV marked with red is due to the change of the bridge's resistance during grain growth (See Chapter 3).

This effect could be explained by the possible trapping of helium ions at the interface between Pt and SiN as well as at the grain boundaries during the implantation process. Although the thickness of the sample is relatively small (see discussion for silicon) significant amount of helium can be embedded. Thus to initialize the

grain growth in the sample temperature should be increased significantly and this is achieved at higher voltage values. The area of decelerated grain growth is expanded up to 60-70 nm away from the actual cutting point. TRIM calculation of penetration depth for this particular geometry shows that this number correspond to the spread of helium ions in the sample.

Heating of the sample due to applied voltage leads to increasing of out diffusion of the helium from the sample and at some point bigger grains starts to form also in the areas, surrounding the HIM created hole.

## 6.6 CONCLUSIONS

We have investigated the effect of specimen temperature on the damage created by a focused helium beam in Si and SrTiO<sub>3</sub> samples. It is clearly essential to heat the sample to prevent damage due to the embedded helium ions. If the out diffusion of helium is sufficiently large high-quality cuts can be made. We have shown that heating the sample makes HIM an excellent tool for nanoscale modifications. However, the following limitation must be kept in mind: more complex samples (e.g. parts of ICs) may suffer from unwanted diffusion of such things as dopants, barrier layers or Cu metallization, all of which put an upper limit on the allowed temperature. Further studies (scan strategy, beam current variations etc.) are required to determine the processing window for such complex samples.

## 6.7 REFERENCES

1. Livengood, R., et al., *Subsurface damage from helium ions as a function of dose, beam energy, and dose rate*. Journal of Vacuum Science & Technology B, 2009. **27(6)**: p. 3244-3249.
2. Raineri, V. and M. Saggio, *Radiation damage and implanted He atom interaction during void formation in silicon*. Applied Physics Letters, 1997. **71(12)**: p. 1673-1675.
3. Ziegler, J.F., M.D. Ziegler, and J.P. Biersack, *SRIM - The stopping and range of ions in matter (2010)*. Nuclear Instruments & Methods in Physics Research Section B-Beam Interactions with Materials and Atoms, 2010. **268(11-12)**: p. 1818-1823.
4. Maas, D.J., et al. *Nano-engineering with a focused helium ion beam*. in MRS Proceedings. 2011.
5. Alkemade, P.E.A., et al., *Imaging and Nanofabrication With the Helium Ion Microscope of the Van Leeuwenhoek Laboratory in Delft*. Scanning, 2012. **34(2)**: p. 90-100.

6. Ward, B.W., J.A. Notte, and N.P. Economou, *Helium ion microscope: A new tool for nanoscale microscopy and metrology*. Journal of Vacuum Science & Technology B, 2006. **24(6)**: p. 2871-2874.
7. Bell, D.C., *Contrast Mechanisms and Image Formation in Helium Ion Microscopy*. Microscopy and Microanalysis, 2009. **15(2)**: p. 147-153.
8. Postek, M.T., et al., *Review of current progress in nanometrology with the helium ion microscope*. Measurement Science & Technology, 2011. **22(2)**.
9. Sidorkin, V., et al., *Sub-10-nm nanolithography with a scanning helium beam*. Journal of Vacuum Science & Technology B, 2009. **27(4)**: p. L18-L20.
10. Winston, D., et al., *Scanning-helium-ion-beam lithography with hydrogen silsesquioxane resist*. Journal of Vacuum Science & Technology B, 2009. **27(6)**: p. 2702-2706.
11. Maas, D., et al., *Nanofabrication with a Helium Ion Microscope*. Metrology, Inspection, and Process Control for Microlithography Xxiv, 2010. **7638**.
12. Drezner, Y., et al., *Structural characterization of He ion microscope platinum deposition and sub-surface silicon damage*. Journal of Vacuum Science & Technology B, 2012. **30(4)**.
13. Lemme, M.C., et al., *Etching of Graphene Devices with a Helium Ion Beam*. Acs Nano, 2009. **3(9)**: p. 2674-2676.
14. Yang, J.J., et al., *Rapid and precise scanning helium ion microscope milling of solid-state nanopores for biomolecule detection*. Nanotechnology, 2011. **22(28)**.
15. Rue, C., et al., *Low keV FIB Applications for Circuit Edit*. Istfa 2007, 2007: p. 312-318.
16. Yamauchi, Y., et al., *Bubble formation on silicon by helium ion bombardment*. Applied Surface Science, 2001. **169**: p. 626-630.
17. Raineri, V., et al., *Radiation damage He interaction in He implanted Si during bubble formation and their evolution in voids*. Nuclear Instruments & Methods in Physics Research Section B-Beam Interactions with Materials and Atoms, 1999. **147(1-4)**: p. 292-297.
18. Bruno, E., et al., *He induced nanovoids for point-defect engineering in B-implanted crystalline Si*. Journal of Applied Physics, 2007. **101(2)**.
19. da Silva, D.L., et al., *Formation of bubbles and extended defects in He implanted (100) Si at elevated temperatures*. Nuclear Instruments & Methods in Physics Research Section B-Beam Interactions with Materials and Atoms, 2004. **219**: p. 713-717.
20. David, M.L., M.F. Beaufort, and J.F. Barbot, *Effect of implant temperature on*



*defects created using high fluence of helium in silicon.* Journal of Applied Physics, 2003. **93(3)**: p. 1438-1442.

21. Jia, C.L., A. Thust, and K. Urban, *Atomic-scale analysis of the oxygen configuration at a SrTiO<sub>3</sub> dislocation core.* Physical Review Letters, 2005. **95(22)**.

22. Szot, K., et al., *Localized metallic conductivity and self-healing during thermal reduction of SrTiO<sub>3</sub>.* Physical Review Letters, 2002. **88(7)**.

23. Haeni, J.H., et al., *Room-temperature ferroelectricity in strained SrTiO<sub>3</sub>.* Nature, 2004. **430(7001)**: p. 758-761.

24. Rudneva, M., et al. *Preparation of electron transparent samples of pre-selected areas using a Helium Ion Microscope.* in 17th International Microscopy Congress - IMC17. 2010. Rio de Janeiro, Brazil.

25. Reutov, V.F. and A.S. Sokhatskii, *Formation of ordered helium pores in amorphous silicon subjected to low-energy helium ion irradiation.* Technical Physics, 2003. **48(1)**: p. 68-72.

26. Jung, P., *Diffusion of Implanted Helium in Si and SiO<sub>2</sub>.* Nuclear Instruments & Methods in Physics Research Section B-Beam Interactions with Materials and Atoms, 1994. **91(1-4)**: p. 362-365.

27. Rudneva, M., et al., *In situ transmission electron microscopy imaging of electromigration in Pt nanowires.* Microscopy and Microanalysis, 2012. **11**.

28. Gao, B., et al., *In situ transmission electron microscopy imaging of grain growth in a platinum nanobridge induced by electric current annealing.* Nanotechnology, 2011. **22(20)**.



# SUMMARY

## **In situ Electrical Measurements in Transmission Electron Microscope**

**Maria Rudneva**

In the present thesis the combination of real-time electrical measurements on nano-samples with simultaneous examination by transmission electron microscope (TEM) is discussed. Application of an electrical current may lead to changes in the samples thus the possibility to correlate such changes with the corresponding I-V measurements is very important. Using the TEM along with in-house built sample holder and measurement setup, some important results were obtained. Firstly, current induced grain growth in polycrystalline Pt nanobridges (14 nm thick, 200 nm wide and 300 nm long) was investigated. Direct correlation was found between the evolution of the grain size and the change in the resistance. Secondly, the electromigration in Pt and Pd nanobridges was studied by *in situ* TEM technique. The material transfer during direct and reverse EM process in Pd bridges with different geometry was followed in-situ using scanning TEM.

Further, the results of application of the Helium Ion Microscope (HIM) as a sculpting tool for nano-scaled samples are presented. We discuss the possibility to combine modification of the sample by the focused helium ion beam with local heating of the specimens. Heating is facilitated by using MEMS based heaters developed in-house. The detailed analysis of the modified samples was carried out with FEI Titan transmission electron microscope (TEM) operated at 300 kV. With the proposed method it is also possible to carry out the electrical measurements on a wide range of materials such as metallic and semi-conductor nanowires, nanobridges, nanoparticles and novel materials such as graphene.

# SAMENVATTING

## **In situ elektrische metingen in Transmissie Elektronen Microscopie**

**Maria Rudneva**

In dit proefschrift wordt de combinatie van real-time elektrische metingen op nano-structuren met gelijktijdige onderzoek met transmissie-elektronenmicroscop (TEM) besproken. Het toepassen van een elektrische stroom kan leiden tot veranderingen in de structuren, dus de mogelijkheid om dergelijke veranderingen met de overeenkomstige IV metingen te correleren is heel belangrijk. Met behulp van de TEM, samen met zelf gebouwde samplehouder en meetopstelling, werden enkele belangrijke resultaten verkregen. Eerst werd stroom-geïnduceerde korrelgroei in polykristallijne platina nano-bruggen (14 nm × 200 nm × 300 nm) onderzocht. Directe correlatie is gevonden tussen de evolutie van de korrelgrootte en de verandering in de weerstand. Ten tweede werd de elektromigratie in platina en palladium nano-bruggen bestudeerd met behulp van *in situ* TEM techniek. De materiaaloverdracht tijdens de directe en reverse EM processen in palladium bruggen met verschillende geometrie werd gevolgd in-situ met behulp van scanning TEM.

Verder worden de resultaten van het toepassen van de Helium Ionen Microscop (HIM) als beeldhouwinstrument voor structuren op de nanoschaal gepresenteerd. We bespreken de mogelijkheid om het wijzigen van de structuur door de gefocuseerde helium ionenbundel te combineren met de lokale verwarming van de structuren. Verwarming wordt gerealiseerd met gefabriceerde, op MEMS gebaseerde verwarmingselementen. De gedetailleerde analyse van gemodificeerde structuren werd uitgevoerd met een FEI Titan transmissie-elektronenmicroscop (TEM) opererend bij 300 kV. Met de voorgestelde methode is het ook mogelijk om de elektrische metingen op een breed scala aan materialen uit te voeren, zoals metalen en halfgeleider nanodraden, nano-bruggen, nanodeeltjes en nieuwe materialen zoals grafeen.

# CURRICULUM VITAE

## Maria RUDNEVA

09-06-1985      Born in Moscow, USSR.

### EDUCATION

- 2002–2008      **Undergraduate**  
Moscow Engineering Physics Institute (State University)  
The Advanced Physics Faculty of Russian Academy of Sciences,  
department of Superconductivity and Physics of Nanostructures  
Thesis title: *"Investigation of protective and electrical properties  
of thin carbon diamond-like films"*  
*Promotor:* Dr. M. B. Tzetlin
- 2008–2012      **Ph.D in Physics**  
Delft University of Technology  
National Center for High Resolution Electron Microscopy  
Thesis title: *"In-situ electrical measurements in transmission  
electron microscopy"*  
*Promotor:* Prof. H. W. Zandbergen



# LIST OF PUBLICATIONS

1. **M. Rudneva**, T. Kozlova and H. W. Zandbergen, *Reliability of STEM imaging of thin polycrystalline samples*, in preparation
2. T. Kozlova, **M. Rudneva** and H. W. Zandbergen, *In situ TEM and STEM studies of reversed electromigration in thin palladium bridges*, to be submitted
3. **M. Rudneva**, E. van Veldhoven, S. Malladi, D. Maas, H. W. Zandbergen, *Precise cutting of the Si at elevated temperature using Helium ion microscope*, to be submitted
4. **M. Rudneva**, B. Gao, F. Prins, Q. Xu, H. S. J. van der Zant and H. W. Zandbergen, *In situ transmission electron microscopy imaging of electromigration in Pt nanowires* accepted to *Microscopy and Microanalysis*, 2012.
5. **M. Rudneva**, E. van Veldhoven, S. Malladi, D. Maas, H. W. Zandbergen, *Novel Nanosample Preparation with a Helium Ion Microscope*, accepted to *Journal of Material Research*.
6. B. Gao, **M. Rudneva**, K. S. McGarrity, Q. Xu, F. Prins, J. M. Thijssen, H. W. Zandbergen and H. S. J. van der Zant, *In situ transmission electron microscopy imaging of grain growth in a platinum nanobridge induced by electric current annealing*, *Nanotechnology* **22**, 2010.
7. **M. Rudneva**, E. van Veldhoven, S. Malladi, D. Maas, H. W. Zandbergen, *Application of the Helium Ion Microscope as a sculpting tool for nanosamples*, *MRS Proceedings*, **Volume 1455**, 2012.
8. D. J. Maas, E. W. van der Drift, E. van Veldhoven, J. Meessen, **M. Rudneva**, and P. F. A. Alkemade, *Nano-engineering with a focused helium ion beam*, *MRS Proceedings*, **Volume 1354**, 2011.

## Patents(s):

D. J. Maas, **M. Rudneva**, E. van Veldhoven en H. W. Zandbergen, HIM Lamella preparation, patent, aanvraagnummer 61/384035/US, 02-12-2010